MINISTÉRIO DA CIÊNCIA, TECNOLOGIA E INOVAÇÃO
INSTITUTO NACIONAL DE PESQUISAS ESPACIAIS

sid.inpe.br/mtc-m21d/2023/04.28.06.44-TDI

IDENTIFICATION AND OBSERVATIONAL ANALYSIS OF MAGNETIC FLUX ROPES USING PARKER SOLAR PROBE DATA

Dorcas Dupe Oseni

Master's Dissertation of the Graduate Course in Space Geophysics, guided by Drs. Marlos Rockenbach da Silva, and Marcos Willian da Silva Oliveira, approved in April 24, 2023.

URL of the original document:
<http://urlib.net/8JMKD3MGP3W34T/4929CRP>

INPE
São José dos Campos
2023

PUBLISHED BY:

Instituto Nacional de Pesquisas Espaciais - INPE
Coordenação de Ensino, Pesquisa e Extensão (COEPE)
Divisão de Biblioteca (DIBIB)
CEP 12.227-010
São José dos Campos - SP - Brasil
Tel.:(012) 3208-6923/7348
E-mail: pubtc@inpe.br

MINISTÉRIO DA CIÊNCIA, TECNOLOGIA E INOVAÇÃO
INSTITUTO NACIONAL DE PESQUISAS ESPACIAIS

sid.inpe.br/mtc-m21d/2023/04.28.06.44-TDI

IDENTIFICATION AND OBSERVATIONAL ANALYSIS OF MAGNETIC FLUX ROPES USING PARKER SOLAR PROBE DATA

Dorcas Dupe Oseni

Master's Dissertation of the Graduate Course in Space Geophysics, guided by Drs. Marlos Rockenbach da Silva, and Marcos Willian da Silva Oliveira, approved in April 24, 2023.

URL of the original document:
<http://urlib.net/8JMKD3MGP3W34T/4929CRP>

INPE
São José dos Campos
2023

Cataloging in Publication Data

Oseni, Dorcas Dupe.

Os22i Identification and observational analysis of magnetic flux ropes using parker solar probe data / Dorcas Dupe Oseni. – São José dos Campos : INPE, 2023.

xxviii + 152 p. ; (sid.inpe.br/mtc-m21d/2023/04.28.06.44-TDI)

Dissertation (Master in Space Geophysics) – Instituto Nacional de Pesquisas Espaciais, São José dos Campos, 2023.

Guiding : Drs. Marlos Rockenbach da Silva, and Marcos Willian da Silva Oliveira.

1. ICME. 2. Magnetic cloud. 3. Magnetic flux rope. 4. Parker solar probe. 5. Minimum variance analysis. I.Title.

CDU 550.38

MINISTÉRIO DA CIÊNCIA, TECNOLOGIA E INOVAÇÃO

INSTITUTO NACIONAL DE PESQUISAS ESPACIAIS
Serviço de Pós-Graduação - SEPGR

MASTER DISSERTATION FINAL DEFENSE - DORCAS DUPE OSENI
REG. 199823/2021, EVALUATION COMMITTEE Nº 071/2023

On April 24th, 2023, the above-mentioned candidate has defended his/her final Master Dissertation (oral presentation followed by questions) before an Examining Board, whose members are listed below, in a hybrid format, with some of the members participating via video conference.

The candidate has been APPROVED unanimously by the Examining Board, fulfilling the requirements for receiving the Degree of Master in Space Geophysics/Solar-Terrestrial Environment Sciences. The final work is required to be published with the suggestions made by the Examining Board and reviewed by the advisor(s).

Title: "IDENTIFICATION AND OBSERVATIONAL ANALYSIS OF MAGNETIC FLUX ROPES USING PARKER SOLAR PROBE DATA"

Examining Board Members:

Dr. Alisson Dal Lago – President – INPE
Dr. Marlos Rockenbach da Silva – Advisor – INPE
Dr. Marcos Willian da Silva Oliveira – Advisor– IFSP
Dr. Ezequiel Echer –Internal Member – INPE
Dr. Arian Ojeda González – External Member – IP&D/UNIVAP
Dra. Nada Al Haddad – External Member – University of New Hampshire/Space Science Center

Declaration of approval by Nada AlHaddad in a separate attached document.

Documento assinado eletronicamente por **Ezequiel Echer**, **Pesquisador**, em 28/04/2023, às 14:24 (horário oficial de Brasília), com fundamento no § 3º do art. 4º do Decreto nº 10.543, de 13 de novembro de 2020.

Documento assinado eletronicamente por **Alisson Dal Lago**, **Pesquisador**, em 28/04/2023, às 16:58 (horário oficial de Brasília), com fundamento no § 3º do art. 4º do Decreto nº 10.543, de 13 de novembro de 2020.

Documento assinado eletronicamente por **Marlos Rockenbach da Silva**, **Pesquisador**, em 28/04/2023, às 17:32 (horário oficial de Brasília), com fundamento no § 3º do art. 4º do Decreto nº 10.543, de 13 de novembro de 2020.

Documento assinado eletronicamente por **marcos william da silva oliveira (E)**, **Usuário Externo**, em 02/05/2023, às 10:29 (horário oficial de Brasília), com fundamento no § 3º do art. 4º do Decreto nº 10.543, de 13 de novembro de 2020.

Documento assinado eletronicamente por **Arian ojeda gonzalez (E)**, **Usuário Externo**, em 09/05/2023, às 15:01 (horário oficial de Brasília), com fundamento no § 3º do art. 4º do Decreto nº 10.543, de 13 de novembro de 2020.

A autenticidade deste documento pode ser conferida no site https://sei.mcti.gov.br/verifica.html, informando o código verificador **11018459** e o código CRC **1C65CA91**.

Referência: Processo nº 01340.003056/2023-22 SEI nº 11018459

"14. You are the light of the world. A city that is set on a hill cannot be hidden".

"15. Nor do they light a lamp and put it under a basket, but on a lampstand, and it gives light to all who are in the house".

Matthew 5:14,15
from the *"Bible"*

*To **God**, my parents **Dorcas** and **Fatai Oseni**, my brother **Theophilus** that have always supported and prayed for me all along the journey and my wonderful roommate **Taiwo Osanyin** for your support and guidance.*

ACKNOWLEDGEMENTS

To Dr Marlos Rockenbach, for his supervision, guidance, support and encouragement throughout the project, you are most excellent. I also greatly appreciate your timely feedback at every stage of the research.

To Dr Marcos and Dra. Rosemeire Williams Oliveira, my co-supervisors, for always being available and sharing your knowledge and resources.

To Dr Alisson Dal Lago and Dr. Ezequiel Echer, president and member of the board for my proposal, thank you for your cogent suggestions and corrections.

To Professor Nada Al-Haddad from the University of New Hampshire, my research mentor, for your corrections, suggestions and support, I am greatly indebted.

To all my teachers and professors of the National Institute for Space Research (INPE), São José dos Campos, who have instilled in me the knowledge and skills needed to produce this work.

To Professor Vale Asari from UFSC, Brazil, my career mentor, thank you for helping me set my priorities and for all the timely advice.

To my colleagues, friends and "family" here in Brazil, Jose Marchezi, Vinicius Deggeroni, Felipe Oliveira, Karen Ferreira, Graziela, Elienara, Adevilson, Prosper and Vera Nyassor, Micheal and Tunmike Adebayo, Tosin Makinde, Frank Chingarandi, Melina Ceruks, Fred Tavares and Marcus, who have assisted in some ways to get this work done, supported me emotionally and made Brazil a second home for me.

To colleagues, I met at SHINE 2022, Anwesha and Sam Badman, who have contributed to my knowledge and taught me some tools used in this research, I also express my vast appreciation.

And to everyone I could not mention here, I'm grateful for your impact and influence, great or small.

A great appreciation also to the Parker Solar Probe instruments team, for their consistent feedback and answers to questions.

Huge gratitude to CAPES and CNPQ for the financial support.

ABSTRACT

Interplanetary coronal mass ejections (ICMEs) are coronal mass ejections observed in the interplanetary medium characterised by enhanced magnetic field and changes in plasma observations. They sometimes contain magnetic clouds (MCs) that are identified by a coherent change in the direction of their magnetic field direction. The space weather effects of ICMEs on planetary magnetospheres depend on the intensity and orientation of the interplanetary magnetic field, velocity and length of passage time of MCs in the ICMEs. In the case of Earth, the effects are strong especially when there is a persistent southward orientation (i.e., negative B_z) for a long duration. The study of the evolution of these structures is important for predicting their magnetic profile and estimating their space weather impacts. We systematically search for Interplanetary Coronal Mass Ejections (ICMEs) that contain magnetic clouds, using Parker Solar Probe observational data from 2018 – 2022. We also selected ICMEs that are Earth-bound and are observed by WIND spacecraft. We used the minimum variance analysis (MVA) technique to determine the minimum variance direction of the magnetic clouds and used the derived measured components of the magnetic field to determine the chirality of the flux ropes. We also used the force-free cylindrical model to reconstruct the in-situ magnetic field data measurements of all events. A total of 17 well-observed magnetic clouds are studied from Parker Solar Probe and sometimes also from spacecraft located in the interplanetary medium within 1 AU. This work discussed five (5) example events in detail including a controversial event and also presented a summary analysis of the identified structures and their evolution as they travel from about ≈0.3 AU at PSP to ≈1 AU at WIND/ACE.

Keywords: ICME. Magnetic cloud. Magnetic flux rope. Parker solar probe. Minimum variance analysis. Lundquist force free model. Space weather.

IDENTIFICAÇÃO E ANÁLISE OBSERVACIONAL DE TUBOS DE FLUXOS MAGNÉTICOS USANDO DADOS DA PARKER SOLAR PROBE

RESUMO

As ejeções de massa coronais interplanetárias (ICMEs) são ejeções de massa coronais observadas no meio interplanetário caracterizadas por campo magnético com características bem definidas, associadas às variações observadas no plasma do vento solar. Às vezes, eles contêm nuvens magnéticas (MCs) que são identificadas por uma mudança coerente na direção do campo magnético. No caso da Terra, os efeitos no clima espacial das ICMEs nas magnetosferas planetárias dependem da intensidade e orientação do campo magnético interplanetário, velocidade e duração do tempo de passagem das MCs nos ICMEs. Os efeitos são fortes, especialmente quando há uma orientação persistente para o sul (ou seja, B_z negativo) por um longo período. O estudo da evolução dessas estruturas é importante para prever seu perfil magnético e estimar seus impactos no clima espacial. Procuramos sistematicamente Ejeções de Massa Coronais Interplanetária (ICMEs) que contêm nuvens magnéticas, usando dados observacionais da Parker Solar Probe de 2018 a 2022. Também selecionamos ICMEs que estão direcionadas à Terra e são observados pela espaçonave WIND. Usamos a técnica de análise de mínima variância (MVA) para determinar a direção de variância mínima das nuvens magnéticas e usamos as componentes medidas derivadas do campo magnético para determinar a polaridade magnética dos tubos de fluxo. Também usamos o modelo cilíndrico livre de forças para reconstruir as medições de dados do campo magnético in-situ de todos os eventos. Um total de 17 nuvens magnéticas bem observadas são estudadas utilizando dados da Parker Solar Probe e, às vezes, também de espaçonaves localizadas no meio interplanetário dentro de 1 UA. Este trabalho discutiu cinco (5) exemplos de eventos em detalhes, incluindo um evento controverso e também apresentou uma análise resumida das estruturas identificadas e sua evolução à medida que viajam de cerca de ≈0.3 AU em PSP para ≈1 AU em WIND/ACE.

Palavras-chave: ICME. Nuvem magnética. Corda de fluxo magnético. Parker Solar Probe. Análise de variância mínima. Modelo livre de força de Lundquist. Clima Espacial.

LIST OF FIGURES

Page

LIST OF TABLES

Page

LIST OF ABBREVIATIONS

AU	–	Astronomical Unit
CDF	–	Common Data Format
CME	–	Coronal Mass Ejection
Dst	–	Disturbance Storm Time index
FIELDS	–	Electromagnetic Fields Investigation
GSE	–	Geocentric Solar Ecliptic coordinate system
ICME	–	Interplanetary Coronal Mass Ejection
IMF	–	Interplanetary Magnetic Field
IS⊙IS	–	Integrated Science Investigation of the Sun
LASCO	–	Large Angle and Spectrometric Coronagraph
LH	–	Left-Hand helicity
MC	–	Magnetic Cloud
MFI	–	Magnetic Field Investigation
MFR	–	Magnetic Flux Rope
MHD	–	Magnetohydrodynamic
MVA	–	Minimum Variance Analysis
PCA	–	Principal Component Analysis
PSP	–	Parker Solar Probe
RH	–	Right-Hand helicity
RTN	–	Radial, Tangential, Normal coordinate system
SECCHI	–	Sun Earth Connection Coronal and Heliospheric Investigation
SECCHI/COR1	–	Inner Coronagraph
SECCHI/COR2	–	Outer Coronagraph
SECCHI/EUVI	–	Extreme UltraViolet Imager
SECCHI/HI	–	Heliospheric Imager
SOHO	–	Solar and Heliospheric Observatory
SPAN	–	Solar Probe ANalyzers
SPAN-A	–	Solar Probe ANalyzers for electrons and ions
SPAN-B	–	Solar Probe ANalyzers for electrons
SPC	–	Solar Probe Cup
STEREO-A	–	Solar Terrestrial Relations Observatory Ahead
SW	–	Solar Wind
SWE	–	Solar Wind Experiment Ion
SWEAP	–	Solar Wind Electrons Alphas and Protons
UT	–	Universal Time
WIND	–	Comprehensive Solar Wind Laboratory for Long-Term Solar Wind Measurements
WISPR	–	Wide-field Imager for Solar Probe

LIST OF SYMBOLS

R_s	–	Solar radius. $1R_s$ is about 700,000 km/420,000 miles/16 arc minutes.
ρ, N	–	Density
V	–	Volume
α	–	Force-free model constant
$\alpha(r)$	–	Function of position in the force-free magnetic field model
μ_0	–	Magnetic permeability in vacuum
β	–	Plasma beta
θ	–	Latitude of flux rope axis
ϕ	–	Longitude of flux rope axis
x_i	–	Eigen vectors
λ_i	–	Eigen values
χ	–	Magnetic field angle of rotation
v_{exp}	–	MC expansion speed
H	–	Magnetic helicity
R	–	Radial distance
V_A	–	Alfven speed
p	–	Impact parameter
t	–	Time
$\vec{B}$	–	Magnetic field
B_A	–	Axial magnetic field component of the force-free model
B_R	–	Redial magnetic field component of the force-free model
B_T	–	Tangential magnetic field component of the force-free model
$\vec{E}$	–	Electric field
$\vec{J}$	–	Electric current density
σ_0	–	Electric conductivity
v_{sw}	–	Solar wind velocity
g	–	Acceleration due to gravity
J_i	–	Bessel functions
$M^B_{\mu v}$	–	Covariance matrix
B_{lat}	–	Latitudinal variation of the magnetic field
B_{lon}	–	Longitudinal variation of the magnetic field
m	–	metre
h	–	hour
$sec(s)$	–	second(s)
$min(s)$	–	minute(s)
nT	–	nanoTesla
(x, y, z)	–	Cartesian coordinate system
(r, v, z)	–	Cylindrical coordinate system
(J_r, J_v, J_z)	–	Cylindrical coordinate system of electric current density components
(B_r, B_v, B_z)	–	Cylindrical coordinate system of magnetic field components

CONTENTS

Page

1 INTRODUCTION

1.1 Research background

The Sun is the source of light, warmth and energy on Earth but it is neither constant and its influence is not entirely advantageous. The Sun being energetic and very dynamic releases a continuous outward flow of plasma at an average speed of 400 km/s (GOSLING et al., 1971), known as the solar wind. The solar magnetic field embedded in the plasma thus flows with the solar wind. Varying regions of the Sun produce solar wind of varying speeds and densities; coronal holes are known to produce high-speed solar wind ranging from 500 - 1000 km/s, especially at the poles (RICKETT et al., 1976; GOSLING et al., 1976). Space weather impacts highly depend on the solar wind speed, its density and the direction of the magnetic field embedded in it and the Earth's magnetosphere has been a shield to us from the majority of extreme conditions from the Sun.

Coronal mass ejections (CMEs) are one of the most important processes that occur in the solar atmosphere. They are described to be huge plasma particle bubbles filled with magnetic field lines, frequently erupting from the Sun's atmosphere. These structures move outward through the solar corona at speed up to 2000 km/s (LIN, 2000) and move through interplanetary space. They sometimes reach the Earth's magnetosphere with important effects over the current systems, radiation belts and ionosphere, and even on the Earth's surface. CMEs were first observed with a coronagraph on the 7th Orbiting Solar Observatory (OSO 7) from 1971 to 1973 (TOUSEY et al., 1973). A coronagraph is a specialized instrument that uses a disk of the apparent same size as the Sun to block direct light from the Sun's bright surface so that the corona can be observed.

ICMEs are interplanetary CMEs that are observed *in situ* in the interplanetary medium. It is important to study ICMEs because those with strong and sustained southward magnetic field components are known to be the main drivers of strong geomagnetic activity on Earth (GONZALEZ; TSURUTANI, 1987; ECHER; GONZALEZ, 2004; KILPUA et al., 2017a). They impact spacecrafts in the interplanetary medium and in Earth's low orbit and also impact other planets.

1.2 Research motivation

A subset of ICMEs that are distinguishable by an enhanced magnetic field that rotates in direction is described in terms of a magnetic cloud (MC) and its underlying

structure is described as a magnetic flux rope (MFR) (MARUBASHI, 1986). Some of the earliest description of magnetic cloud were given by Burlaga and Klein (1980), Burlaga et al. (1981) and Klein and Burlaga (1982). Magnetic flux ropes are flux tubes with helical winding about their axis, and they will be described further in Chapter 2. Their polarity is the determinant of the occurrence of magnetic reconnection at the Earth's magnetosphere. They have been observed in regions less than and beyond 1 AU. With the advent of the Parker Solar Probe (PSP) travelling so close to the Sun than any other spacecraft, we aim to study these structures at distances that have not been observed before and also make comparisons of their observations at regions closer to Earth. The previous record of the closest approach distance to the Sun was held by Helios 2 on April 17, 1976, at 43.4 million kilometres (0.29 AU)[1]. This was after Helios 1 passed within 47 million kilometres (0.31 AU) from the Sun on March 15, 1975[2]. PSP is set to come within 6.2 million kilometres (0.04 AU) of the Sun in 2025[3].

1.3 Research objectives

The scientific question to be answered: what is the nature of magnetic clouds at distances very close to the Sun and how well do they evolve as they travel outward?

The specific objectives are:

a) Identification of magnetic flux rope structures in ICME events observed by Parker Solar Probe.

b) Determination of the orientation of the flux ropes using the minimum variance analysis (MVA) technique.

c) Application of the Lundquist force-free model.

d) Description of the evolution of magnetic clouds as they propagate from the Sun.

The main contributions of the work are:

a) To have better understanding of the structure of magnetic flux ropes near the Sun, and in the interplanetary medium.

[1] Helios 2 Mission
[2] Helios 1 Mission
[3] Parker Solar Probe Mission

b) To understand and reproduce the evolution of the magnetic topology, configuration and stability of flux ropes as they propagate from the Sun to Earth.

c) Enhanced understanding of these structures will contribute to Space weather forecast.

2 FUNDAMENTAL THEORIES

2.1 Solar eruptions: Coronal Mass Ejections (CMEs)

The Sun is a variable star undergoing several processes, but the most dynamic and striking changes are the short-term eruptions that occur in the Sun's atmosphere and can persist for minutes, hours or even a day. Examples of these are solar flares and prominences which occur in the chromosphere and corona, and coronal mass ejections (CMEs) that expel a large part of the coronal plasma (EDDY, 2009). They are heavily influenced by the 11-year solar cycle and perturb the solar wind as they move away from the Sun.

CMEs are powerful ejections and their interplanetary counterparts are the major drivers of Space Weather disruptions that affect technological and human operations. They involve the eruption of a large amount of plasma and magnetic flux at high speeds from the solar corona into the solar wind and are referred to as interplanetary coronal mass ejections (ICMEs) when observed in the interplanetary medium. When they reach the Earth's magnetosphere, their orientation can cause geomagnetic storms through reconnection processes at the magnetopause (BURLAGA; KLEIN, 1980). These interplanetary disturbances affect technologies in the interplanetary medium, and planets and even impact human activities on Earth.

Most of the eruptions observed in the corona are due to the dominating magnetic forces over other forces such as pressure gradient and gravity (WIEGELMANN; SAKURAI, 2021). The magnetic field originates from the solar dynamo that couples the solar atmosphere to its core. So far, we only have highly accurate measurements at the photosphere with the aid of a vector magnetogram—which gives the magnetic field vector of the photosphere (WIEGELMANN; SAKURAI, 2021).

CMEs can be observed in the outer solar atmosphere by a device called a coronagraph, and in the interplanetary medium by a spacecraft that measures the plasma and magnetic field *in situ*. Figure 2.1 shows a CME that was captured by the STEREO spacecraft. Currently, there is a wide field imager on the Parker Solar Probe (PSP/WISPR (VOURLIDAS et al., 2016)) that will be able to give white-light images of the solar wind, shocks, and solar eruptions.

The velocity of CMEs can be up to ≈ 3500 km/s and the mass can reach 10^{17} grams (GOPALSWAMY et al., 2009). There can be one CME eruption in three days and there can be multiple eruptions in one day. The source of eruption can also range

Figure 2.1 - A CME observed by STEREO in July 2011.

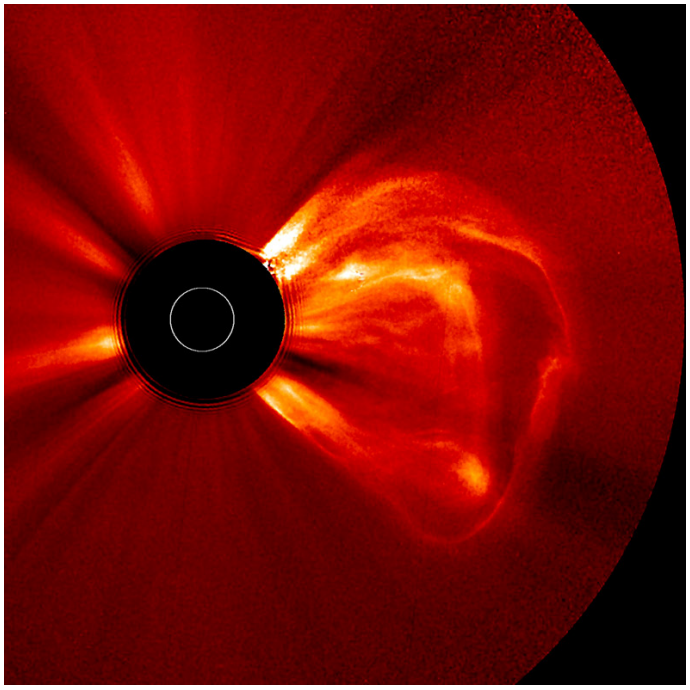

This still image shows the second and larger of the two CMEs that erupted from the Sun from July 24-25, 2011. The white circle represents the Sun, and additional areas were blocked out with an occulting disk so that the fainter structures in the corona can be observed. The image was taken by the STEREO (Ahead) spacecraft.

SOURCE: Solar Terrestrial Relations Observatory (STEREO) (2011).

from active regions ($\approx 10^4$ km) to quiescent filaments ($\approx 10^6$ km). As they erupt and propagate, they expand but eventually, reach a constant angular width. Some of the observed CMEs by coronagraph exhibit signature of flux-rope morphology (VOURLIDAS et al., 2017).

CMEs in the solar corona sometimes exhibit a 3-part structure famously called the "light bulb" structure. A perfect example of this is shown in Figure 2.2, but there are several CMEs in the coronagraph images that do not perfectly fit into this structure too.

2.1.1 Streamer blowout CMEs (SBO CMEs)

Another major class of coronal mass ejections, that were encountered in this research are called streamer-blowout CMEs (SBOs). They are characterised by slow, wide CME, exhibiting the 3-part structure and lasting from hours to days. They do not

Figure 2.2 - A CME observed by SOHO-LASCO C2 on December 2, 2002.

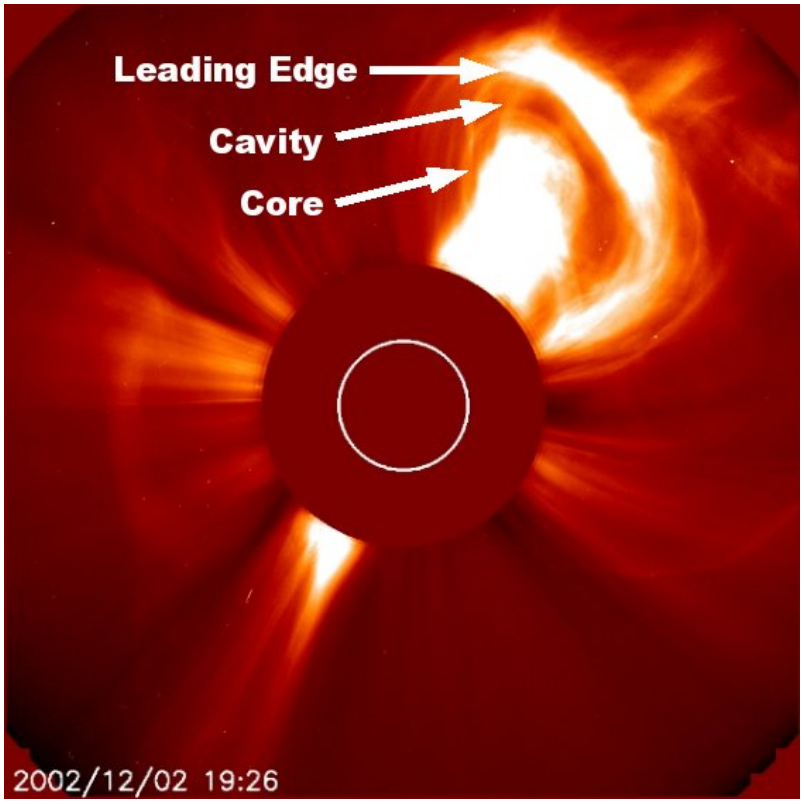

A 3-part CME structure showing a loop-like leading edge, followed by a dark cavity and then a bright core. The image was taken by SOHO/LASCO/C2.

SOURCE: Colaninno (2012).

originate from active regions and are proposed to arise from polarity inversion lines (PILs) outside active regions through magnetic reconnection (VOURLIDAS; WEBB, 2018). They are commonly observed in the quiet Sun and exhibit more flux rope configuration.

2.2 Geomagnetic storms

In the 19th century, it was discovered that the magnetic perturbations observed on the Earth's surface are caused by ring currents flowing in Earth's inner magnetosphere. Geomagnetic storms were defined by 19th-century scientists to be intense, irregular variabilities of the geomagnetic field due to solar disturbances (KAMIDE; CHIAN, 1990). Examples of such disturbances are solar eruptions like CMEs.

The westward flow of ring currents in the magnetosphere is proposed to be the

cause of the geomagnetic disturbances as they cause a decrease in the geomagnetic horizontal intensity of the geomagnetic field on the surface of the Earth. It is important that we are able to predict the interconnected processes within the Sun-Earth system.

2.2.1 Dst index

The depression in the horizontal component H of the Earth's magnetic field for over one to several days is used as a signature for geomagnetic storms. This depression caused by ring currents is measured using Dst index. The Dst is calculated using the equation below:

$$Dst = \frac{1}{N} \sum_{n=1}^{N} \frac{H - H_q}{\cos \phi} \tag{2.1}$$

where H is the horizontal component of the magnetic field disturbance at a particular station, H_q is the horizontal component over the quietest days, N is the total number of stations and ϕ is the station latitude. $\cos \phi$ is used to normalize magnetic disturbances observed at various latitudes to the values at the equator.

Figure 2.3 - Schematic diagram of Dst variation in a typical geomagnetic storm showing the phases of variation.

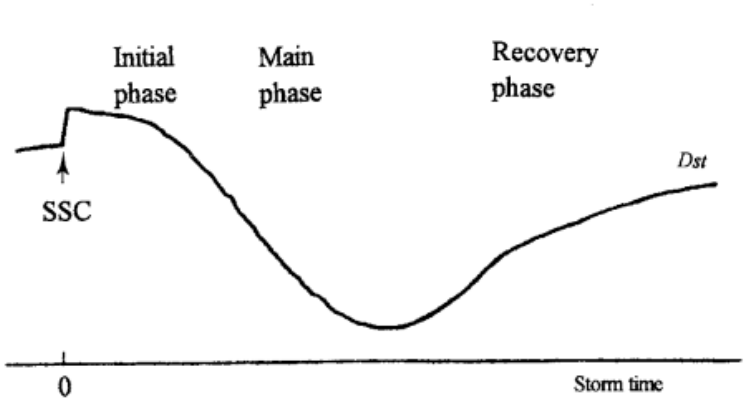

SOURCE: Kamide and Chian (1990).

The general standards for geomagnetic storms are time periods with a minimum of Dst less than -50 nT. Thus, the minimum Dst values are now commonly accepted to deduce the magnitude of magnetic storms (GONZALEZ et al., 1994). The phases of Dst in a typical geomagnetic storm vary from sudden commencement (SSC) to

the initial phase, main phase and recovery phase; this is shown in Figure 2.3. The sudden commencement stage is characterised by a sudden positive increase in the H component followed by a fairly constant phase called the initial phase. Then the main phase is characterised by a depressed H component over one or a few hours. The storm ends with a recovery phase where the H component slowly recovers.

2.3 Interplanetary Coronal Mass Ejections (ICMEs)

Several studies like Tsurutani et al. (1990) and Lindsay et al. (1999) have established a connection between remotely observed CMEs and *in-situ* measured interplanetary CMEs. In the interplanetary medium, ICMEs are often (but not always) characterised by coherent magnetic field structures lasting of the order of a day (sometimes longer than a day) at 1 AU, and a shock wave. There are shocks and sheaths in the interplanetary space that are associated with ICMEs.

Fast forward shock occurs when the propagation speed of the ICME in the solar wind frame exceeds the fast MHD wave, which is the Alfvén speed (v_A, in the direction of the ambient magnetic field) and is the magnetosonic speed (v_{ms}, in the perpendicular direction to the magnetic field). Reverse shocks can also occur and are caused by the overexpansion of ICMEs at speeds that are comparable to the ambient solar wind (GOSLING et al., 1998). Reverse shocks move towards the Sun relative to the solar wind medium (GONZÁLEZ et al., 2014). ICMEs can travel faster than the ambient solar wind but do not drive a shock. Yet, they deflect and compress the plasma flow ahead of them and cause disturbed regions called sheaths, while their leading waves appear like under-developed shocks (KILPUA et al., 2017b).

The sheath is the region found between the shock and the leading edge of the magnetic ejecta. Here, there are sudden changes in the solar wind parameters, and the compressed region is characterised by rapid fluctuations in the magnetic field.

Both structures, ICME shock and sheath are visible in the left-hand side plot in Figure 2.4. The shock is signified by the vertical blue dotted line and the leading edge or front boundary of the ICME is signified by the continuous vertical red line. In between the shock and the leading edge is the sheath. Within the ICME, is another structure enclosed in the red-dotted vertical line that is called a magnetic cloud (MC).

2.4 Magnetic Clouds

Magnetic clouds (MCs) are highly magnetized plasma structures with distinct characteristics observed in interplanetary coronal mass ejections (ICMEs). It has been shown that ≈30% of ICMEs contain magnetic clouds (GOSLING, 1990; RICHARDSON; CANE, 2010), but varies with the solar cycle, with about 60% ICMEs containing MCs in solar minimum and about 15% at solar maximum (CANE; RICHARDSON, 2003). This will also be evaluated in this work.

Magnetic clouds are best observed when the spacecraft is passing close to the axis of the cloud. According to Burlaga et al. (1981), they are characterized when the following are observed simultaneously:

- Enhanced magnetic field (Figure 2.4, panel *a*).
- Large, smooth and coherent change of the direction of the magnetic field vector on time scales of several hours to days. This is identified in the magnetic field components B_R, B_T, B_N, and in the latitudinal and longitudinal variation of the magnetic field vector i.e., variations in the angles θ and ϕ given in solar ecliptic coordinates (e.g., see Figure 2.4, panel *b* and *c*).
- Relatively low proton temperature and plasma beta (Figure 2.4, panels *e* and *f* respectively).

Additional characteristics of magnetic clouds highlighted and deduced from the application of magnetic cloud models:

- They have an approximately symmetric magnetic field with a peak value near the centre of the observed interval.
- They pass Earth's orbit in about one day as observed by a spacecraft at 1 AU (BURLAGA et al., 1981).
- Some of them (about half) are drivers of interplanetary shock waves.
- They affect the propagation of cosmic rays (SAVIAN et al., 2007; ROCKENBACH et al., 2014). Cosmic rays are charged atomic particles from the Sun or violent events—such as the eruption of a supernova—and they are accelerated in the shock waves that usually follow the cosmic explosion. For example, Forbush decrease (decrease in the intensity of cosmic rays) was

Figure 2.4 - ICME with (left) or without (right) MC signatures as observed by ACE spacecraft.

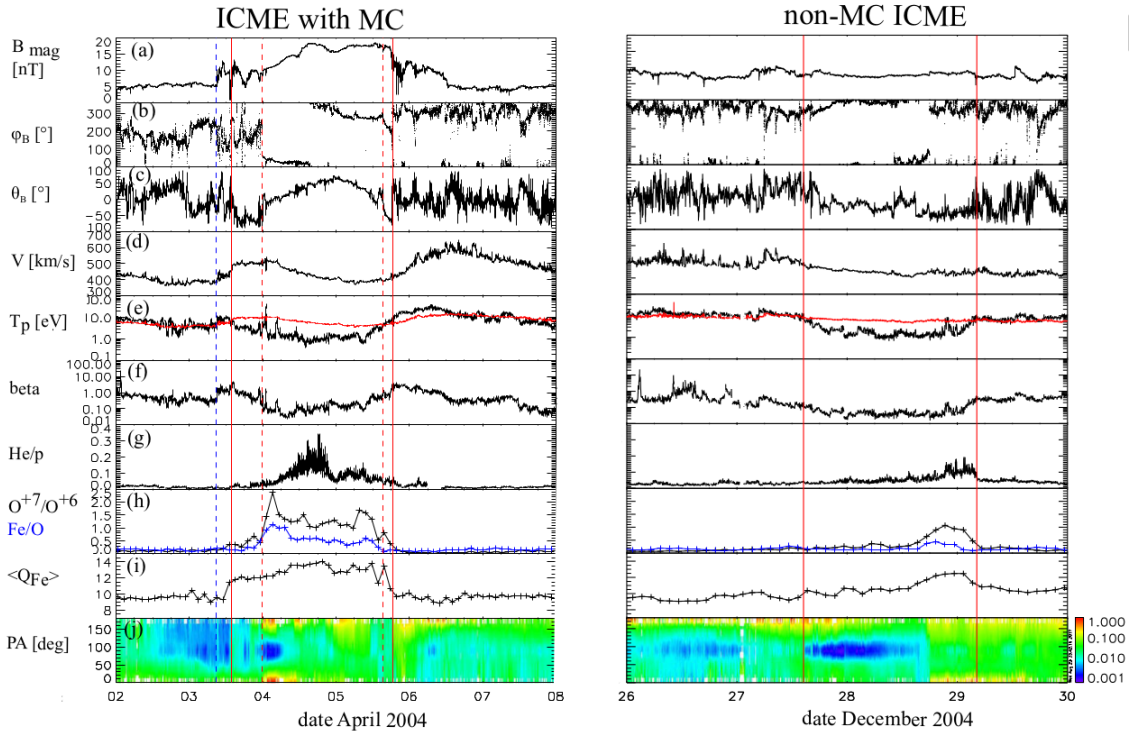

Left: ICME chock preceded the MC and there is a reverse shock after the MC (between the MC end and ICME end). The panel represents: *a)* magnetic field magnitude, *b)* azimuth/latitude and *c)* polar/longitude angles of the magnetic field, *d)* solar wind speed, *e)* temperature, *f)* plasma beta, *g)* helium to proton ratio, *h)* O^{+7}/O^{+6} ratio (black) and Fe/O ratio (red), *i)* iron average charge state, and *j)* pitch angle spectogram of 272-eV electrons. Pitch angle 0° (180°) refers to the particles that stream parallel (anti-parallel) to the magnetic field. The magnetic field angles in solar ecliptic coordinates, θ_B and ϕ_B are defined as $\theta_B = 90° \equiv$ N, $\theta_B = -90° \equiv$ S and $\phi_B = 0° \equiv$ sunward direction, $\phi_B = 90° \equiv$ E, $\phi_B = 270° \equiv$ W.

SOURCE: Kilpua et al. (2017b).

correlated with some of the magnetic cloud parameters such as: magnetic field strength, the helical field structure, velocity and the velocity gradient, geometric dimensions (PETUKHOVA et al., 2019) and shock parameters (VIEIRA et al., 2009).

Cosmic rays are blocked and scattered by inhomogeneities such as magnetic clouds in Space (KAMIDE; CHIAN, 1990).

In addition to these, Burlaga and Klein (1980), Farrugia et al. (1993), Davies et al. (2020) and several other authors also outlined other characteristics such as

- Declining radial speed (can be observed in Figure 2.4, panel *d*), and
- Decreased proton density with the ambient solar wind.

Another characteristic of ICMEs shown in Figure 2.4 is in panel *g*—helium to proton ratio. The enhanced abundance of helium to proton was one of the earliest identified ICME signatures (GOSLING et al., 1973), but other studies have shown that this characteristic is also found in slow solar wind (RODRIGUEZ et al., 2016). Panel *h* gives the O^{+7}/O^{+6} and Fe/O ratios and panel *i* shows the iron average charge state. ICMEs show enhanced high charge states and average iron charge states which are good signatures of the ICME plasma.

The **plasma beta**, β, is a dimensionless number derived from the ratio of plasma pressure to magnetic pressure. This is expressed as

$$\beta = \frac{8\pi NkT}{B^2} = \frac{P_{th}}{P_B} \tag{2.2}$$

where N is the proton density, k is Boltzmann's constant, T is the temperature (it can be the sum of electron and proton temperature $T_e + T_p$, or just T_p), B is the magnetic field, P_{th} is proton thermal pressure and P_B is magnetic pressure. The total pressure is given as $P_{total} = P_{th} + P_B$. Plasma beta is low in magnetic clouds because the magnetic field pressure dominates over thermal pressure within the cloud. β is often very low i.e., averagely $\approx$0.12 and closer to $\approx$0.08 at the center of the MC interval at 1 AU (LEPPING; BERDICHEVSKY, 2000).

Figure 2.4 shows two ICMEs and their signatures as observed by the ACE spacecraft. The vertical red lines represent the start and end times as defined by Richardson and Cane in their ICME list[1]. The red dashed line at the left-hand side of Figure 2.4 bounds the region of the magnetic cloud. The blue dashed line represents the shock wave preceding the ICME, which is defined by the sudden increase in magnetic field magnitude, proton speed and temperature. The ICME on the left hand contains significant changes in the magnetic field and plasma characteristics while the ICME on the right-hand side lacks major changes except for a slightly depressed temperature.

Detailed features of the plasma parameters especially proton temperature, plasma beta and even bulk speed (though not included in the key MC definitions) are useful

[1] http://www.srl.caltech.edu/ACE/ASC/DATA/level3/icmetable2.htm

for defining the clouds' proper boundaries as observed in Figure 2.4 (LEPPING et al., 2006).

Figure 2.5 shows the momentum flux, total pressure, and plasma beta observed in a magnetic cloud. The total pressure (P_{total}) in the cloud is higher than the ambient solar wind thus causing the cloud to expand outwardly even at a distance of 2 AU (BURLAGA et al., 1981). The expansion is principally driven by the dominant magnetic pressure; it reduces the density and thus the momentum flux (Figure 2.5). The momentum flux is an additional cloud parameter given in Burlaga and Behannon (1982).

Figure 2.5 - Additional parameters related to the dynamics of magnetic cloud measured by Voyager 2 at 2 AU.

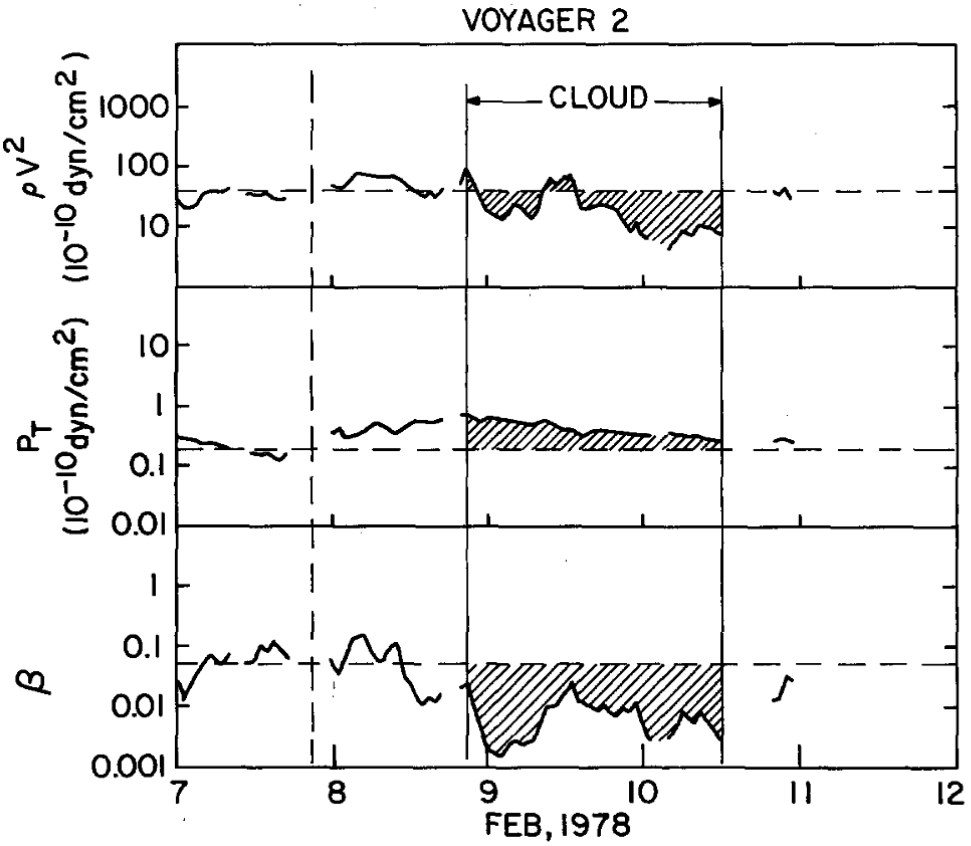

Momentum flux (top), total pressure (middle), and plasma beta (lower panel). There is increased total pressure and cloud expansion which caused reduced momentum flux, and plasma beta is low due to dominating magnetic pressure.

SOURCE: Burlaga and Behannon (1982).

According to Burlaga and Klein (1980), magnetic clouds are extended regions of approximately 0.25 AU at 1 AU. Burlaga and Behannon (1982) noted that they

are stable enough to persist with minor changes up to distances in 2 - 4 AU as observed in the solar wind by Voyager 1 and 2. At this distance, the average radial size of the cloud is increased to approximately 0.47 AU. Using these values, the expansion speed of magnetic clouds in the radial direction is estimated to be about 45 km/s. This is consistent with the expansion speed of ≈33 km/s, derived from the difference between the speed of the clouds' front and rear boundaries. Also, these expansion speeds estimated by the authors are about half of the average Alfvén speed which agrees with Klein and Burlaga (1982) estimations. The latter stated that the expansion speed from the Sun to 1 AU is of the order $v_A/2$.

According to Nieves-Chinchilla et al. (2005), magnetic clouds can be studied using several approaches.

- **Theoretical**: we use idealised structures such as spheroidal, toroidal, elliptical or cylindrical to understand the behaviour of clouds with different magnitudes (BURLAGA et al., 1981; VANDAS et al., 1993; ROMASHETS; VANDAS, 2003; HIDALGO et al., 2002; NIEVES-CHINCHILLA et al., 2016).
- **Numerical simulations**: these are more practical approaches such as using numerical 3 or $2\frac{1}{2}$-dimensional magnetohydrodynamic method (VANDAS et al., 2002; ODSTRCIL et al., 2003), and 2-dimensional magnetohydrostatic approach (HU; SONNERUP, 2002).
- **Analytical models**: they are based on assumed magnetic topologies of MCs that are used to fit the observed data. Examples of such model approaches are linear force-free models (BURLAGA et al., 1981; LEPPING et al., 1990), uniform-twist flux rope model (FARRUGIA et al., 1999), and non-force free models (HU; SONNERUP, 2001; HIDALGO et al., 2002).

These approaches are based on the Lundquist model. Another common approach for studying MCs is the Gradshafranov reconstruction technique (HU; SONNERUP, 2001; AL-HADDAD et al., 2011; AL-HADDAD et al., 2013).

The famous Lundquist model was proposed by Goldstein (1983) as a linear force-free field with a cylindrical magnetic configuration, and it was considered by several authors as a relatively good approximation of MCs field distribution (LEPPING et al., 1990; DASSO et al., 2005).

However, observational data of ICMEs have shown that the plasma pressure gradient is far from constant, thus causing the development and application of other analytical

models based on non-force-free conditions. This change now makes it possible to study the magnetic field and plasma data of magnetic clouds simultaneously (CID et al., 2002).

Most analytical models propose a circular cross-section for the MCs. In a study by Nieves-Chinchilla et al. (2005), the author used a more practical model—an elliptical cross-section model which includes the distortion and expansion of the cross-section of the magnetic clouds from the first principles.

The distortion was included due to previous work, such as Riley et al. (2003) that showed how much ICMEs undergo significant distortion as they travel through the solar wind. Hidalgo et al. (2002) was one of the first to adapt this knowledge by assuming an elliptical cross-section model.

The expansion of the cross-section of MCs is also important because it is the cause of the decrease in the solar wind velocity in MCs.

When Nieves-Chinchilla et al. (2005) compared the elliptical cross-section model with previous works such as Lepping et al. (1990), it was deduced that the orientation angles of the clouds were the only common parameter they shared. However, Al-Haddad et al. (2013) compared the application of force-free constant α technique, self-similarly expanding fitting technique and the Grad-Shafranov reconstruction technique on MCs and deduced that their chirality, orientation and magnetic field strength were closely correlated.

Models that assume a local cylindrical geometry for the MCs also have this parameter in common: the orientation of the cloud axis, which includes:

- the latitudinal variation θ of the magnetic field,
- the longitudinal variation ϕ of the magnetic field, and
- the maximum approach distance to the cloud axis.

We can estimate some global magnetohydrodynamic quantities such as magnetic flux and helicity using *in situ* measurement and assumptions (expressed above) on the magnetic distribution inside the MC (DASSO et al., 2003). To make these estimations, it is important to get the

- orientation of the MC based on fittingtechniques,

- estimation of the cloud size and
- the magnetic components within the cloud (GULISANO et al., 2007).

2.4.1 Magnetic clouds as magnetic flux ropes

Magnetic flux tube (Figure 2.6) is a volume enclosed by magnetic field lines which intersect a closed curve. Flux tubes store magnetic energy ($\int B^2/(2\mu_0)d\vec{V}$), and can work as a channel for the flowing of fast particles, heat and plasma and can also interact with their surroundings transferring mass, momentum and a topological quantity known as *magnetic helicity*. This exchange can be caused by surface pressure forces and magnetic reconnections. When this magnetic flux tube gets twisted, it is called a *magnetic flux rope* (PRIEST, 1990).

Figure 2.6 - A curved flux tube.

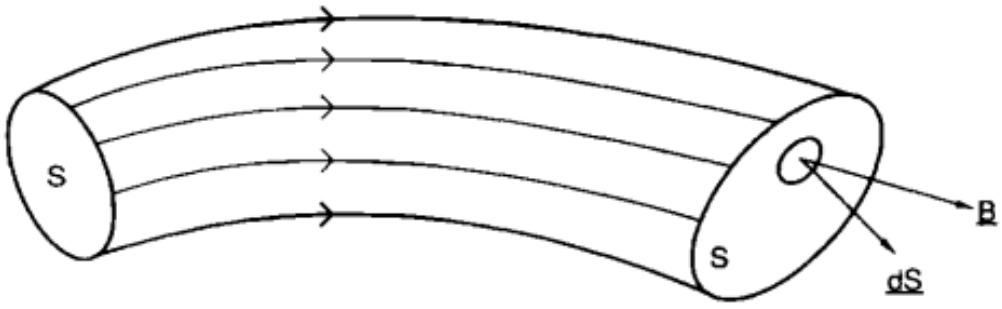

S is the cross-section of the flux tube and B represents the magnetic field.
SOURCE: Priest (1990).

In an attempt to visualize the global magnetic topology of the internal field rotations observed in magnetic clouds (MCs), Goldstein (1983) suggested that MCs can be interpreted as cylindrical magnetic flux ropes, with axial fields near their centre and increasingly poloidal fields towards the outer edges.

Magnetic flux rope is used to describe the helical structure of magnetic field lines found in magnetic clouds. They are thought to give rise to the observed properties of plasma and magnetic properties of these structures. They have approximately three-dimensional (3-D) configurations of twisted magnetic field lines around an axis.

2.5 Magnetic Clouds modelling

There are several MC modelling approaches and none have been found to apply to all kinds of MCs. There are several important things to be considered and parameters that might be prioritised while modelling.

Some of the key questions to be answered are given by Kilpua et al. (2017b):

- Is the magnetic cloud static or expanding?
- Is the cross-section elliptical or more circular?
- Should the plasma effects be prioritised? i.e., whether a force-free or non-force-free model is more appropriate.

Goldstein (1983) gave an early description of magnetic clouds when it was first discovered in the solar wind. The author described them locally as cylindrical magnetic configurations with symmetric force-free magnetic flux ropes ($\boldsymbol{\nabla} \times \vec{B} = \alpha(r)\vec{B}$). Later on, Burlaga (1988) showed that a constant α can satisfactorily describe the magnetic field changes that occur when a spacecraft travels through a magnetic cloud. The concept of the force-free field model is used in this work and will be further reviewed in Section 2.5.2.

Some magnetic clouds have been observed to have asymmetric magnetic field signatures along the observing spacecraft trajectories. This makes it impossible to apply cylindrical configurations. Farrugia et al. (1995) in his work used a force-free Spheromak geometry to account for the asymmetries. Farrugia et al. (1999) also considered a cylindrically shaped cloud but with a non-linear force-free field.

Magnetic clouds have been well-modelled as static plasma columns using magnetohydrodynamic equations, yet they have been observed by several researchers to be dynamic and expanding structures (BOTHMER; SCHWENN, 1998; VANDAS et al., 2009). The expression for MC expansion speed is given as

$$v_{exp} = \frac{1}{2}(v_s - v_e) \tag{2.3}$$

where v_s and v_e are the speeds at the start and end of the MC boundary respectively, obtained from a linear fit of the solar wind profile.

In what sense can magnetic cloud cross-sections be considered static? Bhattacharjee et al. (2022) sought to answer this question by calculating the ratio of expansion speed $|v_{exp}|$ to Alfven speed V_A using *Wind* and Helio ICME events.

$$R_A = \frac{|v_{exp}|}{\langle V_A \rangle} \tag{2.4}$$

The authors state that the expansion speed does not need to be strictly zero, but if $|v_{exp}|$ is small in comparison to characteristic speeds such as the Alfvén speed, the static approximation can be considered valid. To investigate this, the calculated mean, median and most probable values for R_A from the *Wind* events are 0.29, 0.24 and 0.06 respectively. The mean, median and most probable values of R_A for the Helios events are 0.28, 0.25 and 0.03 respectively.

This showed that MC expansion speeds are typically far smaller than Alfvén speeds thus validating the static plasma modellings. Thus MC boundaries can be considered static, to a good extent, over an Alfvén crossing timescale. Although the measurement of the MC expansion speeds is along the line in which the spacecraft intercept the cloud, the rate at which signals propagate from one MC cross-section to another is much less than the rate of the cross-sectional expansion. This further supports the idea of static column modelling.

2.5.1 Principles of magnetohydrodynamics

This principle is needed to explore the force-free model condition. The principles of magnetohydrodynamics (MHD) can be used to model the interaction of plasma and magnetic field, where the plasma is treated as a single continuous medium. It unifies the equations of slow electromagnetism and fluid mechanics.

Magnetohydrodynamic equations are a combination of macroscopic equations for a conducting fluid-like plasma. They represent the set of equations for each species, except for information lost (e.g., through Bremsstrahlung radiation) concerning the variability of each species. Interplanetary magnetic clouds have been represented by cylindrically symmetric equilibrium configurations which are force-free solutions of the MHD equations (GOLDSTEIN, 1983).

Maxwell equations consist of Poisson's equation, vanishing of the divergence of the magnetic field, Faraday's law (2.5d) and Ampere's law (2.5e). Other equations are Ohm's law in the simplified form (2.5f), continuity equation (2.5a), momentum equa-

tion (2.5b), and the adiabatic equation of conservation of energy (2.5c). The displacement current $\partial\vec{D}/\partial t$ is neglected, which is valid when plasma speed $\vec{v} \ll c$ and $v_A \ll c$ (OJEDA-GONZÁLEZ et al., 2021) the speed of light.

Here is the set of simplified magnetohydrodynamic equations:

$$\frac{\partial \rho_m}{\partial t} + \boldsymbol{\nabla} \cdot (\rho_m \vec{u}) = 0 \tag{2.5a}$$

$$\rho_m \frac{D\vec{u}}{Dt} = \vec{J} \times \vec{B} - \nabla p \tag{2.5b}$$

$$\nabla p = V_s^2 \nabla p_m \tag{2.5c}$$

$$\boldsymbol{\nabla} \times \vec{E} = -\frac{\partial \vec{B}}{\partial t} \tag{2.5d}$$

$$\boldsymbol{\nabla} \times \vec{B} = \mu_0 \vec{J} \tag{2.5e}$$

$$\vec{J} = \sigma_0 (\vec{E} + \vec{u} \times \vec{B}) \tag{2.5f}$$

where ρ_m denotes the total mass density, p is total scalar pressure, $\vec{B}$ is magnetic flux density, V_s is adiabatic sound speed, $\vec{u}$ is average fluid velocity, $\vec{J}$ is the electric current density σ_0 is the electric conductivity of the fluid and $\vec{E}$ is the electric field.

To arrive at this set of simplified MHD equations, the following assumption has been made. There is macroscopic electrical neutrality such that electric charge density ρ vanishes. $\partial\vec{E}/\partial t$ is neglected (2.5e) for very low frequency and highly conducting fluids. For Equation (2.5f), time derivatives and pressure gradients are negligible. Viscosity and thermal conductivity are also neglected and the pressure dyad reduces to scalar pressure (BITTENCOURT, 2004).

This set of approximate equations greatly reduced the mathematical complexity of the general equations and helps to understand the physical processes of highly conducting fluids at very low frequencies.

To understand the behaviour of the magnetic field of magnetic structures such as in

MCs, we start by taking the curl of Ohm's law 2.5f,

$$\boldsymbol{\nabla} \times \vec{J} = \sigma_0[\boldsymbol{\nabla} \times \vec{E} + \boldsymbol{\nabla} \times \left(\vec{v} \times \vec{B}\right)]$$

Replacing $\vec{E}$ and $\vec{J}$ with Equations (2.5d) and (2.5e),

$$\boldsymbol{\nabla} \times \left(\boldsymbol{\nabla} \times \vec{B}\right) = \mu_0\sigma_0 \left[-\frac{\partial \vec{B}}{\partial t} + \boldsymbol{\nabla} \times \left(\vec{v} \times \vec{B}\right)\right] \tag{2.6}$$

Using identity $\boldsymbol{\nabla} \times \left(\boldsymbol{\nabla} \times \vec{B}\right) = \boldsymbol{\nabla}^2\vec{B}$ and $\boldsymbol{\nabla} \cdot \vec{B} = 0$, Equation (2.6) becomes

$$\frac{\partial \vec{B}}{\partial t} = \boldsymbol{\nabla} \times \left(\vec{v} \times \vec{B}\right) + \eta_m \boldsymbol{\nabla}^2\vec{B} \tag{2.7}$$

where η_m is magnetic viscosity, $\eta_m = \frac{1}{\mu_0\sigma_0}$.

The first term on the right-hand side of 2.7 is called the *flow term* and the second term is called the *diffusion term*. The ratio of the flow term to the diffusion term is called *magnetic Reynolds number*. Using dimensional analysis, it is given by

$$R_m = \frac{vL}{\eta_m}$$

When $R_m \gg 1$, it means the flow term dominates over the diffusion term and Equation (2.7) reduces to

$$\frac{\partial \vec{B}}{\partial t} = \boldsymbol{\nabla} \times \left(\vec{v} \times \vec{B}\right) \qquad (R_m \gg 1) \tag{2.8}$$

This means that in a highly conducting fluid, the magnetic field lines are *frozen* in the fluid, i.e. they strictly move along with fluid and do not diffuse out (BITTENCOURT, 2004). This is an approximation that is used to describe magnetic clouds (MCs). Equation (2.7) means that in a highly conducting fluid such as a magnetic cloud, its fluid move along the magnetic field lens any motion perpendicular to the field lines will carry them with the fluid.

2.5.2 Linear force-free model

Here, we review the concept of the force-free condition (LUNDQUIST, 1950; GOLDSTEIN, 1983; BURLAGA, 1988) because it is the most typical and simple model for studying magnetic clouds, and it is used to describe the geometry of magnetic clouds in this work. Thus, we describe this method below.

Figure 2.7 - A sample of an electrically conducting fluid at equilibrium in an MHD flow experiencing gravitational force, magnetic force and pressure gradient.

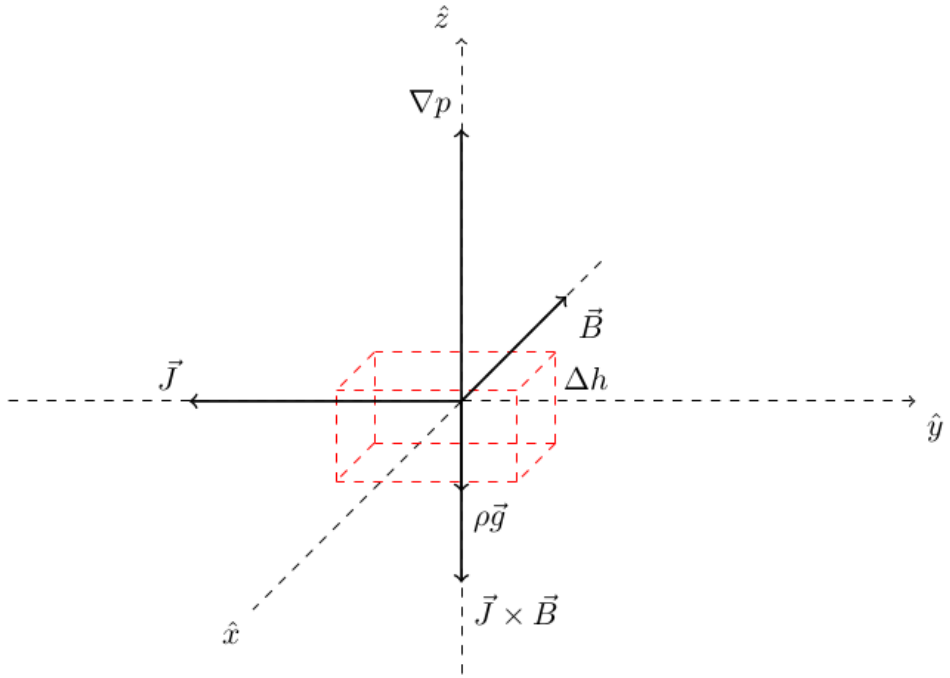

SOURCE: González (2013).

Consider a region in space, where the external magnetic field $\vec{B}$ has a fixed direction perpendicular to the ecliptic plane. There is a volume of plasma in this region experiencing hydrostatic pressure gradient and gravity force as shown in Figure 2.7. The movement of particles in this plasma forms an electric current $\vec{J}$ which is perpendicular to the magnetic field. This is described by the MHD equation for the motion of plasma under the action of a plasma pressure gradient, a magnetic force ($\vec{J} \times \vec{B}$) and gravity expressed as:

$$\rho\left(\frac{d\vec{v}}{dt}\right) = -\boldsymbol{\nabla} p + \vec{J} \times \vec{B} + \rho\vec{g} \tag{2.9}$$

where p is the thermal pressure (nKT), $\vec{B}$ is the magnetic field, $\vec{v}$ is the plasma velocity and $\vec{J}$ is the electric current density.

In regions with $\beta \ll 1$ (as observed in magnetic clouds), the magnetic pressure ($B^2/2\mu$) dominates over the plasma pressure (p) and as well as over other non-magnetic forces like gravity (g) and the kinematic plasma flow pressure ($\rho d\vec{v}$).

From Equation (2.9), we can neglect, in the lowest order, all non-magnetic forces and assume that the Lorentz force ($\vec{J} \times \vec{B}$) vanishes, i.e.

$$\frac{B^2}{2\mu} \gg p$$

$$\frac{B^2}{2\mu} \gg g$$

$$\frac{B^2}{2\mu} \gg \rho \frac{d\vec{v}}{dt}$$

This approach is called the *force-free approximation* and for static configurations, it is defined as:

$$\vec{J} \times \vec{B} = 0 \tag{2.10}$$

Also, the term force-free is used when one refers to the magnetohydrostatic equilibrium when external forces are neglected in the cloud (IVANOV; HARSHILADZE, 1984). From Equation (2.5e):

$$\vec{J} = \frac{1}{\mu_0} \boldsymbol{\nabla} \times \vec{B} \tag{2.11}$$

which is the electric current density. By inserting Equation (2.11) into (2.10), we have:

$$\left(\frac{1}{\mu_0} \boldsymbol{\nabla} \times \vec{B} \right) \times \vec{B} = 0$$

$$(\boldsymbol{\nabla} \times \vec{B}) \times \vec{B} = 0 \tag{2.12}$$

$$\boldsymbol{\nabla} \cdot \vec{B} = 0 \tag{2.13}$$

Equation (2.12) can be fulfilled either by *current-free (potential) magnetic fields* or by *force-free fields*.

I. Current-free or potential magnetic fields:

$$\boldsymbol{\nabla} \times \vec{B} = 0 \tag{2.14}$$

It assumes that the current density $\vec{J}$ is identically zero ($\vec{J} = 0$) so that $\vec{B}$ can be written as the gradient of a scalar magnetic potential. Current free (potential) fields are the simplest assumption for the solar coronal magnetic field.

The most general solution to Equation (2.14) is

$$\vec{B} = \boldsymbol{\nabla}\phi \tag{2.15}$$

Substituting Equation (2.15) into 2.13 gives

$$\boldsymbol{\nabla}^2\phi = \frac{\partial^2\phi}{\partial x^2} + \frac{\partial^2\phi}{\partial y^2} + \frac{\partial^2\phi}{\partial z^2} = 0 \tag{2.16}$$

This is commonly used for the determination of the basic geometry of the magnetic field e.g., in the corona. However, potential fields do not have electric currents (J) that are necessary for plasma heating and impulsive energy e.g., flares and coronal mass ejections (CMEs). Hence, the reason we are considering the second application.

II. Force-free fields:

Equation (2.12) implies that:

$$\vec{B} \parallel \boldsymbol{\nabla} \times \vec{B}$$

$$\vec{B} \parallel \vec{J}$$

It assumes that the magnetic field is not potential ($|\vec{J}| \neq 0$) then the general solution is that the current is parallel to the magnetic field.

We have $\boldsymbol{\nabla} \times \vec{B} = \mu_0\vec{J}$, thus we cannot define a scalar magnetic potential ϕ as indicated in Equation (2.16). The $\vec{B} \parallel \boldsymbol{\nabla} \times \vec{B}$ condition can be rewritten as:

$$\mu_0\vec{J} = \alpha\vec{B}$$

Since $\boldsymbol{\nabla} \cdot \vec{J} = 0$, (the equation of conservation of electric charge in the absence of changes in the total macroscopic charge density ρ) then

$$\boldsymbol{\nabla} \times \vec{B} = \alpha \vec{B} \tag{2.17}$$

for some scalar function α, which may be a function of position and time.

Property of α: The scalar function $\alpha(r)$ is not completely arbitrary since $\vec{B}$ must satisfy the conditions:

- $\boldsymbol{\nabla} \cdot \vec{B} = 0$
- the vector identity $\boldsymbol{\nabla} \cdot (\boldsymbol{\nabla} \times \vec{B}) = 0$

So using Equation (2.17), we obtain

$$\boldsymbol{\nabla} \cdot (\boldsymbol{\nabla} \times \vec{B}) = \boldsymbol{\nabla} \cdot (\alpha \vec{B}) = \alpha \boldsymbol{\nabla} \cdot \vec{B} + \vec{B} \cdot \boldsymbol{\nabla} \alpha$$

Hence,

$$\vec{B} \cdot \boldsymbol{\nabla} \alpha = 0 \tag{2.18}$$

so that α is constant along each field line, although it may vary from field line to field line. If $\alpha = 0$, then the magnetic field reduces to the potential case earlier considered. Also, α can be considered to be uniform i.e. constant on all field lines.

The first possibility leads to equations that do not possess a general solution and are usually solved numerically; this is useful for nonlinear force-free (NLFF) extrapolation of photospheric sources. However, for the sake of this work, we will only consider the case where α is constant everywhere.

For a linear or constant α, we will have to solve Equation (2.17) which is a linear equation for $\vec{B}$. We can have:

$$\boldsymbol{\nabla} \times \left(\boldsymbol{\nabla} \times \vec{B} \right) = \boldsymbol{\nabla} \times \alpha \vec{B} = \alpha (\boldsymbol{\nabla} \times \vec{B}) = \alpha^2 \vec{B}$$

Using curl identity and Maxwell equation, recall $\boldsymbol{\nabla} \times \left(\boldsymbol{\nabla} \times \vec{B} \right) = \boldsymbol{\nabla} \times \alpha \vec{B} = \boldsymbol{\nabla} (\boldsymbol{\nabla} \cdot \vec{B}) - \boldsymbol{\nabla}^2 \vec{B}$. Since $\boldsymbol{\nabla} \cdot \vec{B} = 0$, thus:

$$\boldsymbol{\nabla}^2 \vec{B} = -\alpha^2 \vec{B} \tag{2.19}$$

This is a *Helmholtz equation*.

There is an infinite number of configurations for different choices of α. Assuming that the magnetic field (force-free) decays due to the finite conductivity σ of the fluid. We apply the curl operator to Ohm's law.

$$\boldsymbol{\nabla} \times \vec{J} = \sigma_0(\boldsymbol{\nabla} \times \vec{E} + \boldsymbol{\nabla} \times (\vec{v} \times \vec{B})) \tag{2.20}$$

$$\frac{1}{\sigma_0}(\boldsymbol{\nabla} \times \vec{J}) = \boldsymbol{\nabla} \times \vec{E} + \boldsymbol{\nabla} \times (\vec{v} \times \vec{B})$$

$$\boldsymbol{\nabla} \times \vec{E} = \frac{1}{\sigma_0}(\boldsymbol{\nabla} \times \vec{J}) - \boldsymbol{\nabla} \times (\vec{v} \times \vec{B}) \tag{2.21}$$

Since the magnetic field is force-free, so $F_m = \vec{q}(\vec{v} \times \vec{B}) = 0$ and the particles travel along the field lines.

$$\boldsymbol{\nabla} \times \vec{E} = \frac{1}{\sigma_0}(\boldsymbol{\nabla} \times \vec{J}) \tag{2.22}$$

Substituting Equation (2.22) into Faraday's law and combining it with Ampere's law gives:

$$\frac{\partial \vec{B}}{\partial t} = -\frac{1}{\sigma_0}(\boldsymbol{\nabla} \times \vec{J}) = -\frac{1}{\mu_0 \sigma_0}(\boldsymbol{\nabla} \times (\boldsymbol{\nabla} \times \vec{B})) \tag{2.23}$$

From Equation (2.17), we have

$$\frac{\partial \vec{B}}{\partial t} = -\frac{1}{\mu_0 \sigma_0}(\boldsymbol{\nabla} \times \alpha \vec{B}) \tag{2.24}$$

Using the identity $\boldsymbol{\nabla} \times (\alpha \vec{B}) = \alpha(\boldsymbol{\nabla} \times \vec{B}) + (\boldsymbol{\nabla}\alpha) \times \vec{B}$, we derive the expression:

$$\frac{\partial \vec{B}}{\partial t} = -\frac{1}{\mu_0 \sigma_0}(\alpha^2 \vec{B} + \boldsymbol{\nabla}\alpha \times \vec{B}) \tag{2.25}$$

The term $\boldsymbol{\nabla}\alpha \times \vec{B}$ from Equation (2.25) can twist the shape of the fluid, as the component $\boldsymbol{\nabla}\alpha \times \vec{B}$ will produce a force on the field lines $\vec{B}$ causing a twist. **Magnetic helicity** H is the topological magnitude for measuring the twist and linkage of magnetic field lines.

$$H = \int \vec{A} \cdot \vec{B} d\vec{V} \tag{2.26}$$

where $\vec{A}$ s the magnetic potential vector. Considering a force-free field and constant $\alpha(r)$, Equation (2.25) reduces to:

$$\frac{\partial \vec{B}}{\partial t} = -\frac{\alpha^2}{\mu_0 \sigma_0} \vec{B} \tag{2.27}$$

whose solution is given by:

$$\vec{B} = \vec{B}_0 \exp\left\{-\frac{\alpha^2}{\mu_0 \sigma_0} t\right\} \tag{2.28}$$

It was proposed that a magnetic cloud can be ideally modelled by a symmetric cylinder from the force-free model (GOLDSTEIN, 1983). So, writing the magnetic field and current vectors in cylindrical coordinates:

$$\vec{J} = (J_r, J_v, J_z)$$

$$\vec{B} = (B_r, B_v, B_z)$$

then we have:

$$\vec{J} \times \vec{B} = (J_v B_z - J_z B_v)\hat{r} + (J_z B_r - J_r B_z)\hat{v} + (J_r B_v - J_v B_r)\hat{z} \tag{2.29}$$

$$\boldsymbol{\nabla} p = \frac{\partial p}{\partial r}\hat{r} + \frac{1}{r}\frac{\partial p}{\partial v}\hat{v} + \frac{\partial p}{\partial z}\hat{z} \tag{2.30}$$

Furthermore, considering a cylindrically symmetrical flow tube with the components of $B_r(r) = 0$ and the gas pressure $p = p(r)$ i.e., $\partial p/\partial z = \partial p/\partial v = 0$, substituting in $\boldsymbol{\nabla} p = J \times B$, we have

$$\frac{\partial p(r)}{\partial r} = J_v(r) B_z(r) - J_z(r) B_v(r) \tag{2.31}$$

From Ampère's Law, we have that the current J given in cylindrical coordinates as

$$\vec{J} = \left(0, -\frac{1}{\mu_0}\frac{\partial B_v}{\partial r}, \frac{1}{\mu_0 r}\frac{\partial (rB_v)}{\partial r}\right) \tag{2.32}$$

Thus Equation (2.17) (force-free condition) is transformed into the differential system

$$\begin{cases} \alpha(r)B_v(r) = -\frac{\partial B_v}{\partial r} \\ \alpha(r)B_z(r) = \frac{1}{r}\frac{\partial B_v}{\partial r} \end{cases} \tag{2.33}$$

Considering constant α, the system of differential equations gives:

$$B_v(r) = -\frac{1}{\alpha}\frac{dB_z(r)}{dr} \tag{2.34}$$

$$\frac{1}{r}\frac{d}{dr}\left(r\frac{dB_v(r)}{dr}\right) + \alpha^2 B_z(r) = 0 \tag{2.35}$$

In Lundquist (1950), the solution of the Equations (2.34) and (2.35) are expressed as

$$B_v(r) = J_1(\alpha r) \quad \text{and} \quad B_z(r) = J_0(\alpha r) \tag{2.36}$$

where J_0 and J_1 are zeroth and first-order Bessel functions. Assuming a cylindrical geometry for the magnetic field (BURLAGA, 1988), the solutions for the force-free model determine the components (Figure 2.8):

Axial component (z)

$$B_A = B_0 J_0(\alpha R) \tag{2.37a}$$

Tangential component (ϕ)

$$B_T = B_0 H J_1(\alpha R) \tag{2.37b}$$

Radial component (r)

$$B_R = 0 \tag{2.37c}$$

where $H = \pm 1$, represents the handedness of the magnetic helicity (right-handedness is positive and left-handedness is negative.), B_0 is the estimate of the "amplitude" magnitude of the magnetic field (this is observed to occur at the axis of the cloud i.e., at $R = 0$) and R is the radial distance to the cylindrical flux rope axis. Lepping et al. (1990) then developed a least-square technique that fits the Lundquist solution to the magnetic field observations.

Figure 2.8 - The Bessel-function field.

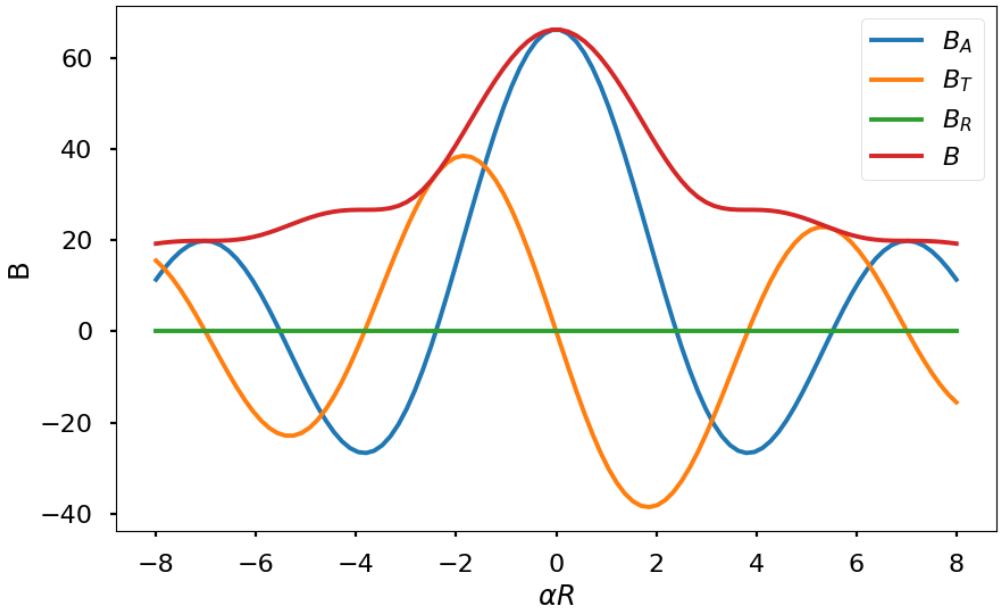

B_A, B_T and B_R are the components of a magnetic field described as cylindrical flux ropes. The axial field B_A starts from B_0 at $r = 0$ and decreases to zero at $\alpha R = 2.4$, after which it reverses sign, while the azimuthal/tangential field B_T increases from zero at the origin to a maximum and then declines.

SOURCE: Author.

As mentioned earlier, *magnetic helicity*, H is used to describe the twist and writhe of magnetic field lines. It allows us to compare models of magnetic fields in different geometries without using parameters specific to a model. Observations have shown that structures in the northern hemisphere of the Sun have predominantly negative helicity, and structures in the southern hemisphere of the Sun have predominantly positive helicity.

The force-free model is suitable to describe the geometry of flux ropes which can be inferred from the results of the Minimum Variance Analysis (MVA) (SONNERUP; CAHILL, 1967; BURLAGA et al., 1981; BOTHMER; SCHWENN, 1998; OLIVEIRA et al., 2021) which is described in Section 2.6. The justification for assuming magnetic clouds to be force-free with constant α is based on the success experienced in fitting the model with magnetic field data (BURLAGA, 1988; LEPPING et al., 1990; AL-HADDAD et al., 2011). However, it is a non-unique solution that applies to some MCs, and the 3D geometry of MCs cannot be accurately inferred from a 1D cut.

2.6 Minimum Variance Analysis

Minimum Variance Analysis (MVA) is a statistical method used extensively in Space Physics to analyse the distribution of plasma and magnetic field measurements from single spacecraft. It calculates the eigenvalues and eigenvectors of the covariance matrix of the data and uses these to estimate the direction where the measurement uncertainties are the smallest. The eigenvectors corresponding to the smallest eigenvalues represent the direction with the minimum variance in space. MVA is used to reduce the dimensionality of large datasets (making it easier to visualize and interpret) while preserving as much statistical information as possible.

Here, we use MVA to find the most representative direction of the magnetic field in magnetic clouds (MCs) and use it to determine the orientation of the magnetic field and how it changes over time. When applied to a set of vectors, e.g., $\vec{B} = (B_R, B_T, B_N)$, it gives a new coordinate system in the direction of the *maximum, intermediate* and *minimum* variance. It is also used to identify the presence of magnetic flux ropes (MFRs).

The current form of the use of MVA was introduced in Sonnerup and Cahill (1967), where the basic techniques were presented as applied to magnetic field measurements; and this technique was further developed in subsequent papers. Here we present a review of the physical and mathematical basis of the MVA technique as presented in Sonnerup and Scheible (1998).

Consider a spacecraft transversing through a transition layer (a magnetic cloud in this case). Since MVA is based on an idealised 1-D model, then $\frac{\partial}{\partial x} = 0$, $\frac{\partial}{\partial y} = 0$. Thus leaving only the z-component that is in the direction of the unit normal to the layer ($\hat{n}$).

$$\boldsymbol{\nabla} \cdot \vec{B} = \frac{\partial B_z}{\partial z} = 0 \tag{2.38}$$

i.e. B_z is independent of z. Since the magnetic field, $\vec{B}$ is divergence-free, its normal component must be continuous across any infinitely thin surface. From Faraday's law, we have $\boldsymbol{\nabla} \times \vec{E} = -\frac{\partial \vec{B}}{\partial t}$ such that B_z must also be time-independent ($\frac{\partial \vec{B}_z}{\partial t} = 0$).

We only need distinct measurements of $\vec{B}^{(1)}, \vec{B}^{(2)}, \vec{B}^{(3)}$, to determine $\hat{n}$. We measure $\vec{B}^{(1)}$ and $\vec{B}^{(3)}$ on opposite sides of the layer but adjacent to it, and measure $\vec{B}^{(2)}$ around the layer's middle.

$$\vec{B}^{(1)} \cdot \hat{n} = \vec{B}^{(2)} \cdot \hat{n} = \vec{B}^{(3)} \cdot \hat{n} \tag{2.39}$$

This means that the three vectors $\vec{B}^{(1)}, \vec{B}^{(2)}, \vec{B}^{(3)}$ have a common component perpendicular to the layer, so the vectors $(\vec{B}^{(1)} - \vec{B}^{(2)})$ and $(\vec{B}^{(2)} - \vec{B}^{(3)})$ are tangential to the layer. We can obtain the normal vector $\hat{n}$ from their normalized cross product.

$$\hat{n} = \pm \frac{(\vec{B}^{(1)} - \vec{B}^{(2)}) \times (\vec{B}^{(2)} - \vec{B}^{(3)})}{|(\vec{B}^{(1)} - \vec{B}^{(2)}) \times (\vec{B}^{(2)} - \vec{B}^{(3)})|} \tag{2.40}$$

Therefore, the accurate measurements of the vectors on opposite sides of the layer and the third vector in the middle are sufficient to find the normal vector, provided that all three were measured simultaneously. But, this is not possible with a single spacecraft passing through the layer, but we can still use the method under the condition that the changes in the transition layer and the attitude are negligible during the time of passage.

Magnetic clouds deviate from the ideal 1-D model described above and are more likely to have 3-D internal structures which evolve, and the orientation of its normal may undergo temporal fluctuation too. The temporal fluctuation may also vary as the spacecraft travels through the structure.

These changes can cause added random and systematic measurement errors. In modern magnetometers (instruments measuring the magnetic field component along the spin axis of the spacecraft), random errors are usually negligible compared to other errors. But random errors may arise from the zero-level offset of the magnetometer. However, this kind of constant offset does not affect the determination of $\hat{n}$ from

Equation (2.40).

The minimum variance technique is designed to accommodate the non-ideal effects mentioned above, except for the presence of a temporal change in the normal direction ($\hat{n}$). Also, the high-time resolution in the magnetometer can measure several vectors $B^{(i)}(i = 1, 2, 3, ..., M)$ during a spacecraft transversal.

The MVA method identifies the direction $\hat{n}$ where the field component set $\{B^{(i)} \cdot \hat{n}\}(i = 1, 2, 3, ..., M)$ has minimum variance.

Normal vector $\hat{n}$ for the direction of minimum variance is determined by minimising

$$\sigma^2 = \frac{1}{M} \sum_{i=1}^{M} \left| (\vec{B}^{(i)} \cdot \hat{n} - \langle \vec{B} \rangle) \cdot \hat{n} \right|^2 \tag{2.41}$$

This is the calculation of the mean quadratic deviation of the individual products of $B^{(i)} \cdot \hat{n}$ from $\langle B^{(i)} \rangle \cdot \hat{n}$, where the mean value $\langle \vec{B} \rangle$ is given by

$$\langle \vec{B} \rangle \equiv \frac{1}{M} \sum_{i=1}^{M} \vec{B}^{(i)} \tag{2.42}$$

and the minimisation is done under the normalisation constraint $|\hat{n}|^2 = 1$. We use a Lagrange multiplier λ to implement the constraint, and then find the solution to this set of homogeneous linear equations.

$$\begin{aligned} \frac{\partial}{\partial n_X}\Big(\sigma^2 - \lambda(|\hat{n}|^2 - 1)\Big) &= 0 \\ \frac{\partial}{\partial n_Y}\Big(\sigma^2 - \lambda(|\hat{n}|^2 - 1)\Big) &= 0 \\ \frac{\partial}{\partial n_Z}\Big(\sigma^2 - \lambda(|\hat{n}|^2 - 1)\Big) &= 0 \end{aligned} \tag{2.43}$$

where σ^2 is given from Equation (2.41) and $\hat{n}$ is expressed as the three components of the cartesian coordinate system (n_X, n_Y, n_Z) in which the magnetic field data is given in.

Differentiating Equation (2.43) yields a set of three equations that can be written in matrix form as

$$\sum_{v=1}^{3} M_{\mu v}^{B} n_v \equiv \lambda n_\mu \tag{2.44}$$

where $\mu, v = 1, 2, 3$ represent the Cartesian components and

$$M_{\mu v}^{B} \equiv \langle B_\mu B_v \rangle - \langle B_\mu \rangle \langle B_v \rangle \tag{2.45}$$

is the magnetic covariance matrix. From Equation (2.44), the values of the eigenvalues are $\lambda_1, \lambda_2, \lambda_3$. The matrix $M_{\mu v}^{B}$ is symmetric, the eigenvalues are real and their corresponding eigenvectors, $\vec{x}_1, \vec{x}_2, \vec{x}_3$ are orthogonal. Eigenvectors $\vec{x}_1, \vec{x}_2, \vec{x}_3$ represent the directions of *maximum*, *intermediate*, and *minimum* variance of the magnetic field component respectively.

The eigenvector $\vec{x}_3$ corresponds to the smallest eigenvalue, λ_3 and it is used to estimate the vector normal to the current sheet, and λ_3 represents the magnetic field variance along the estimated normal.

Summarily, MVA applied to the temporal series of the magnetic field involves the calculation of eigenvalues and eigenvectors of a covariance matrix of magnetic field components. It finds the directions that minimize the variance Equation (2.44). The intermediate eigenvector is orthogonal to all field vectors and therefore provides the direction to the MC axis (OLIVEIRA et al., 2020). It estimates the orientation of the cloud axis quite well when the distance between its axis and the spacecraft trajectory in the MC (the impact parameter, p) is small compared to the cloud axis (KLEIN; BURLAGA, 1982).

There is no unique model for the magnetic field of MCs, but many different configurations have been considered to be consistent MVA (BURLAGA; BEHANNON, 1982).

2.6.1 Applications of the Minimum Variance Analysis (MVA)

MVA is applied to the observed interplanetary magnetic field (IMF) measured by the spacecraft, to identify smooth rotations of the magnetic field vectors and to find the orientation of the cylinder axis of the force-free model (SONNERUP; CAHILL, 1967). The MVA method can be accurately applied for changes in the direction of the magnetic field vector that exceeds $30°$ (BURLAGA; BEHANNON, 1982), and the MCs are identified when there is a smooth rotation in the plane of maximum variance.

The eigenvector associated with the intermediate eigenvalue gives the direction of the axis of the MC (KLEIN; BURLAGA, 1982).

There are two main advantages that MVA has over other more sophisticated techniques in finding the direction of a magnetic cloud's axis:

- It is relatively simpler to apply because it only requires magnetic field measurements.
- It requires minimal assumptions on the magnetic configuration.

A major limitation of the MVA application is that it does not incorporate plasma parameters.

But when the impact parameter, p (distance between the MC axis and the spacecraft trajectory in the MC), is high, the accuracy of the MVA technique reduces and the axis direction derived deviates from the actual one. Gulisano et al. (2007) generated a set of synthetic clouds with different orientations and p to estimate the error caused by the MVA method.

There are some criteria used to validate the application of the MVA technique to identify the axis direction of MCs based on the computed eigenvalues and eigenvectors. For $\lambda_1 > \lambda_2 > \lambda_3$, Lepping and Behannon (1980) defined the error criteria that events with a ratio of

$$\frac{\lambda_2}{\lambda_3} \geq 2 \tag{2.46a}$$

$$\sphericalangle(B_1, B_M) \geq 30^\circ \tag{2.46b}$$

can be well interpreted using MVA. $\lambda_2/\lambda_3 \geq 2$ indicates that there is a strong intermediate variance direction compared to the minimum variance direction and the magnetic hodogram will provide enough information to confidently identify the presence of a magnetic cloud. But, if $\lambda_2/\lambda_3 < 2$ then the magnetic field data is not well aligned with a flux rope configuration and MVA interpretations might be inaccurate. Also, the magnetic field angle of rotation (spherical angle) must be $\geq 30^\circ$ to show that there is a significant rotation of the magnetic field components, since MCs are identified by large rotation of the direction of magnetic field vectors. This is represented by χ in this work.

Also, Siscoe and Suey (1972) gave a 5% criterion significance level of

$$\frac{\lambda_1}{\lambda_2} > 1.37 \quad \text{and} \quad \frac{\lambda_3}{\lambda_2} < 0.72 \tag{2.47}$$

i.e., for any event that falls within this threshold, the variance direction (flux-rope axis direction) is well defined. Sonnerup and Scheible (1998) also show that for relatively smaller data sets with less than 50 data points, the ratio should be $\lambda_2/\lambda_3 \geq 10$ for more reliability of the method.

This reveals that these criteria are good but not sufficient enough for a good determination of MC's axis direction (GULISANO et al., 2007). It is also important to note that the application of the cutoff MVA ratio varies depending on the exact application. Works presented by authors like Oliveira et al. (2020) have identified MCs with a ratio < 2 and also non-MCs that meet the condition given in Lepping and Behannon (1980).

It is important to note that MVA is used to determine the direction of the cloud axis and not to identify whether it is a magnetic cloud or not.

The MVA technique can result in 180° ambiguity of the cloud's orientation because it only provides the direction of the axis of the magnetic cloud and not its orientation. When the MVA provides the intermediate variance direction which is the most representative direction of the axis of the flux rope, there are two possible orientations for this axis. It could be in the positive or negative direction, but MVA always gives positive eigenvalues (because the covariance matrix is a positive semi-definite matrix), so the eigenvectors sign may need to be changed to have a correct geometry.

Several authors have developed ways to solve this ambiguity. Oliveira et al. (2021) developed a computational method that calculates the MC axis angle using MVA and corrects it in comparison to a simulated linear force-free model. Shi et al. (2021) used the z-direction Poynting flux S_z to determine the uncertainties. Oliveira et al. (2020) also developed a new metric to determine the validity of MVA interpretation, concerning its ambiguity; this is done by evaluating the separation of the eigenvalues.

From the principal cloud axis angle (ϕ, θ) derived from the application of the MVA, θ is the angle of the magnetic field vector to the R-T plane (elevation angle out of the Sun-Earth plane) and ϕ is the angle of the magnetic field vector swept out anticlockwise from the Sun-Earth line, projected unto the R-T plane (Sun-Earth

plane) ($\phi = 180^o$ points sunwards).

2.6.2 Degeneracy of MVA

It is most common to have 3 distinct eigenvalues of the covariance matrix, which represents the non-degenerate matrix and the variance ellipsoid. However, MVA results can be non-unique i.e., there can be more than one eigenvector that corresponds to the minimum variance direction such that there are multiple orientations of the magnetic field. These are the three possible types of degeneracy:

$\lambda_1 \approx \lambda_2$**:** It results in an oblate variance ellipsoid, the minimum variance direction $\vec{x}_3$ is well determined, but any vector lying perpendicular to $\vec{x}_3$ (equatorial plane of the shape) may serve as $\vec{x}_1$ and $\vec{x}_2$. This does not affect the application of MVA for normal-vector and normal-field components as long as $\lambda_3 \ll \lambda_2 \approx \lambda_1$

$\lambda_2 \approx \lambda_3$**:** It gives a prolate variance ellipsoid, with its axis along $\vec{x}_1$ while the intermediate $\vec{x}_2$ and minimum $\vec{x}_3$ variance is constrained to be perpendicular to $\vec{x}_1$, otherwise arbitrary. The application of MVA, in this case, does not yield a valid normal direction.

$\lambda_1 \approx \lambda_2 \approx \lambda_3$**:** It gives a spherical or near-spherical variance ellipsoid and cannot provide information about the normal or tangential directions.

Figure 2.9 shows different cases of degenerate ellipsoids: row 1 is spherical, 2 is oblate and 3 is prolate. Figure 2.10 shows different cases of non-degenerate ellipsoids, where all eigenvalues are distinct.

In cases where λ_2 and λ_3 are almost the same, it yields a large uncertainty in the corresponding eigenvectors to the rotation about the remaining eigenvector $\vec{x}_1$. In extreme cases, the orientation of the intermediate and minimum variance directions may switch places causing an $\approx 90°$ rotation of $\vec{x}_2$ and $\vec{x}_3$ around $\vec{x}_1$. These behaviours invalidate the use of the intermediate variance eigenvector $\vec{x}_3$ to predict the normal direction.

Oliveira et al. (2021) noted that the threshold $\frac{\lambda_2}{\lambda_3} \geq 2$ given by Lepping and Behannon (1980) does not consider the first degeneracy. So, the author found a property in the study of geodesy, to determine if a variance ellipsoid is degenerate or not by flattening the elliptical surface (KARNEY; DEAKIN, 2010).

Figure 2.9 - Examples of degenerate ellipsoids with each row showing ellipsoids of different eigenvalues.

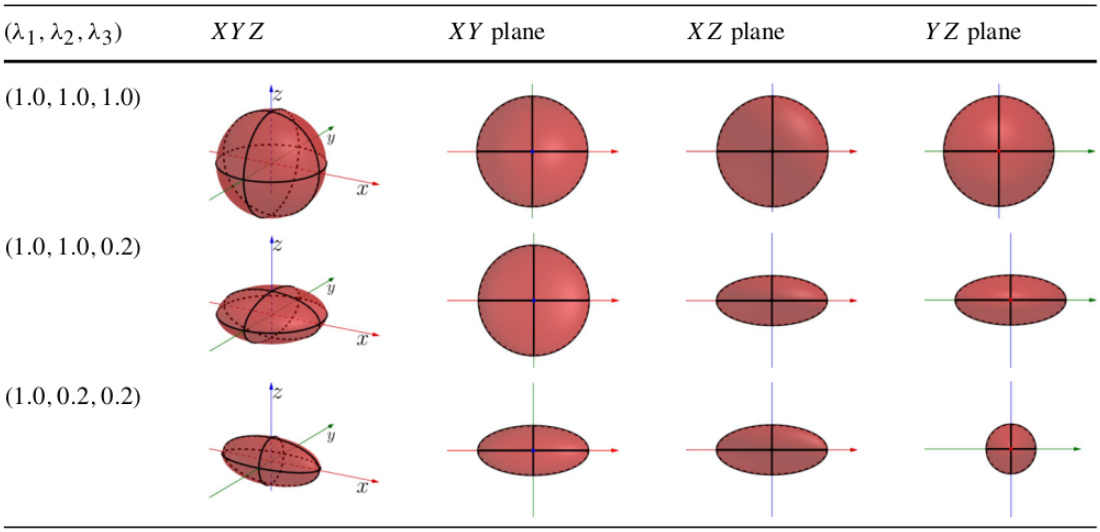

SOURCE: Oliveira et al. (2020).

Figure 2.10 - Examples of degenerate ellipsoids with each row showing ellipsoids of different eigenvalues.

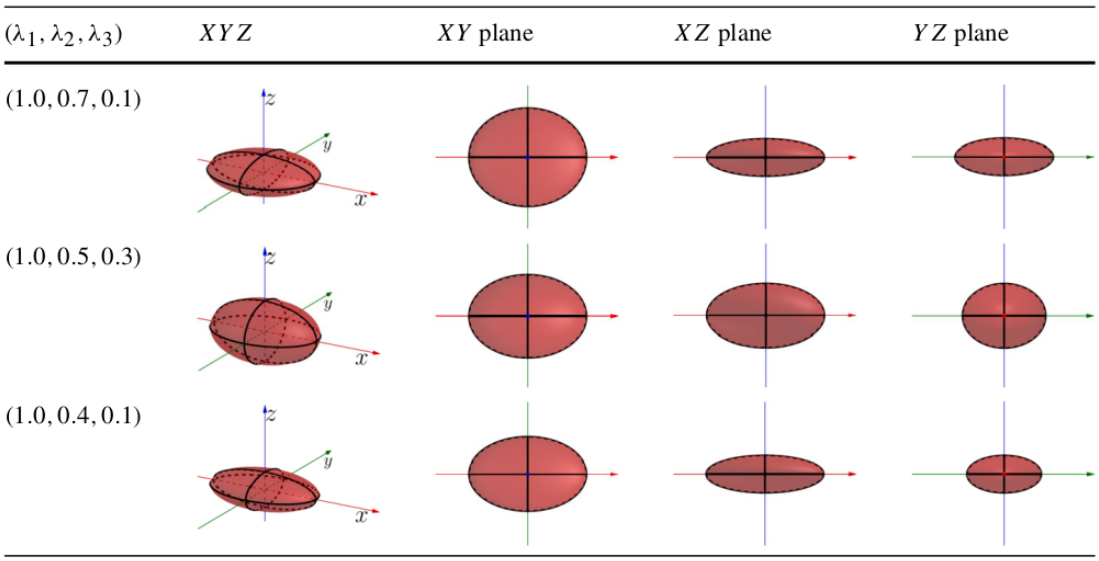

SOURCE: Oliveira et al. (2020).

Oliveira et al. (2020) also proposed a metric (Equation (2.48)) to analyse the cases of degeneracy or non-degeneracy using the product of the flatness relative to each axis. The metric is also important to show the proximity of the degeneracy of the ellipsoid geometry.

$$P(\lambda_1, \lambda_2, \lambda_3) = 100 \times \frac{(\sqrt{\lambda_1} - \sqrt{\lambda_3})(\sqrt{\lambda_1} - \sqrt{\lambda_2})(\sqrt{\lambda_2} - \sqrt{\lambda_3})}{\sqrt{(\lambda_1)^3}} \tag{2.48}$$

where λ_1, λ_2 and λ_3 are the highest, intermediate and lowest eigenvalue obtained respectively. Using the metric described in Equation (2.48), (OLIVEIRA et al., 2021) then highlighted a new threshold for the characterisation of MC based on the degeneration of MVA, which is expressed as:

$$4.5 < P(\lambda_1, \lambda_2, \lambda_3) < 19.5 \tag{2.49}$$

This metric will be used alongside Bothmer and Schwenn (1998) criteria to determine if MVA can be applied to the ICMEs under consideration.

2.6.3 Magnetic hodogram representation

Magnetic hodograms are 2D plots that show the magnetic field projections unto a certain set of eigenvectors. They are used to identify flux ropes by analysing the loop structure (semicircular rotation) of the magnetic hodograms. It was adopted in earlier observations of magnetic flux ropes to observe the clear rotation of their magnetic field when the plot indicates an arc in the *maximum variance plane* (B_y versus B_x). The *minimum variance plane*, however, shows that one of the components of $\vec{B}$ is constant or zero as the magnetic cloud travels past the spacecraft (KLEIN; BURLAGA, 1982).

An example of a magnetic hodogram is shown in Figure 2.11 where there is an arc in the maximum variance plane (B_y versus B_x) and a constant variation in the minimum variance plane (B_z versus B_x). However, Nieves-Chinchilla et al. (2018) went further to identify different forms of flux ropes discussed in Section 2.7. The plot below shows almost a complete rotation (360°) in the magnetic field components of the MC. Nieves-Chinchilla et al. (2018) classified it as a complex magnetic field configuration in comparison to simple flux rope rotations. The projection of the magnetic field onto the eigenvectors as shown in the plot below is: projection onto

a tangential plane is the plot of $B_1 = \vec{B}^{(m)} \cdot \vec{x}_1$ versus $B_2 = \vec{B}^{(m)} \cdot \vec{x}_2$. The side view projection is the plot of $B_1 = \vec{B}^{(m)} \cdot \vec{x}_1$ versus $B_3 = \vec{B}^{(m)} \cdot \vec{x}_3$ i.e. versus the normal field component, and the last projection is $B_2 = \vec{B}^{(m)} \cdot \vec{x}_2$ versus $B_3 = \vec{B}^{(m)} \cdot \vec{x}_3$.

Figure 2.11 - The magnetic hodogram in the GSE coordinate system of an ICME observed by *Wind* spacecraft on September 30, 2006.

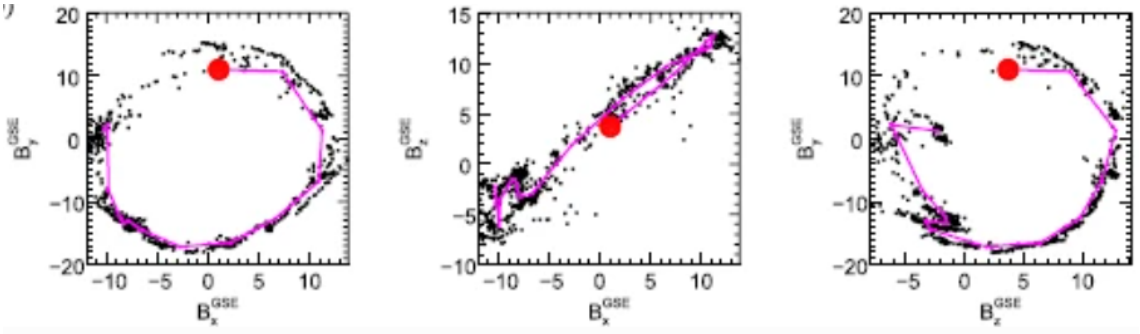

The overplotted pink line shows the hourly data average, and the start time is marked with a red dot.

SOURCE: Nieves-Chinchilla et al. (2018).

2.7 Magnetic flux ropes classifications

There are varying scales of magnetic flux ropes found in various Space environments. We are studying magnetic flux ropes (MFRs) which are the underlying structures of magnetic clouds (KLEIN; BURLAGA, 1982) and there is another type called small-scale magnetic flux ropes, SFRs (MOLDWIN et al., 2000; HU et al., 2018). Their major difference is that small-scale magnetic flux ropes are small in size, they only last for a few minutes to a few hours and can be found in Earth's magnetosphere and solar wind. Also, magnetic flux ropes are noted to be originated from the Sun, while the origin of SFRs is still controversial: the Sun and/or interplanetary space (SHI et al., 2021).

There are different ways to classify flux ropes, and the well-known classification by Bothmer and Schwenn (1998), Mulligan et al. (1998) into eight (8) types is made according to

- the axis direction (ϕ_{axis}, θ_{axis}) of the magnetic cloud that can be obtained from the minimum variance analysis (MVA) technique, and
- the smooth directional change of the magnetic field vector in the interval.

The directional changes can be observed in the B_r, B_t, and B_n components of the magnetic field and in the variation of the latitudinal and longitudinal component of the magnetic field vector (i.e., variations in angles θ and ϕ given in solar ecliptic coordinates).

The latitudinal (θ) component presents an angular variation between -90^o and 90^o and shows the behaviour of the cloud's magnetic field in the S-N direction. The longitudinal (ϕ) component presents an angular variation between 0^o and 360^o, showing the behaviour of the cloud's magnetic field in the E-W direction. This means that when the angles, also known as the magnetic field's polar, ($\theta = 90° \equiv N,\ \theta = -90° \equiv S$) and azimuthal ($\phi = 0° \equiv$ sunward direction, $\phi = 90° \equiv E,\ \phi = 270° \equiv W$). Note that these configurations are deduced from the application of the force-free models.

The variation of the latitudinal and longitudinal components was used to predict four (4) possible flux-rope configurations which have been confirmed to be present in the solar wind. The axis of an MC (ϕ_{axis}, θ_{axis}) can have any orientation with the ecliptic plane.

The type of flux ropes are defined by the direction of the magnetic field aligned to the electric current, which passes through the cross-section of the rope (MARUBASHI, 1986) (as expressed in the force-free model). Depending on the direction in which the magnetic field was observed at the front boundary, rear boundary and middle, we can classify an MC into eight (8) flux rope categories as shown in Figure 2.12 and stated in 2.13.

- Bipolar magnetic clouds ($|\theta_{axis}| \leq 45^o$): these are MCs with low inclination i.e., the axis of the flux rope is lying close to the ecliptic plane and the interplanetary magnetic field (IMF) north-south component (B_z) changes sign from the leading edge to the trailing edge. This means that the *magnetic field vector may rotate from N to S or S to N while the flux rope axis is westward (W) or eastward (E).* Examples of such configurations are SEN, NES, NWS, and SWN (Figure 2.12, 2.13).
- Unipolar magnetic clouds ($|\theta_{axis}| > 45^o$): these are MCs whose axes are highly inclined to the ecliptic plane and B_z maintains its sign from the leading edge to the trailing edge. Their magnetic fields are observed to rotate from East (E) to West (W) or W to E, while the axis is pointing to either south or north. Examples of such configurations are ENW, WNE,

WSE, and ESW (Figure 2.12, 2.13).

Figure 2.12 - Categories of the flux rope types.

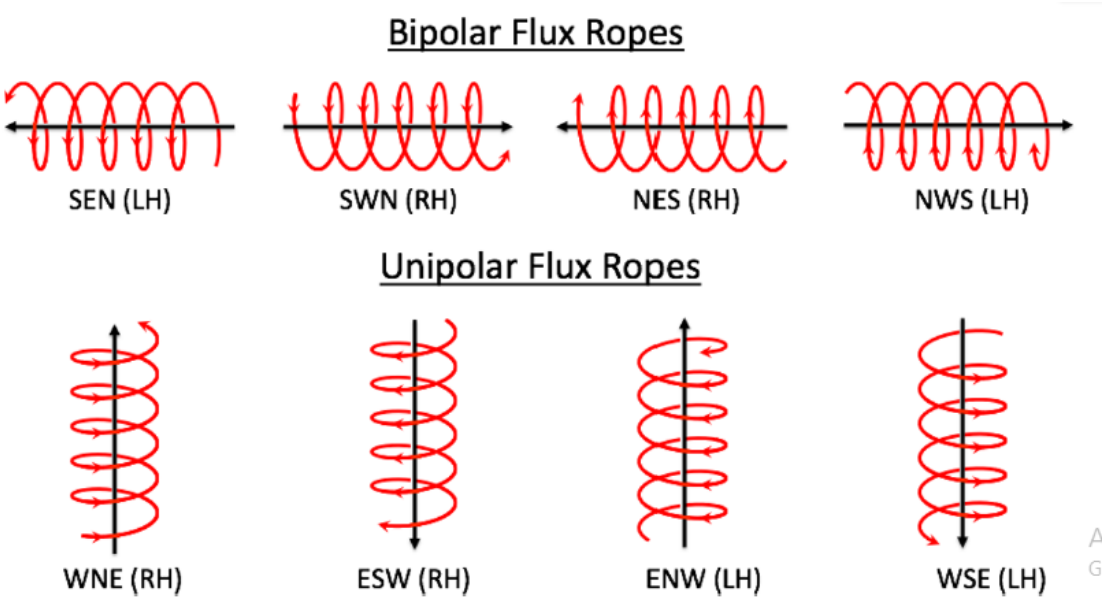

Upper panel - Bipolar (low-inclination); Lower panel - Unipolar (high inclination to the ecliptic plane). The 3 letters caption of each flux rope type is the direction of the magnetic field at the MC leading edge, centre, and trailing edge (East (E), West (W), North (N), South (S), assuming that the spacecraft moves into the page. The magnetic helicity H sign can be left-handed/negative (LH; clockwise rotation) or right-handed/positive (RH; anti-clockwise rotation).

SOURCE: Palmerio et al. (2018).

According to the study carried out by Nieves-Chinchilla et al. (2019) on 353 ICME *Wind* observations from 1995–2015, the authors classified the configurations of the ICMEs magnetic field into the following:

a) F_r: single rotation between 90° and 180°.

b) F^-: single rotation $< 90°$.

c) F^+: single rotation $> 180°$.

d) C_x: complex with multiple rotations.

e) E: ejecta with unclear rotation.

Figure 2.13 - The classification of the rotation of magnetic field rotation in flux ropes.

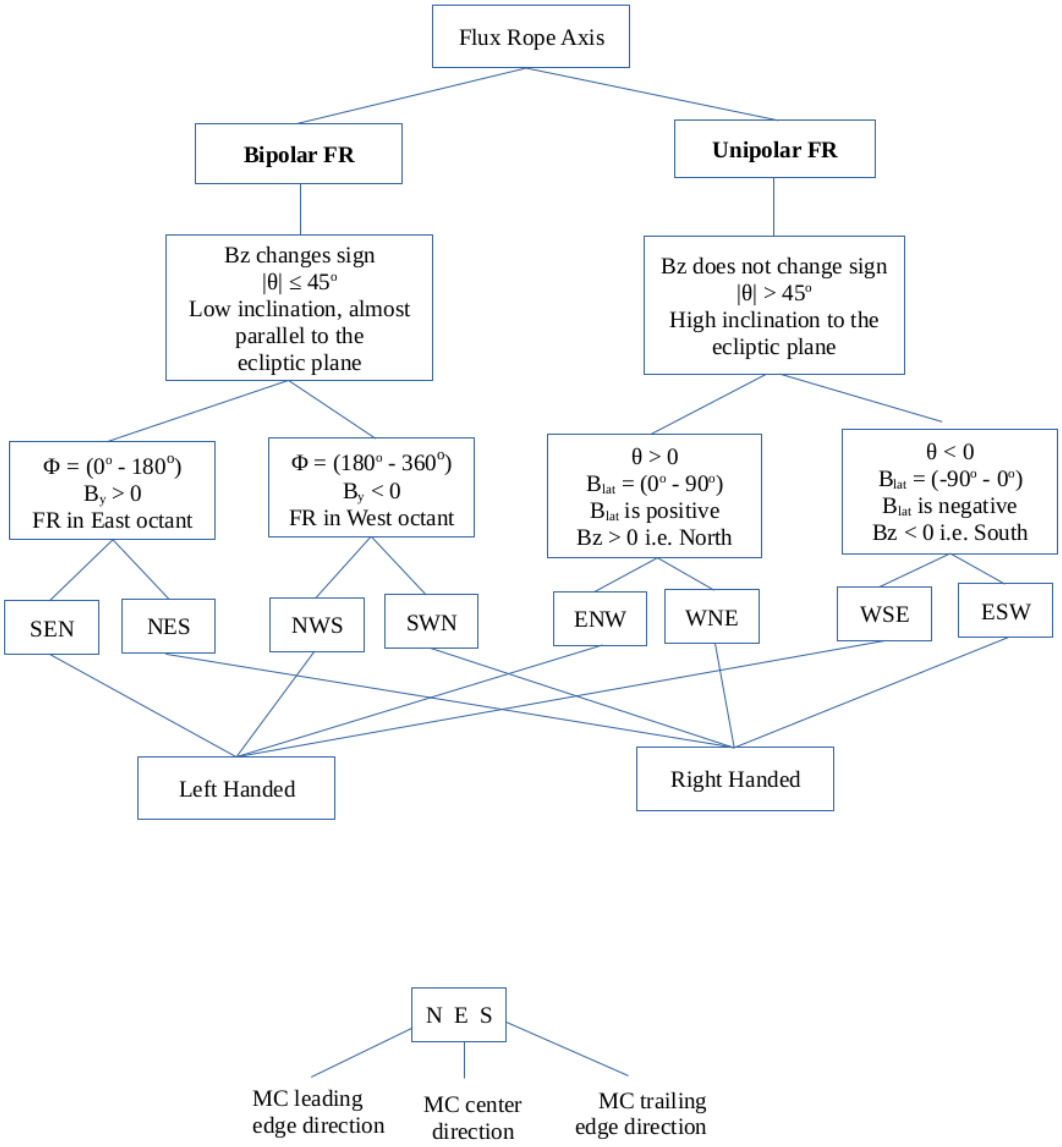

At level 3 of the diagram, bipolar flux rope is distinguished from unipolar by the inclination of its axis to the ecliptic plane. Level 4 introduces the different possible positions and types of FR axis rotation which yields the 8 different types shown in level 5. SEN, NWS, ENW, and WSE are left-handed (LH) helicity while NES, SWN, WNE, and ESW are right-handed (RH) helicity. RH is positive and LH is negative.

SOURCE: Author, based on Bothmer and Schwenn (1998) and Mulligan et al. (1998) classification.

The first three (F_r, F^-, F^+) are single flux rope structures found in the ICMEs as shown in Figure 2.14 panel *a*–*c*, and the last two (C_x, E) are structures with complex or no rotations, as shown in Figure 2.14 panel *d*, *e*. The Fr and F+ events best fit the circular-cylindrical and elliptic-cylindrical flux rope model developed in Nieves-Chinchilla et al. (2016) and Nieves-Chinchilla et al. (2018).

Figure 2.14 - The classification of the magnetic field configuration in *Wind* ICMEs.

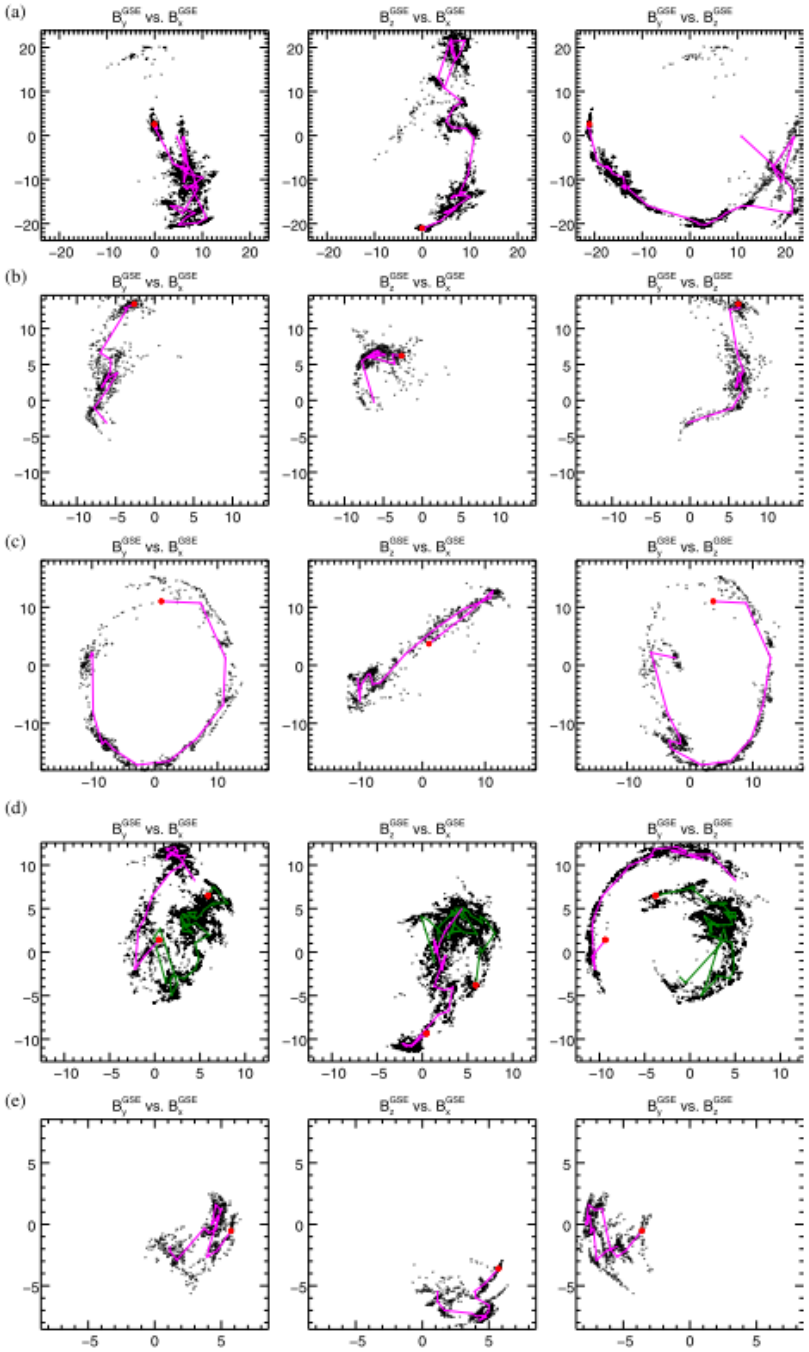

a) F_r observed on October 18, 1995, b) a F^- observed on September 4, 2012, c) a F^+ observed on September 2006, d) a C_x observed on February 7, 1995, e) a E observed on February 10, 1997.

SOURCE: (NIEVES-CHINCHILLA et al., 2019).

2.8 Alfvénic structures

Alfvén waves are described as electromagnetic waves with low frequency in a conducting fluid with a background magnetic field (STASIEWICZ; GUSTAFSSON, 2000). The ion mass provides the inertia in the Alfvén wave while the background magnetic field tension gives the restoring force.

This is another structure that is commonly observed in the solar atmosphere, solar wind and planetary magnetospheres. They are typical of *slab turbulence* as opposed to magnetic flux ropes that represent *quasi-2D turbulence* (MONTGOMERY; MATTHAEUS, 1995). Although, magnetic flux ropes are primarily identified from enhanced magnetic field helicity (TELLONI et al., 2012), this property is also observed in Alfvén waves or structures (ZHAO et al., 2020), thus, both structures are observationally found to contain a helical magnetic field. However, flux ropes are non-propagating structures that are transported with plasma flow, while Alfvénic Structures propagate at local Alfvén speed along the mean magnetic field. They are also more likely to be found in high-speed streams and can be related to the energization of particles.

Another major difference is the speed of these structures. Burlaga and Behannon (1982) stated that the average Alfvén speed at the front and the rear boundary is estimated to be about 104 km/s which is nearly twice magnetic clouds' expansion speed.

Alfvén speed is the typical speed at which magnetic forces accelerate plasma and it is expressed as

$$v = \frac{B}{(\mu_0 \rho)^{\frac{1}{2}}} \equiv v_A \tag{2.50}$$

where B is the magnetic field magnitude, μ_0 is the permeability of the vacuum, ρ is density and v_A is Alfvén wave group speed.

3 INSTRUMENTATION AND DATA PROCESSING

The data used in this work were obtained from the Parker Solar Probe (PSP), WIND spacecraft, Solar Terrestrial Relations Observatory (STEREO), Solar & Heliospheric Observatory (SOHO) spacecraft, Solar Dynamics Observatory (SDO), ACE spacecraft, BepiColombo mission and Solar Orbiter (SolO). This chapter contains a description of the used spacecrafts, information on the data and the applied methods. This section also explains how the spacecraft's data were collected, wrangled, analysed and visualized.

3.1 Parker solar probe spacecraft (PSP)

The Parker Solar Probe (PSP) is the first spacecraft to travel through the Sun's atmosphere, known as the corona, seven times closer than any other spacecraft before it. This spacecraft launched on August 12, 2018, is travelling through regions of intense heat and solar radiation to give humanity the closest-ever observation of a star (DUNBAR, 2021). It was launched into a heliocentric orbit using multiple Venus gravity assist that eventually reduce its perihelion to less than 10 solar radii ($\approx$ 6.6 million km to the Sun). It will provide new data on solar activity, thus contributing to predicting space weather effects that could have major impacts on Earth.

In 2017, it was renamed after Eugene Parker, a Professor Emeritus at the Department of Astronomy and Astrophysics at the University of Chicago. Parker is a pioneering astrophysicist that proposed the concept of how stars—including our Sun give off energy, which is called the "solar wind".

PSP combines in-situ measurements and imaging to greatly enhance our understanding of the Sun. Aboard the spacecraft are four scientific instruments: Fields Experiment (FIELDS, Figure 3.1) (BALE et al., 2016), Integrated Science Investigation of the Sun (IS$\odot$IS, Figure 3.2) (MCCOMAS et al., 2016), Solar Wind Electrons Alphas and Protons Investigation (SWEAP, Figure 3.4) (KASPER et al., 2016) and Wide-field Imager for Solar Probe (WISPR, Figure 3.3) (VOURLIDAS et al., 2016). These four instruments will measure magnetic and electric fields, plasma waves and energetic particles and image the solar wind. PSP will trace the movement of heat and energy through the solar corona and explore the acceleration of solar wind and solar energetic particles. Figures 3.1, 3.2, 3.3, and 3.4 contain the images of these instruments and their individual functions.

Figure 3.1 - Fields Experiment (FIELDS).

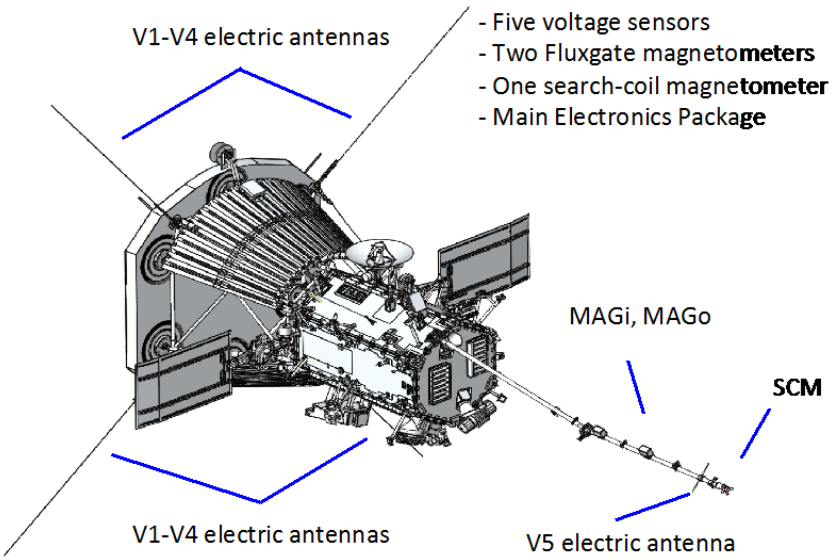

It measures electric and magnetic fields and waves Poynting flux, absolute plasma density and electron temperature, spacecraft floating potential and density fluctuations, and radio emissions (BALE et al., 2016).

SOURCE: NATIONAL AERONAUTICS AND SPACE ADMINISTRATION (NASA). Parker Solar Probe (PSP) Mission (2018).

Figure 3.2 - Integrated Science Investigation of the Sun (IS⊙IS).

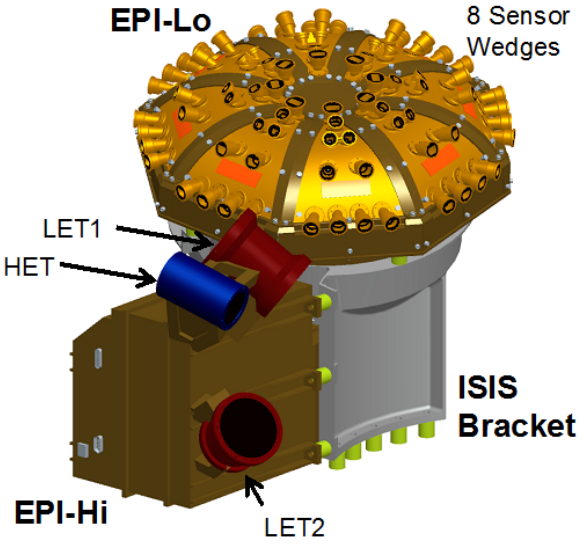

It measures energetic electrons, protons and heavy ions that are accelerated to high energies in the Sun's atmosphere and inner heliosphere (MCCOMAS et al., 2016).

SOURCE: NATIONAL AERONAUTICS AND SPACE ADMINISTRATION (NASA). Parker Solar Probe (PSP) Mission (2018).

Figure 3.3 - Wide-field Imager for Solar Probe (WISPR).

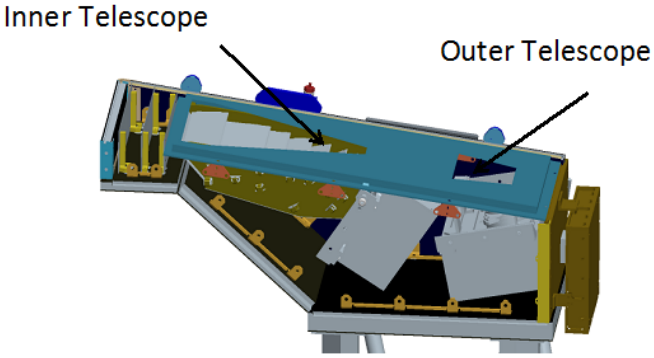

It takes images of the Sun's corona and inner heliosphere. It will provide images of the solar wind, ICMEs and other structure that approaches or pass the spacecraft (VOURLIDAS et al., 2016).

SOURCE: NATIONAL AERONAUTICS AND SPACE ADMINISTRATION (NASA). Parker Solar Probe (PSP) Mission (2018).

Figure 3.4 - Solar Wind Electrons Alphas and Protons (SWEAP) Investigation.

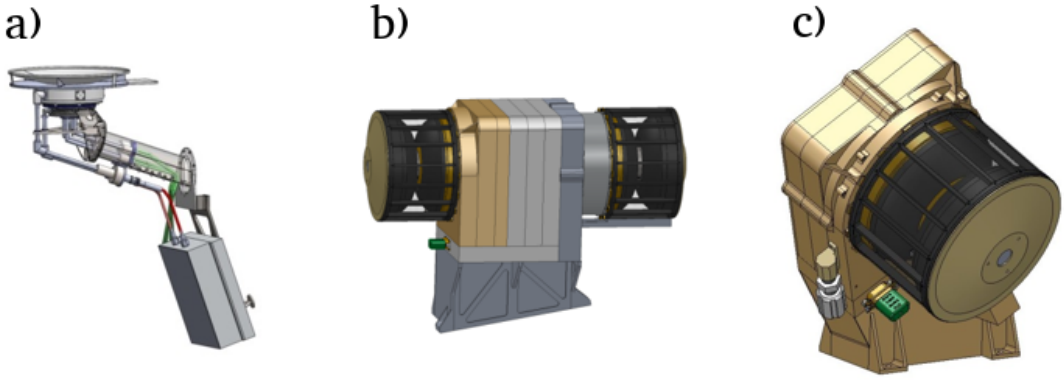

(a) SPC (CASE et al., 2020), (b) SPAN-A+ (LIVI et al., 2020), (c) SPAN-B (WHITTLESEY et al., 2020) instruments. They count the most abundant particles in the solar wind: electrons, protons and helium ions and measure their velocity, density and temperature (KASPER et al., 2016).

SOURCE: NATIONAL AERONAUTICS AND SPACE ADMINISTRATION (NASA). Parker Solar Probe (PSP) Mission (2018).

3.1.1 The inertial RTN coordinate system

This is the coordinate system of the PSP spacecraft which is a version of the Radial, Tangential, Normal heliospheric reference frame. A similar frame is used in other interplanetary missions such as Voyager, Ulysses, STEREO and Helios. It is a magnetic field coordinate system that is defined by the orientation of its three

right-handed Cartesian axes in euclidean space and the origin position relative to a system.

While studying the local plasma environment of a spacecraft, the axis system is usually chosen as a factor of the position of the spacecraft. One of the most commonly used are Radial-Tangential-Normal (RTN) Systems which is defined by the radial vector from a central body to the spacecraft and the magnetic or rotational normal axis of that body. It is convenient to use this Cartesian frame to express the local velocity and magnetic field vectors.

In this system, R is radially outward from the Sun towards the instantaneous position of Parker Solar Probe, T is the cross product of the solar rotation axis with R (i.e., parallel to the solar equatorial plane) which is approximately along the planetary orbital direction, N is towards the North and completes the triad.

This frame is inertial because it represents the spacecraft's current position in an instantaneous inertial frame. In this frame, the vector velocities are calculated relative to the fixed stars (the Sun used here). Also, the velocity data is adjusted for the spacecraft's motion, which will reach a top speed of ≈175 km/s during future encounters. The solar wind flow at perihelia can be compared to the aberration flow, which is the apparent speed of the solar wind in the spacecraft frame as a result of spacecraft motion[1].

3.1.2 PSP spacecraft frame

In the PSP observatory reference frame, the heat shield normal points along +Z and the solar panels is along the Y-axis. The Solar Probe Cup instrument (SPC) is on the -X side of the heat shield. The Solar Probe Analyzers A and B (SPAN-A, -B) are on the +X and -X sides of the spacecraft bus, respectively. The spacecraft's RAM orientation during contacts is in the +X direction[2]. This is shown in Figure 3.5.

The SPC reference frame is similar to the spacecraft frame and there is no transformation carried out on the measurements.

[1] SWEAP data user guide pdf accessed on June 15, 2023
[2] SWEAP data user guide pdf accessed on June 15, 2023

Figure 3.5 - PSP view from the Sun during an encounter.

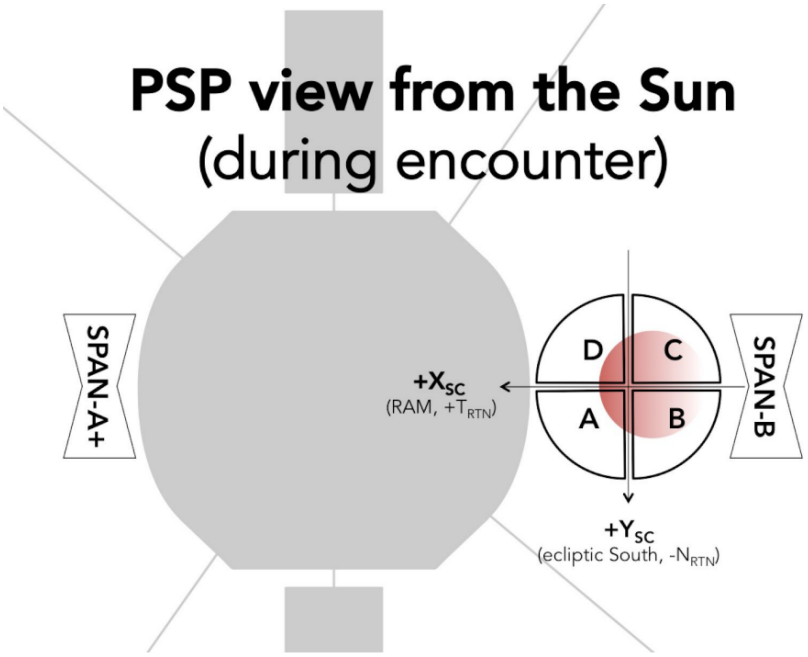

SOURCE: Solar Wind Electrons Alphas and Protons (SWEAP) science team (2020).

3.2 WIND spacecraft

WIND spacecraft is one of the most successful and longest-running space observatories. It was launched on November 1, 1994. It had several orbits through the magnetosphere until it was placed in a Lissajous orbit around the L1 Lagrange point in early 2004. This point is more than 200 R_e upstream of Earth; from there it observes the unperturbed flows from the Sun just before it impacts Earth's magnetosphere. In 2020, it was inserted into a 'halo orbit' around L1.

Lagrangian points are where all the gravitational forces acting between two objects cancel each other out. Thus, spacecrafts are placed in these regions to 'hover'. There are five Lagrangian points which are labelled L1 to L5. L1 is one of and perhaps the most immediately significant of the Lagrangian points discovered by mathematician Joseph-Louis Lagrange. This point is 1.5 million kilometres from Earth or about 1% of the distance to the Sun. Streams, particles and solar wind from the Sun reach L1 about an hour before it reaches Earth.

There are eight instruments aboard this spacecraft, of which two will be used for this research. These are the Magnetic Field Investigation (MFI, (LEPPING et al., 1995))

and Solar Wind Experiment (SWE, Ogilvie et al. (1995)) Faraday Cup - Ion, shown in Figure 3.6.

This spacecraft is included in this research because it makes observations of ICMEs just as they are about to impact the magnetosphere. With the PSP very close to the Sun, and WIND close to Earth, we can make computational analyses and deductions on the evolution of these key structures.

3.2.1 GSE coordinate system

Unlike the Parker Solar Probe, the WIND spacecraft is in a Geocentric Solar Ecliptic (GSE) system. This means that its X-axis is pointing from the Earth towards the Sun and its Y-axis is in the ecliptic plane pointing towards dusk (opposing planetary motion). Its Z-axis is parallel to the ecliptic pole.

Figure 3.6 - The WIND spacecraft and its components.

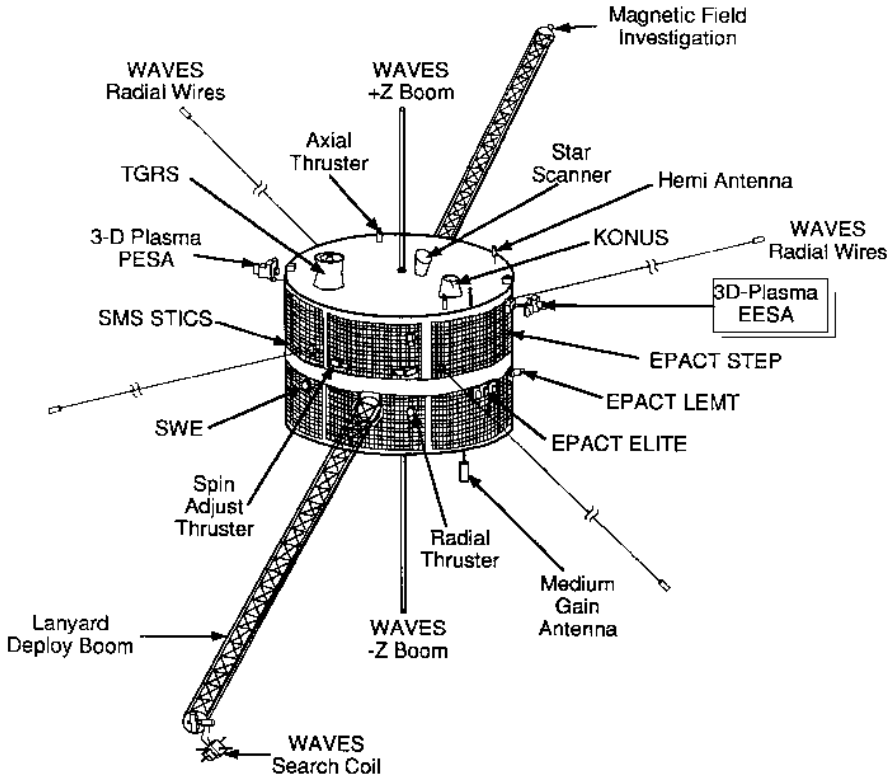

Only data from the magnetic field investigation (MFI) and SWE are needed which are magnetic field and plasma data respectively.

SOURCE: University of Washington (2011).

3.3 STEREO mission

Some of the identified events in the interplanetary medium are carefully traced back to the Sun to unravel their eruption or source conditions. STEREO-A and SOHO coronagraphs are the most used for this purpose.

The Solar Terrestrial Relations Observatory is a NASA mission that contains two identical observatories - with one ahead of Earth's orbit, and the second one behind. The goal was to get the first stereoscopic observation of the Sun and the nature of coronal mass ejections (CMEs). It was launched on October 25, 2006.

Figure 3.7 - The STEREO spacecraft and its components.

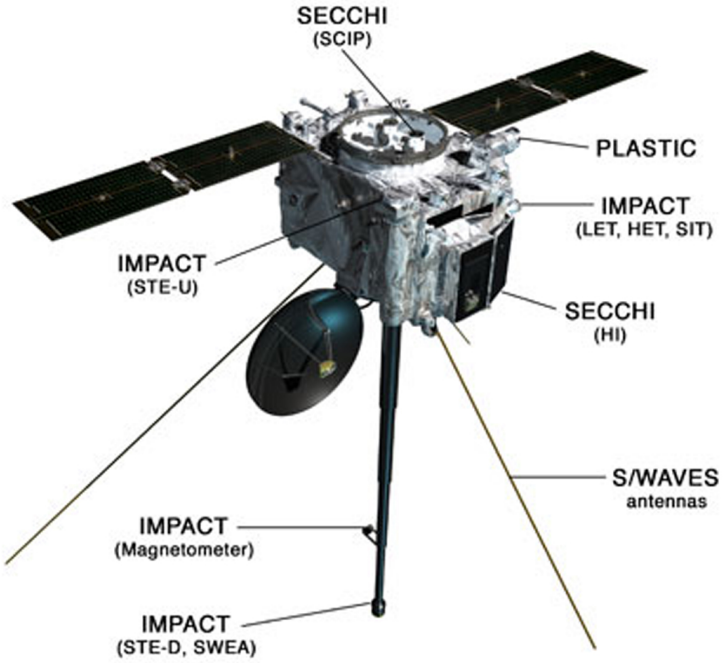

Overview of a deployed STEREO spacecraft. Only data from the SECCHI coronagraphs and imagers aboard STEREO-A was used for this research. Credits: APL.

SOURCE: NATIONAL AERONAUTICS AND SPACE ADMINISTRATION (NASA). STEREO Mission (2021).

Communication with the STEREO-Behind (STEREO-B) has been severed since September 23, 2016, but STEREO-Ahead (STEREO-A) still remains a useful observatory to date. The spacecraft contains 4 instruments: Sun-Earth Connection Coronal and Heliospheric Investigation (SECCHI, Howard et al. (2008)) to study the 3-D evolution of CMEs from the Sun's surface until it impacts Earth; STEREO/WAVES to trace radio bursts from the Sun to Earth's orbit; In-situ Measurements

of Particles and CME Transients (IMPACT, Luhmann et al. (2008)) to sample the distribution of solar wind plasma electrons; and energetic particles, and Plasma and Suprathermal Ion Composition (PLASTIC, Galvin et al. (2008)) to measure the bulk solar wind, plasma protons, alpha particles and heavy ions.

SECCHI is the only instrument used and it also contains four instruments: an extreme ultraviolet imager (EUVI, Wülser et al. (2004)), two white-light coronagraphs (COR1, Thompson et al. (2003) and COR2) and a heliospheric imager (HI, Eyles et al. (2009)).

3.4 SOHO spacecraft

The Solar and Heliospheric Observatory (DOMINGO et al., 1995) is a mission designed to study the Sun from its core to the corona including the solar wind. It was launched on December 2, 1995, and has twelve (12) instruments on board. SOHO is slowly orbiting around the first Lagrangian point (L1) while moving around the Sun in step with Earth, this affords it an uninterrupted view of the Sun. Out of the 12 instruments on board, the one applicable to this research is the Large Angle and Spectrometric Coronagraph (LASCO, Brueckner et al. (1995)). The LASCO instrument is a set of three coronagraphs that image the solar coronal from 1.1 to 32 solar radii, where one solar radius is about 700,000 km, 420,000 miles or 16 arc minutes.

Figure 3.8 - SOHO spacecraft illustration.

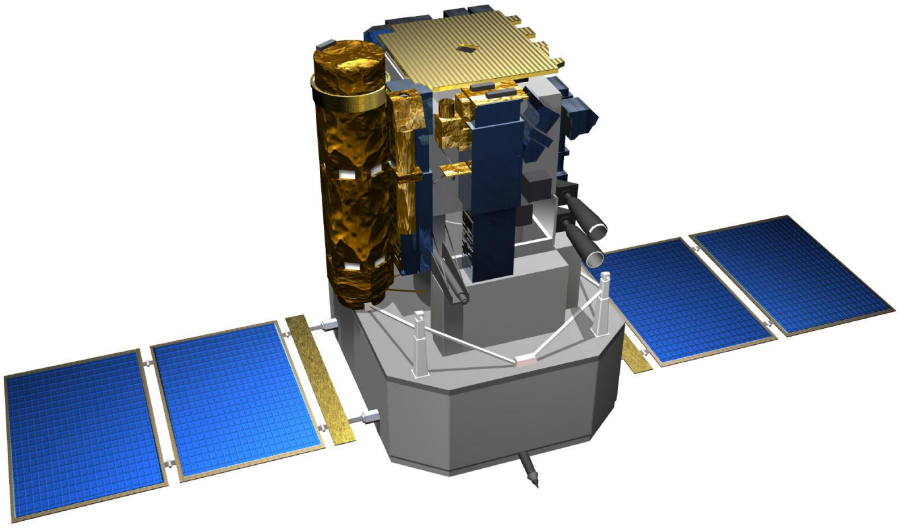

SOURCE: NATIONAL AERONAUTICS AND SPACE ADMINISTATION (NASA); EUROPEAN SPACE AGENCY (ESA); Solar and Heliospheric Observatory (SOHO) Mission (2020).

3.5 ACE spacecraft

NASA's Advanced Composition Explorer (ACE) is a spacecraft designed to collect and study magnetic fields and energetic particles from the Sun to Earth at the L1 Lagrange point. This spacecraft launched in 1997 carries nine scientific instruments on board, eight of which are still in operation. Two of these instruments used in this research are the magnetometer (MAG, (SMITH et al., 1998)) and the solar wind electron, proton and alpha monitor (SWEPAM, (MCCOMAS et al., 1988)). Figure 3.9 shows the spacecraft and its instruments.

Figure 3.9 - ACE spacecraft structure.

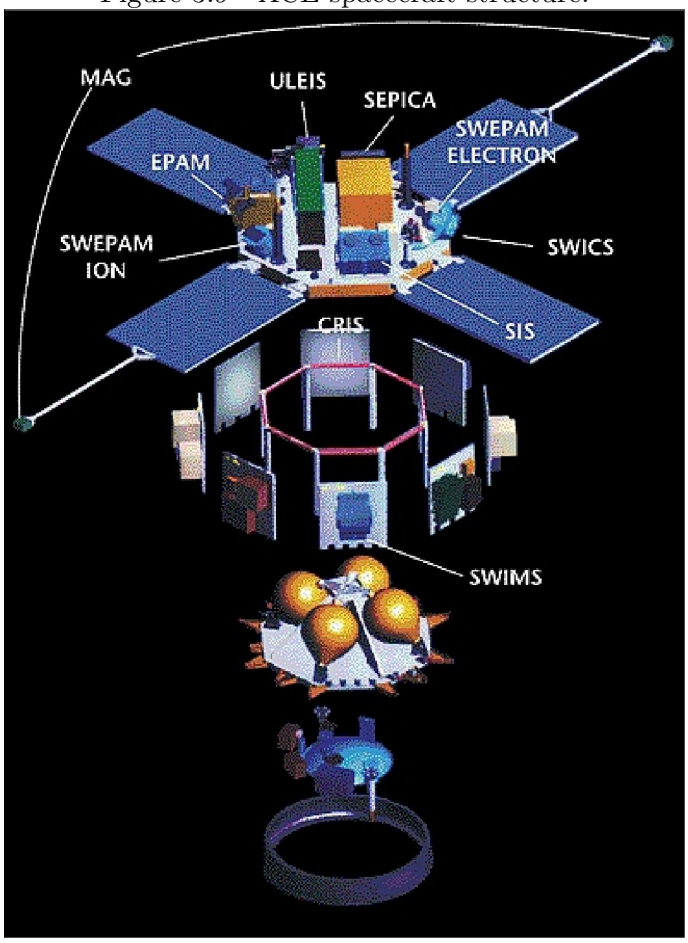

SOURCE: Stone et al. (1998)

3.6 SDO mission

The Solar Dynamics Observatory (SDO) is the first mission launched under NASA's Living With a Star (LWS) Program designed to study the causes of the Variability and its impacts on Earth. This spacecraft launched on February 11, 2010 studies

the solar atmosphere on small scales of space and in several wavelengths simultaneously. On board, the mission is three scientific experiments: Atmospheric Imaging Assembly (AIA, (LEMEN et al., 2012)), EUV Variability Experiment (EVE, (WOODS et al., 2012)) and Helioseismic and Magnetic Imager (HMI, (SCHERRER et al., 2012)). Figure 3.10 is the image of the spacecraft that allows nearly continuous observation of the Sun.

Figure 3.10 - SDO spacecraft and its instruments.

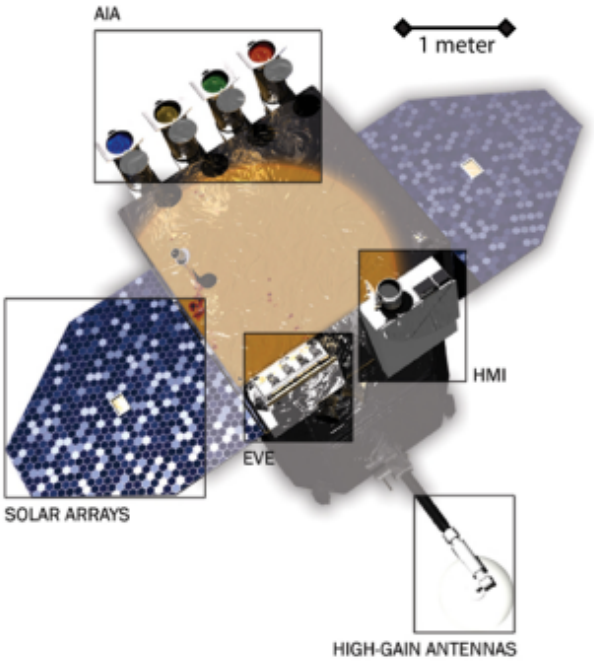

SOURCE: Pesnell et al. (2012)

HMI provides continual full-disk coverage of the Sun at high spatial resolution and new vector magnetogram capabilities. AIA gives images of the Sun's atmosphere in 10 wavelengths every 10 seconds to link changes in the solar surface to changes in the interior. EVE measured the extreme ultraviolet (EUV) irradiance of the Sun with high spectral resolution, temporal cadence and precision.

3.7 BepiColombo spacecraft

BepiColombo is a collaborative mission between the European Space Agency (ESA) and the Japan Aerospace Exploration Agency (JAXA). It is made up of two spacecraft: Mercury Planetary Orbiter (MPO and Mercury Magnetospheric Orbiter (MMO) designed to orbit and study planet Mercury (as seen in Figure 3.11). It was launched in October 2018 and will begin to orbit Mercury in 2025. This study used

the magnetic field (MPO/MAG, (HEYNER et al., 2021)) and plasma measurements (MMO/MPPE, (SAITO et al., 2010)) from the instruments aboard to analyse the properties of events it encountered on its way to Mercury.

Figure 3.11 - BepiColombo spacecraft and its instruments.

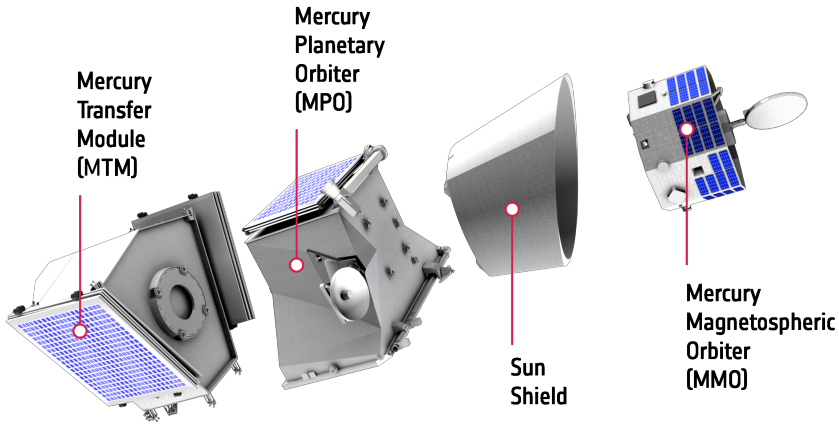

SOURCE: Montagnon et al. (2021)

3.8 PSP data collection

For the Parker Solar Probe (PSP) mission, the magnetic field data is from the magnetometer of FIELDS (BALE et al., 2016), and plasma data is from SPC and SPAN-A (also referred to as SPAN-I because it measures ions) in the SWEAP instrument (KASPER et al., 2016). The data is made available on the PSP website for FIELDS[3], SWEAP-SPC[4] and SWEAP-SPAN-A[5] in NASA CDF format.

CDF—Common data format is a library and data tool developed by NASA to store and manipulate multi-dimensional data sets. To be able to access the data downloaded, the user will have to download the latest version of the tool on this website[6] depending on the operating system in use. An important requirement is to ensure that the installed CDF version is 3.7.0 or above, because other versions or CDF I/O tools may not support the TT2000 timing standard.

The magnetic field and plasma data are available in level 2 and level 3, but the author used level 2 FIELDS data and level 3 SWEAP data, due to incomplete level

[3]FIELDS data page accessed on June 15, 2023
[4]SWEAP-SPC data page accessed on June 15, 2023
[5]SWEAP-SPAN-I data page accessed on June 15, 2023
[6]CDF web page accessed on June 15, 2023

3 FIELDS data at the time of use. The magnetic field data from FIELDS is in spacecraft and RTN coordinates, and available in three intervals: per second, per minute and four samples per cycle. The one-minute interval in RTN coordinate was used because the other intervals had extensive data points. SPC data is available in a single format and interval while SPI level 3 data had two formats: sf0a and sf00. For this work, the sf00 format was used.

The data can be downloaded manually or remotely with some python libraries.

For a **manual** download,

- the author navigates from the FIELDS data page in Footnote 3 to the "mag_RTN_1min/" folder, click on the needed year, (e.g., 2018), month (e.g., 12) and select the second version (e.g., the 19th day: "psp_fld_l2_mag_RTN_1min_20181219_v02.cdf") of the day needed (there is v01 and v02 data for each day).
- For SWEAP-SPC, the author navigates from the data page given in Footnote 4 to L3/ folder, chooses the desired year (e.g., 2018), month (e.g., 12) and clicks on the day needed (e.g., the 19th day: "psp_swp_spc_l3i_20181219_v01.cdf"). It only has a single data version.
- For SWEAP-SPAN-I, the author navigates from the data page in Footnote 5 to L3/ directory, clicks "spi_sf00/" chooses the desired year (e.g., 2018), month (e.g., 12) and click on the day needed (e.g., the 19th day: "psp_swp_spi_sf00_L3_mom_20181219_v04.cdf". There are versions 2, 3 and 4 as of the date of access.

For **remote** data download, the PySPEDAS[7] and PyTplot[8] python library are used. The requirements and information for installing the pySPEDAS library are given here[9]. These processes were followed to download the magnetic and plasma data: (1) set the needed time range, (2) load the magnetic field data (RTN) for the PSP FIELDS instrument and set all the parameters. Note that the data type and the level of data were set to be equal to the manual process described above. A sample code of the PySPEDAS use to download the data and extract a parameter is shown below:

[7] https://pyspedas.readthedocs.io/en/latest/
[8] https://pytplot.readthedocs.io/en/latest/
[9] https://github.com/spedas/pyspedas

```
import pyspedas
# set time range
time_range = ['December 19, 2018, 00:00', 'December 19, 2019, 19:00']
# load magnetic field data from FIELDS
pyspedas.psp.fields(trange=time_range, datatype='mag_rtn_1min',
                    level='l2', time_clip=True)
# load plasma data from SPAN-I
pyspedas.psp.spi(trange=time_range, datatype='spi_sf00_L3_mom',
                 level='l3', time_clip=True)
# Extract magnetic field components
b = get_data('psp_fld_l2_mag_RTN_1min')
br = b3.y[:,0]; bt = b3.y[:,1]; bn = b3.y[:,2]
```

A tutorial on PySPEDAS designed by the Python for Heliophysics Community can be found here[10].

There are also several methods to access the *manually* and *remotely* downloaded CDF data.

For the **manually** downloaded data, the user will have to use the CDFlib or pycdf package. CDFlib is designed to replicate the CDF libraries using pure python, without the need to install the CDF NASA libraries. Pycdf is a package that gives a Python interface to the CDF library. It is important to consult the metadata of each CDF file as they contain comprehensive listings of important information including units, coordinate systems, qualitative descriptions, uncertainties, methodologies, etc.

Here is a sample of the use of CDFlib to open the CDF file and access the needed parameters.

```
import cdflib
import os
import os.path
# set the path
os.environ["CDF_LIB"] = "/home/dorcas/Documents/Research/cdf38_0-dist/lib"
# read the entire file
B = cdflib.CDF('psp_fld_l2_mag_RTN_1min_20181219_v02.cdf')
# extract the needed parameters
```

[10] PySPEDAS tutorial 2022

```
B_rtn = B.varget('psp_fld_l2_mag_RTN_1min')
```

More information about the use of CDFlib can be seen in its documentation[11], and the use of pycdf to read CDF files can be also found on its website[12].

The epoch, density, velocity, temperature, longitude and latitude parameters were extracted in a similar way to the code above using the "varget" function. However, CDF Epochs are given in nanoseconds from the year 2000 with units j2000 (e.g. 595166465964586496). This had to be converted to a useful datetime format so as to make a proper time series plot, using the pandas timestamp function or numpy datetime function. These yields "`2018-11-11 00:01:05.964586496`" and "`numpy.datetime64('2018-11-11T00:01:05.964586496')`" respectively.

3.9 WIND data collection

WIND spacecraft data is collected in the same manner as that of PSP spacecraft. The data is derived from the WIND MFI[13] and SWE[14] repository remotely using PySPEDAS library in Python. The MFI has 3 types of data, h0, h1, and h2, and the h0 type is the relevant type for this research; the SWE has h0 to h5 type of data and the h5 type is used. Here is a sample of the keywords used to access the repository remotely and extract the needed parameters using PySPEDAS. For recent years, 2021 and 2022, the h5 level data is unavailable, so we used the data type 'k0' available in the same website.

```
import pyspedas
# load magnetic field data from WIND using the set time range
pyspedas.wind.mfi(trange = time_range3, time_clip=True)
# load plasma data from SWE
pyspedas.wind.swe(trange=time_range3, time_clip=True)
# Extract density, velocityparameters
D = get_data('N_elec')
V = get_data('U_eGSE')
```

[11] https://cdflib.readthedocs.io/en/latest/
[12] https://spacepy.github.io/pycdf.html
[13] https://spdf.gsfc.nasa.gov/pub/data/wind/mfi/mfi_h0/
[14] https://spdf.gsfc.nasa.gov/pub/data/wind/swe/swe_h5/

3.10 Multi-spacecraft data connection

To study the evolution of the ICMEs as mentioned in the objective, we manually search for events that were observed by multiple spacecrafts and also make use of existing catalogues. The catalogues used are NASA WIND ICME catalogue, 1995 - 2021 compiled by Teresa Nieves Chinchilla; Helio4cast multispacecraft catalogue (contains Solar Orbiter, BepColombo, WIND, PSP, STEREO-A and B, etc.) compiled by Möstl et al. (2022); and ACE, Wind and STEREO ICME list 1996 - 2021 compiled by Richardson and Cane.

We are majorly interested in events observed by PSP and WIND because such events are Earth-bound. To identify events that were observed by both spacecraft, the following steps are taken:

- Estimate arrival time at WIND spacecraft from PSP data using the average velocity and separating distance.
- Utilise the space weather database of notifications, knowledge, and information (DONKI) developed by the community coordinated modelling centre (CCMC). The simulations generated by the Wang-Sheeley-Arge (WSA)-ENLIL+Cone model for 2.0 AU are used to visualise the predicted propagation of the coronal mass ejections (CMEs) and their arrival at different space bodies and spacecrafts.

DONKI has a search space weather activity archive tool[15]. The space weather activity type is set to CMEs and the date range of interests is shown. CCMC has generated a lot of modelled solar events such as coronal mass ejections (CMEs) using the Wang-Sheeley-Arge (WSA)-ENLIL+Cone model for 2.0 AU.

WSA-ENLIL is a physics-based prediction model that operates on a large scale to analyze the heliosphere. It is a global 3D-MHD model that gives a time-dependent description of the background solar wind magnetic field and plasma into which a spherical or ellipsoid CME can be inserted. There are a series of inputs for the model, some of which included the start time of the CME, its speed, longitude and latitude in HEEQ (Stonyhurst heliographic coordinates when HEEQ is converted to longitude and latitude), radius and half angular width.

[15] CCMC DONKI SEARCH

3.11 Data wrangling

Data wrangling was majorly carried out for PSP data as some of the data have gaps, randomness, low signal, and spikes at their raw states. Some of the causes of the poor state of the data for certain dates are:

- Rolling manoeuvres that cause weird spikes and random values in the data, especially in the SPC instrument.
- Data gaps or inaccurate measurement because the full distribution of protons is not in the field of view (FOV). This is a problem in the SPAN-ion instrument and this can be resolved by fitting and modelling the protons.
- At distances far from the Sun ($> 100\ R_s$), the bulk of the solar wind is not usually in the FOV of the SPAN-ion instrument and there is very low time resolution. So it is more useful for observations closer to the Sun

There are 3 major steps that are taken to overcome these data limitations.

- Discard identified ICME events with large data gaps, out of the FOV of the instruments or extreme limitations.
- Clip extreme values carefully without affecting the overall trend of the data.
- Perform a forwards-backwards exponential weighted moving average (FBEWMA) on the data with spikes and noisy values.
- Remove outliers that could not be clipped and are still evident after the moving average has been carried out.
- Interpolation to engineer values for small data gaps. This step is also taken to make the time resolution equal for all the parameters needed to estimate plasma beta.

Figure 3.12 below is a sample of two parameters, volume on the left-hand side and temperature on the right-hand side, showing the application of the steps listed above and discussed in the following subsections. From the first panel is the original data, the clipped data, the exponential weighted moving averaged data, the removal of outlier and the interpolated (final) data.

Figure 3.12 - The process of denoising or removing randomness in certain time series data.

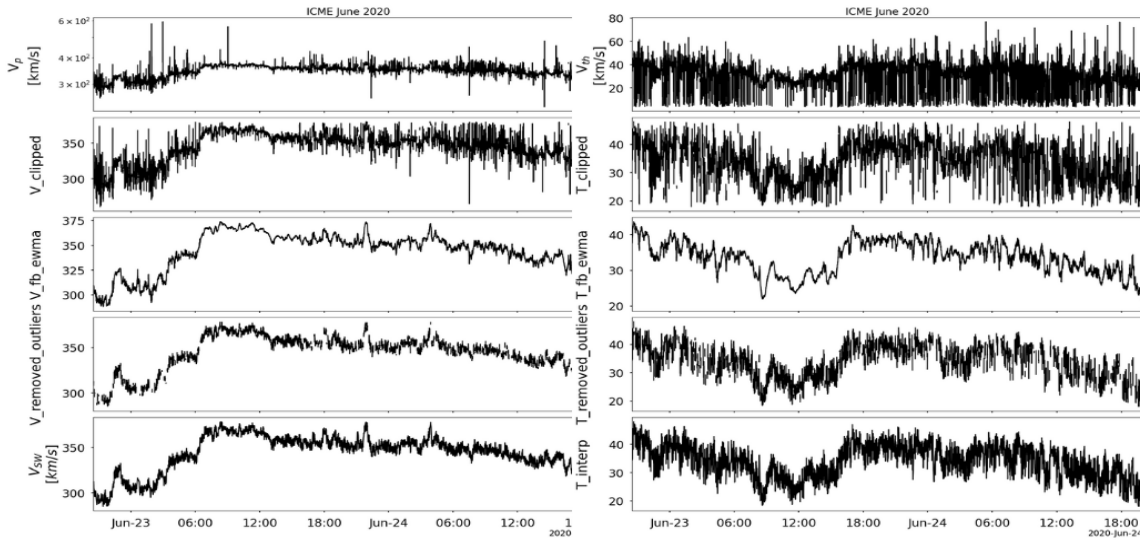

Left panel: Solar wind speed in km/s. Right panel: Thermal speed in km/s. This is the plasma measurement of an ICME that was observed by PSP/SWEAP on June 23, 2020. From the top panel: original data, clipped data, forward-backwards moving averaged data, data with outliers removed, and interpolated data.

SOURCE: Author.

3.11.1 Data clipping

For certain years in Parker Solar Probe data, especially in 2020 and 2021, there are extreme spikes found in the plasma measurements that limit the interpretation of the trend of the data. These spikes are present above and below the actual trend of the data. To resolve this, the author sets a clip value above and below the average trend of the data, such that the extreme spikes are removed. The mild spikes remaining are smoothed out using the exponential weighted moving average discussed in the next section.

3.11.2 Exponential Weighted Moving Average (EWMA)

EWMA is a smoothing technique used in time series by applying weights to the value of a time series. It exerts more weight on recent data points, making it more involved in future forecasts. The formula for weight calculation without adjustment is given as:

$$y_0 = x_0 \tag{3.1a}$$

$$y_t = \alpha x_t + (1 - \alpha) y_{t-1} \tag{3.1b}$$

where x_t is the input value for time t, y_t is the output value (EWMA) for day t and α is the value of the smoothing factor. However, by using the `Pandas` library in Python, it automatically calculates the α parameter from the `span` parameter provided. The `span` parameter is called the "N-day exponential weight moving average", and it is chosen visually based on its smoothing result. Figure 3.13 shows how the smoothness of density of May 28, 2020, ICME varies with the set `span` values.

Figure 3.13 - The averaged density of May 28, 2020, ICME at different SPAN values.

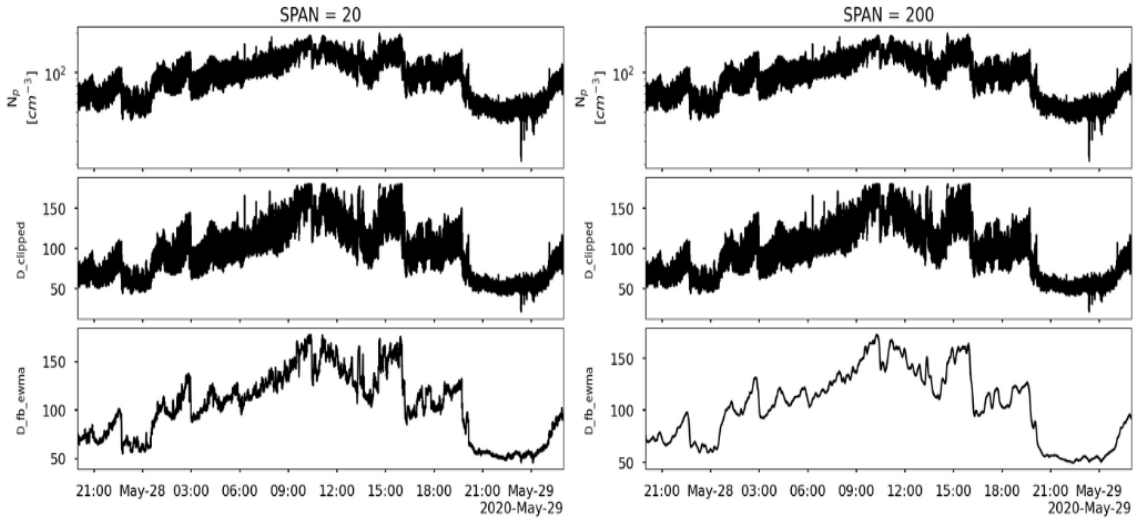

SOURCE: Author.

In this work the author used the **forward-backwards EWMA**, to smooth the randomness and noise in the data so that the weight of the "surrounding data" are taken into consideration. The forward EWMA is simply EWMA calculated from the

beginning of the input value to the end, while the backward EWMA is calculated reversedly, from the end to the beginning (this is done with a step of -1). The forward and backward EWMA are stacked and the mean of each value is calculated.

3.11.3 Removal of outliers

This is the last step for removing unwanted value deviations in the data. After the smoothing average, is done, there are still certain points that deviate from the average trend of the data. This step subtracts the results of the forward-backwards exponential moving averaged data from the original "noisy" data. A maximum deviation value is set such that the result is smoother data void of spikes and randomness.

Finally, after the outliers are removed, the missing gaps are then filled up by interpolating the data.

3.11.4 Interpolation

Discussed here is another application of interpolation in the analysis to correct uneven data size and shape.

Interpolation is a method of estimating new values from existing data. In this work, it is used in 2 different ways: (i) to generate values for missing data (as in 3.11.3), (ii) to reduce the temporal resolution of specific parameters to match other parameters' size. The latter is done using the function `scipy.interpolate.interp1d` from the `scipy` library in Python. It is used to interpolate a 1-D function. It takes in `x` and `y` and returns a callable function that can be called with a new `x`, thus returning a new `y`. The callable interpolator function creates a new `y` from the original `y` input that matches the size of new `x`.

Wherever there are mild data gaps in the magnetic field and plasma data measurements of certain events, they are resolved using the interpolation function, while events with large data gaps are usually discarded. Also, since calling `interp1d` with `NaNs` present results in undefined behaviour, it is ensured that the `NaNs` values are removed.

Secondly, the time resolution of magnetometers and instruments that measure the solar wind parameters are usually different, thus limiting the direct calculation of certain parameters. Magnetic field data (measured by PSP/FIELDS) usually have higher time resolution (i.e. more data points) in comparison with plasma data (measured by PSP/SPAN-ion), while plasma data (measured by WIND/SWE or

PSP/SPC) usually have higher time resolution in comparison with magnetic field data (measured by WIND/MFI or PSP/FIELDS). So, the downloaded magnetic field data is interpolated using the `datetime` of plasma data or vice versa.

Here is a sample code showing the interpolation of `B` using `v.times` for SPAN-ion data.

```
from scipy.interpolate import interp1d
# b.times is the datetime values, b is the magnetic field data values
b_interp = interp1d(b.times, b)
# v.times is the datetime of the plasma data, velocity in this case.
b_new = b_interp(v.times)
```

Interpolation is especially important when calculating plasma beta, an important parameter for identifying the presence of a magnetic cloud in an ICME, but it is not directly measured by spacecraft (Section 2.4). The interpolation ensured that density N, temperature T, and magnetic field $\vec{B}$ are interpolated to the same size and β is calculated using Equation (2.2).

3.12 Identification of magnetic flux ropes

Figure 3.14 is a summary of the processes that the magnetic clouds (MCs) are passed through and are further described below.

Coronal Mass Ejections (CMEs) from the Sun that are observed in the interplanetary medium are called Interplanetary Coronal mass Ejections (ICMEs). They are firstly identified *in-situ* using Parker Solar Probe observational data and cleaned as described in Section 3.11. Afterwards, the author set out to identify the presence of magnetic clouds within the ICME structures.

In Section 2.1, it was stated that ICMEs are sometimes characterised by enhanced magnetic field data. Not all ICMEs contains magnetic clouds, but about 30% of the ICMEs observed at 1AU has magnetic cloud embedded in them. In Section 2.4, it is also stated that magnetic clouds are characterised by the simultaneous observations of these three properties:

- enhanced magnetic field
- large smooth rotation of the magnetic field and

Figure 3.14 - Flow chart to explain the processes of the events analyses.

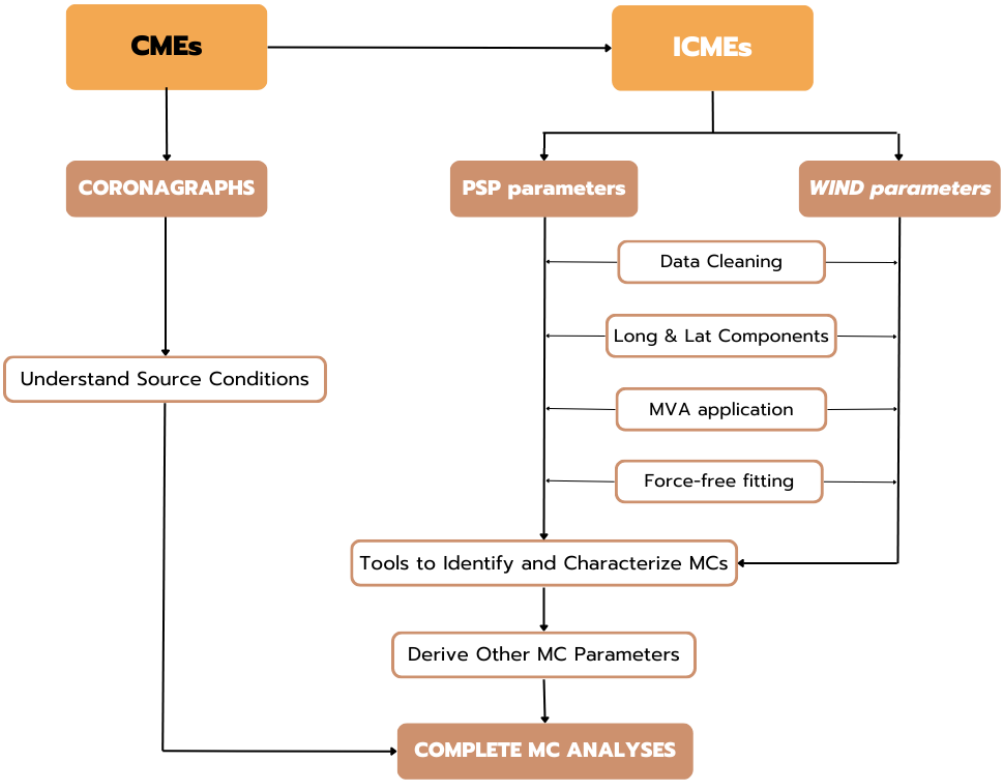

Steps taken from identification of ICMEs to the final analyses of the configuration of the magnetic clouds—magnetic flux ropes.

SOURCE: Author.

- depressed temperature and beta compared to the background solar wind.

Also, it is mentioned that the structure of the twisted magnetic field in magnetic clouds is described as magnetic flux ropes (MFRs), and that is why "magnetic flux ropes" and "magnetic clouds" are used interchangeably in this write-up. This work is only focused on ICMEs with magnetic clouds in them. The primary focus is on PSP observations, after which observations that also impact WIND spacecraft and sometimes Earth are also evaluated and studied. All the studied events are then traced back to the Sun as CMEs with the aid of coronagraphs aboard STEREO-A and SOHO.

The first stage of identifying magnetic flux rope structures is done by visual observation when there is a large smooth rotation in the B_t and/or B_n components of the magnetic field vector. Then plasma beta (described in Section 2.4) must be

calculated and visualised to observe depression in values within the boundaries of the magnetic cloud when compared with the ambient solar wind This is calculated using Equation (2.2)

The visualisation then helps to identify the boundaries of the ICMEs and the magnetic clouds. The choice of boundaries is sort of an "art" because the boundary placement sometimes has an effect on the result of the MVA application.

Asides from visually identified ICMEs and MCs by the author, already existing ICME catalogues were also considered, for example, a mulispacecraft catalogue called Helio4cast[16]. This catalogue is exceptionally useful because it contains ICMEs observed by almost all Heliospheric missions except ACE spacecraft.

For multi-spacecraft events, there are other catalogues that were also used to complement the manual findings. The Results chapter, Section 4 discusses the catalogues used and the list of interplanetary coronal mass ejections and magnetic clouds identified by single and multi-spacecraft.

3.13 Magnetic flux rope events analyses

3.13.1 Magnetic flux rope transformation using MVA

Minimum Variance Analysis (MVA) is a statistical method that is used to analyse the distribution of magnetic field data. It has been theoretically explained in Section 2.6 how it is used to analyse the rotation of magnetic field components of magnetic flux ropes.

Here are the steps of applying MVA to magnetic flux rope events in this research.

- Collect data: This involves collecting magnetic field components (B_r, B_t, and B_n) data that are measured by PSP and WIND.
- Create a covariance matrix: The magnetic field components data collected are used to create a covariance matrix, which is a symmetric matrix that gives information about the correlations between the magnetic field components.
- Eigenvalue decomposition: The covariance matrix is decomposed into its eigenvalues and eigenvectors. This results in three (λ_1, λ_2, λ_3) eigenvalues,

[16] https://helioforecast.space/icmecat

ordered according to eigenvalues $\lambda_1 \geq \lambda_2 \geq \lambda_3$, and three eigenvectors ($\vec{x_1}$, $\vec{x_2}$, $\vec{x_3}$), where

- $\vec{x}_1, \lambda_1$: eigenvector and eigenvalue for the maximum variance direction.
- $\vec{x}_2, \lambda_2$: eigenvector and eigenvalue for the intermediate variance direction
- $\vec{x}_3, \lambda_3$: eigenvector and eigenvalue for the minimum variance direction

The eigenvectors are a 3 by 3 matrix such as:

$$\begin{pmatrix} x_{1i} & x_{2i} & x_{3i} \\ x_{1j} & x_{2j} & x_{3j} \\ x_{1k} & x_{2k} & x_{3k} \end{pmatrix} \tag{3.2}$$

where the columns from left to right represent the eigenvectors from the maximum to intermediate and minimum variance direction respectively.

- Define the minimum variance direction: The eigenvectors that correspond to the smallest eigenvalues represents the direction of minimum variance, which means the direction with the least measurement uncertainties.
- Estimate error in the minimum variance direction.
- Define the magnetic cloud axis given by MVA: The eigenvectors corresponding to the intermediate eigenvalue (λ_3) correspond to the direction of the MC axis. The longitudinal (ϕ_{axis}) and latitudinal (θ_{axis}) angle of the MC's axis is calculated using the eigenvectors corresponding to the intermediate variance direction (i.e. the middle column of the matrix 3.2) with the Equation (3.3).

$$\theta_{axis} = 90^\circ - \operatorname{atan} 2 \left(\frac{\sqrt{x_{2i}^2 + x_{2j}^2}}{|x_{2k}|} \right) \times \frac{180^\circ}{\pi} \tag{3.3a}$$

$$\phi_{axis} = \operatorname{atan} 2 \left(\frac{x_{2j}}{x_{2i}} \right) \times \frac{180^\circ}{\pi} \tag{3.3b}$$

ϕ_{axis} and θ_{axis} angles represent the orientation of the MC axis in spherical coordinates. The latitude is subtracted from 90° to ensure that the value is between -90° and 90°. The value 360° is added to the longitude if

the calculated value is < 0, this is to ensure that the values are between $0°$ and $360°$. These conventions are necessary for the interpretability of the orientation of the axis of the magnetic cloud. Also, `arctan2` is used instead of `arctan` in the longitude formula to handle the sign of both `x` and `y` components (negative or positive) and give the correct quadrant of the angle.

- Generate measured magnetic field components $\vec{B}$ in the minimum variance system (B_L, B_M, B_N): The dot products of the magnetic field components data in RTN coordinate (B_r, B_t, B_n) and the eigenvectors ($\vec{x_1}$, $\vec{x_2}$, $\vec{x_3}$) gives the projection of the magnetic field data onto each of the eigenvectors. This represents the contribution of each of the eigenvectors to the overall variation of the magnetic field.

- Create magnetic hodograms: Magnetic hodograms as described in Section 2.11 are used to visualise the rotation of magnetic flux ropes using the magnetic field components (B_L, B_M, B_N) in the minimum variance system. The plot of B_M against B_L is the maximum variance plane and the plot of B_N against B_M is the minimum variance plane.

However, it is important to check if the MVA will give accurate estimations using the criteria that have been set by previous authors as described in Section 2.6.1. The criteria that are used are:

- the ratio of the intermediate variance and minimum variance $\lambda_2/\lambda_3 \leq 2$ (LEPPING; BEHANNON, 1980).

- angle of rotation of the magnetic field $\chi \geq 30°$ (LEPPING; BEHANNON, 1980).

- the ratio $\lambda_1/\lambda_2 > 1.37$ and $\lambda_3/\lambda_2 < 0.72$ (SISCOE; SUEY, 1972).

- to resolve MVA ambiguity, the author uses the metric $4.5 < P(\lambda_1, \lambda_2, \lambda_3) < 19.5$ (OLIVEIRA et al., 2021).

This means that if a visually identified MC event does not fall within these thresholds, the application of MVA may yield inaccurate interpretation. In such a scenario, the MVA estimation of the MC orientation is discarded. However, if a visually identified MC event falls within the threshold, it means that there is a well-defined flux

rope, else it may or may not have a flux rope; if it has a flux rope then its orientation is not well-defined.

The uncertainties for the MVA condition $\lambda_2/\lambda_3 > 2$ is typical of the order 10°, so if the observed $(\phi_{axis}, \theta_{axis})$ between two spacecraft is $\lessapprox 10°$, the author can conclude that the two spacecrafts observed the same magnetic field configuration. An additional advantage is if the distance between the spacecrafts is small.

3.13.2 Impact parameter

The impact parameter p is the distance between the minimum variance direction of the MC axis and the spacecraft trajectory in the MC. It is important to calculate the parameter because MVA can estimate the orientation of MC axis quite well when p is low (KLEIN; BURLAGA, 1982; BOTHMER; SCHWENN, 1998). If p value is significant, then the orientation derived from MVA is considered inaccurate.

The impact parameter is calculated from the ratio of the minimum variance direction to the magnitude of the magnetic field (GULISANO et al., 2007). The third eigenvalue is obtained from MVA and denotes the minimum variance plane, which is perpendicular to the flux tube.

$$p = \frac{\langle |B_{min}| \rangle}{\langle B \rangle} \tag{3.4}$$

3.13.3 Hodogram representation and helicity

As discussed in Section 2.6.3, the author uses the magnetic hodograms to show the direction of magnetic field lines of magnetic clouds. The magnetic field vectors are plotted at a fixed time in a three-dimensional space, in the minimum variance space in this case. The magnetic field vectors are then connected to form a trajectory.

The magnetic field vectors are gotten from projecting the magnetic field data in RTN coordinates onto the eigenvectors at each time, i.e., the dot product of centred $\vec{B}$ and $\vec{x}_i$. This results in the measured components of B in the minimum variance system, ordered as B_L (B_r^*), B_M (B_t^*), B_N (B_n^*), corresponding to maximum, intermediate and minimum B components respectively for PSP observations or B_x^*, B_y^*, B_z^* for WIND observations. It represents the contribution of each of the eigenvectors to the overall magnetic field variation.

The direction of the hodogram in the intermediate-to-maximum variance plane,

which shows the magnetic field rotation in three-dimensional space over time is also used to identify the helicity of the magnetic flux ropes. A right-handed helicity (RH) would be represented as a counterclockwise rotation in the hodogram and a left-handed helicity (LH) would be represented as a clockwise rotation. The helicity, $H = -1$ when it is left-handed and $H = 1$ for right-handed. This is one of the parameters used in the force-free model fitting (Section 3.14).

3.13.4 Magnetic flux rope configuration

The orientation, longitude (ϕ) and latitude (θ), of the ICMEs, are important parameters because they are often used to determine the rotation of the ICME as it propagates into the heliosphere. Also, the accurate orientation of an ICME is especially important near the Earth because the orientation of ICMEs is related to its geo-effectiveness (ZHAO; HOEKSEMA, 1998).

Magnetic flux ropes have been classified into 8 types by Bothmer and Schwenn (1998) given in Figure 2.12. To determine the type of flux ropes, the author has to calculate the latitudinal components θ and longitudinal components ϕ of the magnetic field vectors of the magnetic cloud. To calculate these, the author performs a coordinate transformation from the RTN (r, t, n, for PSP data) or GSE (x, y, z, for WIND data) coordinate system to the spherical coordinate system (r, θ, ϕ).

$$\theta = 90^\circ - \operatorname{atan}2\left(\frac{\sqrt{B_r^2 + B_t^2}}{B_n}\right) \times \frac{180^\circ}{\pi} \tag{3.5a}$$

$$\phi = \operatorname{atan}2\left(\frac{B_t}{B_r}\right) \times \frac{180^\circ}{\pi} \tag{3.5b}$$

The latitudinal angles must be varying between -90° – 90° and the longitudinal angles must be varying between 0° – 360°.

Using Equations (3.5) with the classification given in Figure 2.13, the plot of PSP observations and WIND observations are classified into one of the 8 types: SEN, SWN, NES, NWS, ENW, ESW, WNE, and WSE.

3.14 Lundquist force-free model processing

The MVA results that quantify the geometry of the flux rope are used as a starting point for the force-free model fit to the magnetic field components and angular variation, using the Lundquist Equation (2.37) (LUNDQUIST, 1950). It generates predicted magnetic field solutions that are used to fit the MCs data measured *in-situ* using a least squares technique similar to Lepping et al. (1990). The orientation angles calculated using MVA initialise the χ^2 minimisation (GOOD et al., 2019; DAVIES et al., 2020).

To do this, it is important to rotate the modelled data by an angle ω around a dimensionless rotation axis. The rotation simulates the simulation performed by MVA to the new coordinate system, i.e., it redirects the axes of the force-free model from angles ϕ and θ. Thus, the force-free model also further verifies the MVA results.

According to Bothmer and Schwenn (1998) and Lepping et al. (2006), the possible geometric configuration for the predicted ideal model corresponds to the projection of the magnetic field lines in the yOz plane, that is, the projection of the axis of the ideal cylinder on the yOz plane of the GSE coordinate system, as shown in Figure 3.15. Thus, we define the angle of rotation ω on the yOz plane from the angles ϕ and θ expressed in Equation (3.6).

Figure 3.15 - The projection of the axis of the ideal cylinder (ϕ, θ) derived from Lundquist model onto the yOz plane of the GSE coordinate system. Angle ω is calculated according to Table 3.1.

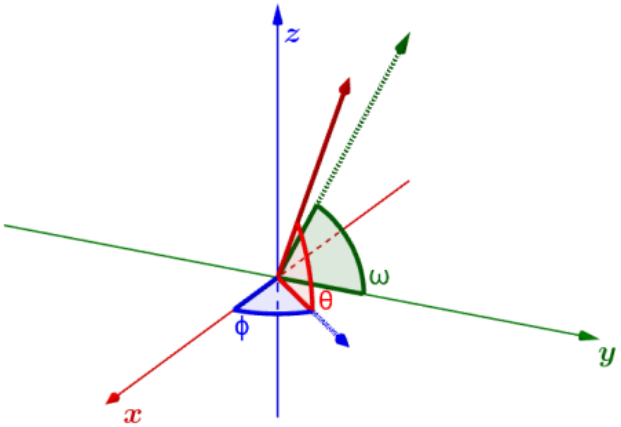

SOURCE: Oliveira et al. (2021).

The relationship between the Cartesian axes and the GSE coordinate system is given by the set of equations (OJEDA-GONZÁLEZ et al., 2017):

$$\begin{cases} x = R\cos\phi\cos\theta \\ y = R\sin\phi\cos\theta \\ z = R\sin\theta \end{cases} \tag{3.6}$$

where ϕ and θ are longitudinal and latitudinal angles respectively and R is the radius of the MC.

In this method, the rotation is performed around the $\hat{x}$-axis in the canonical basis, using this matrix to perform the rotation of the coordinate system.

$$M(\hat{x},\omega) = \begin{bmatrix} 1 & 0 & 0 \\ 0 & \cos\omega & \sin\omega \\ 0 & -\sin\omega & \cos\omega \end{bmatrix} \tag{3.7}$$

The angle ω varies between 0° and 360° and is calculated using the Table 3.1.

Table 3.1 - Relationship between angles ϕ, θ and ω.

$0° < \theta < 90°$	$0° < \phi < 180°$ $180° < \phi < 360°$ $\phi = 0°$ or $\phi = 180°$ or $\phi = 360°$	$\omega = \theta$ $\omega = 180° - \theta$ $\omega = 90°$
$-90° < \theta < 0°$	$0° < \phi < 180°$ $180° < \phi < 360°$ $\phi = 0°$ or $\phi = 180°$ or $\phi = 360°$	$\omega = 360° + \theta$ $\omega = 180° - \theta$ $\omega = 270°$
$\theta = 0°$	$0° < \phi < 180°$ $180° < \phi < 360°$ $\phi = 0°$ or $\phi = 180°$ or $\phi = 360°$	$\omega = 0°$ $\omega = 180°$ $\nexists\ \omega$
$\theta = -90°$	$0° \leqslant \phi \leqslant 360°$	$\omega = 270°$
$\theta = 90°$	$0° \leqslant \phi \leqslant 360°$	$\omega = 90°$

SOURCE: Oliveira et al. (2021).

From Table 3.1, there is no ω for $\phi = 0°$ or $\phi = 180°$ or $\phi = 360°$ because the cloud axis projection corresponds to a point at the origin of the system. Here is the summary of the steps taken to rotate the modelled magnetic field data $\vec{B}^M$:

- Generate the components of the modelled magnetic field data using the force-free Equation (2.37)
- Project the components onto the yOz plane and

- Rotate by ω, which gives $B_x^M,\ B_y^M,\ B_z^M$.

For the optimization process, a non-least-squares fitting technique using `curve_fit()` from the Python open source library `SciPy` (VIRTANEN et al., 2020) is used to fit the modelled B^M data to the observed data B^O. The `curve_fit()` function is part of `scipy.optimize` and a wrapper for `scipy.optimize.leastsq` and internally uses a Levenburg-Marquardt gradient method(also known as damped least-squares method) to minimize the objective function (Lundquist force-free model function in this case).

The zeroth- and first-order Bessel function in the Lundquist force-free model equations are calculated using the `special.jv` function from the Python `scipy` library, where `)` and `J_1 = sp.jv(1, x)`. Also, αR is set to range from -2.4 to 2.4. The optimised parameters are B_0 and α, where B_0 is the maximum magnetic field, i.e., the magnetic field at the axis of the magnetic cloud. Chirality or handedness, H, is a constant -1 or +1 that is also used as input for the force-free equations.

3.14.1 Distance correlation

The optimized Lundquist model is then compared to the observed data to assess how well the model fitting correlates with the observed magnetic field data and calculated longitude and latitude of $\vec{B}$. By using `dcor.distance_correlation(M, O)` in Python, we generate the distance correlation between the two variables.

Distance correlation is used to measure both linear and non-linear associations or dependence between two variables. This is different from Pearson correlation r which only applies to a linear relationship between variables. The distance correlation between any two variables is between zero and one. Zero means that the variables are independent and values closer to one indicate that they are dependent. The distance correlation between the modelled data (M) and observed data (O) would be:

$$\mathcal{R}(M,O) = \frac{\mathcal{V}(M,O)}{\sqrt{\mathcal{V}(M)\mathcal{V}(O)}} \tag{3.8}$$

As mentioned earlier in Section 2.5.2, the modelled magnetic field is symmetric, which does not agree well with observed B data due to erosion and other plasma processes. Since the force-free is generally suitable for reproducing the direction of the magnetic field components, we will only apply the distance correlation to the

fitting of the longitudinal and latitudinal variation of $\vec{B}$.

3.15 Other magnetic cloud parameters

3.15.1 Radius and expansion of the magnetic cloud

The radius of the magnetic cloud is estimated using:

$$R = \frac{V_{avg}}{t} \tag{3.9}$$

where V_{avg} is the average velocity within the magnetic cloud and t is time, $t = t_2 - t_1$, where t_2 and t_1 are the time at the beginning and end of the magnetic cloud boundaries.

In a previous study (BOTHMER; SCHWENN, 1998), it was deduced from a combined study of Helios, voyager and IMP data that the radial diameter of the magnetic cloud increases between 0.3 and 4.2 AU, proportionally to $R^{0.8}$, where R is given in AU. (BURLAGA; BEHANNON, 1982) estimates that

$$V_f - V_r \approx 2V_{exp} \tag{3.10}$$

where V_f and V_r are the speed at the front and rear boundary of the MC respectively. They are calculated by performing a linear fit on the temporal profile of velocity within the MC as shown in Figure 3.16. V_{exp} is the expansion velocity. However, the density decreases inside the magnetic cloud proportional to $R^{-2.4}$, which is stronger when compared to the average solar wind. In the MC analyses of multi-spacecraft observations, the author will verify these proportionalities.

Figure 3.16 - Example of MC velocity and its linear fit.

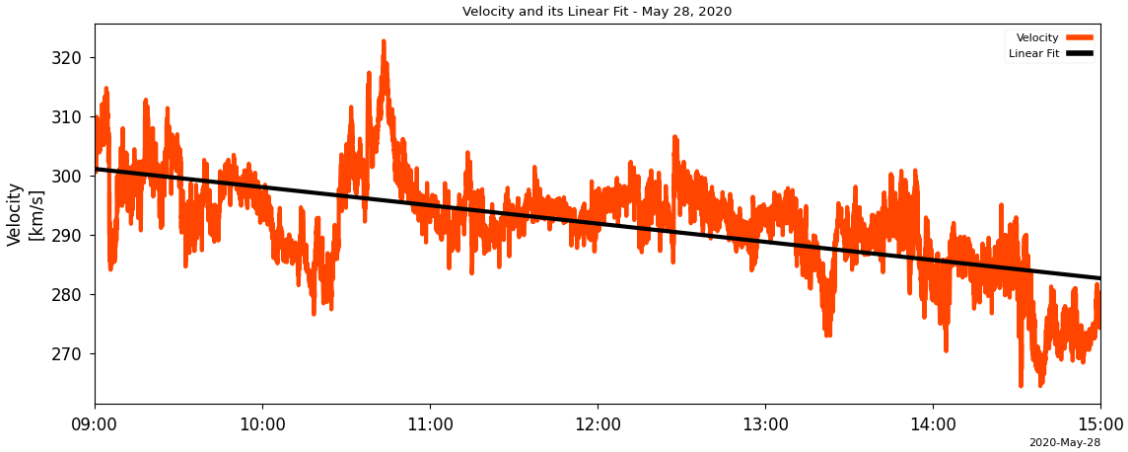

SOURCE: Author.

3.15.2 Location angle

The location angle, L, defined by Janvier et al. (2013) is used as a proxy for the crossing distance of the spacecraft from the nose of the flux rope. It is estimated using:

$$\sin L = \cos\theta_{axis} \cos\phi_{axis} \tag{3.11}$$

The location angle ranges from $L \approx 0°$ to $L \approx -90°$ in one leg, and through $L \approx 0°$ at the nose, to $L \approx 90°$ in the other leg. The closer L is to zero, the closer the spacecraft crossed close to the nose.

4 OBSERVATIONS AND RESULTS

This chapter is divided into five parts with Part 1 discussing the identified ICMEs and MCs from the observation of Parker Solar Probe from 2018 – 2022. Parts 2 and 3 present four (4) samples of single spacecraft and multiple spacecraft observations in the interplanetary medium and Part 4 presents an event that has been analysed in a previous research but a contradictory result was realised. Part 5 presents a summary analysis and deductions from all the events analysed.

4.1 PART I: identification of ICMEs and MCs occurrences: 2018-2022

Using the requirements listed in section 2.1, a total of 54 ICMEs were identified from Parker Solar Probe observations from 2018–2022. Some of these events were observed by PSP only, while some were also observed by other spacecraft such as WIND spacecraft. A summary of the identified ICME events is shown in Table 4.1.

Table 4.1 - The dates of the 54 visually identified ICMEs observed by PSP from November 2018 – September 2022 in combination with an already existing Helio4cast catalogue.

Year	Number of Events	Dates of observation
2018	2	Nov 11, Oct 30
2019	8	March 15, March 24, July 25, July 31, Sep 10, Oct 13, Dec 1, Dec 2
2020	16	Feb 11, Apr 6, Apr 10, Apr 21, May 28, June 23, June 25, June 27, July 22, Aug 18, Sep 12, Oct 13, Oct 28, Nov 29, Dec 1, Dec 15
2021	20	Feb 11, Feb 12, May 5, May 28, May 30, June 7, June 8, June 12, June 25, June 30, July 11, July 24, Aug 29, Sep 12, Sep 26, Oct 11, Oct 27, Nov 3, Nov 9, Dec 28
2022	8	Jan 29, Feb 16, June 12, July 5, July 7, July 17, July 19, Sept 26

SOURCE: Author.

4.1.1 Magnetic cloud occurrences

This research is solely focused on analyses of magnetic clouds; but not all the ICMEs contain a coherent rotation in the direction of the magnetic field component, which represents the presence of a magnetic cloud. So out of the 54 visually identified ICMEs, 44 contain magnetic clouds. Table 4.2 contains the date of occurrence of these magnetic clouds.

Table 4.2 - A summary of the 44 visually identified ICMEs that has magnetic cloud (MCs).

Year	Number of Events	Dates of observation
2018	2	Nov 11, Oct 30
2019	6	March 15, July 25, July 31, Oct 13, Dec 1, Dec 2
2020	13	Feb 11, Apr 6, Apr 21, May 28, June 23, June 25, June 27, July 22, Aug 18, Sep 12, Oct 28, Nov 29, Dec 1
2021	16	Feb 11, Feb 12, May 5, May 28, May 30, June 12, June 24, June 30, July 11, Aug 29, Sep 12, Sep 26, Oct 11, Nov 3, Nov 9, Dec 28
2022	7	Jan 29, Feb 16, July 5, July 7, July 17, July 19, Sept 26

SOURCE: Author.

However, some of these events have a lot of data gaps in their magnetic field data or plasma measurements, with which we cannot perform complete analyses. With these conditions, 17 ICMEs containing magnetic clouds (MCs) and well-observed magnetic field and plasma measurements were selected for this research.

4.1.2 MCs observed by PSP and are Earth-bound

One of the major objectives of this research is to analyse ICME events that were observed by multiple spacecrafts, especially by PSP and WIND, which are Earth-bound. So we manually identified MCs in WIND observations and also utilised existing catalogues of WIND observations of ICMEs given in Section 3.10.

The WSA-ENLIL+cone model simulations (described in Section 3.10) help to identify events that are observed by PSP, WIND, other spacecrafts and interacted with Earth. It gives a simulation of the density and velocity of the CMEs. Apart from simulations, it also gives predicted magnetic field and ion density values at different spacecrafts and planets such as PSP, STEREO-A and Mars.

This section presents the well-observed ICME events that contain magnetic clouds, that are observed by the Parker Solar Probe only and additional spacecraft. The summary of the 17 selected measurements (grouped into 11 single and multi-spacecraft events) and their boundaries are shown in Table 4.3.

Table 4.3 - Single and multi-spacecraft ICMEs observation by PSP, WIND, and STEREO-A, SOHO/LASCO that were analysed in this research.

#	**Start Date/ Time (UT)**	**CME lat.(°)**	**CME long.(°)**	**Location**	**Source**	**S/C– Instrument**	**R(AU)**	**S/C long.(°)**
1	24-05-2020 08:24	-3	-155	SE of EUVI 195	AR	STA-COR2	0.97	-72.5
	28-05-2020 01:20					PSP	0.35	147.6
2	21-06-2020 04:12	-2	41	N40W40	filament	SOHO-C2	1.01	0.2
	23-06-2020 03:20					PSP	0.48	17.7
	26-06-2020 11:00					WIND	1.01	-0.3
3	22-06-2020 15:09	-8	19	S20W08	—	STA-COR2	0.96	-69.7
	25-06-2020 11:30					PSP	0.52	19.9
	27-06-2020 03:10					WIND	1.01	-0.3
4	24-06-2020 05:12	1	43	N09W60	—	SOHO-C2	1.01	0.2
	27-06-2020 12:00					PSP	0.55	20.8
	30-06-2020 01:12					WIND	1.01	-0.3
5	12-09-2020 08:00	—	—	—	—	PSP	0.47	13.0
6	29-11-2020 13:24	-6	-75	S23E97	M4.4 flare	STA-COR2	0.96	-57.7
	30-11-2020 18:40					PSP	0.80	-96.4
	02-12-2020 07:30					WIND	1.00	0.07
7	23-08-2021 03:09	11	-1	NW of STA-COR2	—	STA-COR2	0.96	-42.6
	25-08-2021 04:00					PSP	0.51	-37.5
	27-08-2021 00:00					WIND	1.00	0.2
8	23-09-2021 05:48	-14	-32	S22E28	AR12871	SOHO-C2	0.99	-0.1
	26-09-2021 22:50					PSP	0.78	-43.1
	26-39-2021 22:00					STA-COR2	0.96	-39.8
	27-09-2021 15:40					WIND	0.99	0.2
9	23-09-2021 16:53	-21	-16	S28W16	AR12871	SOHO-C2	0.99	-0.1
	26-09-2021 09:00					PSP	0.78	-43.1
	27-09-2021 14:55					STA-COR2	0.96	-39.8
	26-09-2021 23:00					WIND	0.99	0.2
10	07-11-2021 15:05	11	-80	N20E70	AR12895	SOHO-C2	1.00	-0.3
	09-11-2021 16:50					PSP	0.44	-51.6
11	03-07-2022 03:09	6.0	-2.0	West of STA-COR2	filament	STA-COR2	0.96	-25.5
	04-07-2022 20:50					PSP	0.70	34.3
	07-07-2022 08:00					WIND	1.01	-0.1

Note: **Start time (DD-MM-YYYY)** signifies the time of observation of the CMEs at the coronagraphs and ICMEs shock arrival time at the respective *in situ* spacecrafts. **Source** is the active region (AR) number or source conditions associated with the eruption. **C2** is a coronagraph that is part of the LASCO instrument aboard SOHO. **COR2** is a coronagraph that is part of the SECCHI instrument aboard STEREO-A/STA.

SOURCE: Author.

ICME front boundaries (start times) are selected in this research using a vivid gradual/sudden enhancement in the magnitude of the magnetic field in concert with gradual/sudden changes in the plasma parameters. The rear boundaries (end times) are chosen to be where the magnetic field reduces approximately back to its original value, and changes are also observed in the plasma parameters.

On the other hand, the front boundaries (start times) of MCs are placed where (approximately) the lowest value of B_z/B_y (GSE) or B_n/B_t (RTN) is observed just before the start of the rotation with clear changes in the plasma parameters. The rear boundaries (end times) are placed approximately where the maximum value is reached at the end of the rotation and also in concert with changes in the plasma parameters. These changes may be gradual or abrupt.

4.2 PART II: single spacecraft events

In this section, we explored Event 10 in Table 4.3 that was observed by a single spacecraft in-situ, which is Parker Solar Probe. Event 7 will also be discussed as an example of a single-point observation of ICMEs. Although it was observed by both PSP and WIND, we only focus on the WIND observation because of the insufficient data points present in the PSP observation. The WIND observation has a clear and pristine flux rope structure. We will use the magnetic field and solar wind measuring instruments aboard these Solar and Heliospheric missions to study the averaged data of these events, trace them to the Sun, present their remote analysis and model their propagation in situ.

4.2.1 Example 1: November 10, 2021, ICME

4.2.1.1 Overview of the eruption

One of the single spacecraft events that we analyzed in this work was initiated on the **7th of November, 2021** at about **15:05 UT**. The eruption was captured, in its initial stage by the EUVI (Extreme Ultraviolet Investigation) telescope, which is part of the Sun-Earth Connection Coronal and Heliospheric Investigation (SECCHI) suite on board the STEREO-A spacecraft. The spacecraft is located at ≈ 0.96 AU which is 37° east of the Sun-Earth line and latitude 3° north of the Sun-Earth line. It was also observed by C2 and C3 telescopes of the Large Angle and Spectrometric Coronagraph (LASCO) on board the Solar and Heliospheric Observatory (SOHO) located near Earth at 1 AU. The event was also visible, albeit fainter, at COR2 of the STEREO-A spacecraft.

Figure 4.1 shows the remote observation of the CME just before the eruption and a few minutes after the eruption as observed by AIA 171 and EUVI 195 Å respectively. The Atmospheric Imaging Assembly (AIA, Lemen et al. (2012)) is aboard the Solar Dynamic Observatory (SDO, Pesnell et al. (2012)) orbiting the Earth. Rising field lines were visible at AIA 171/195 starting from 7th November 2021 at 12:25 UT

with the region of eruption bounded by a square in Figure 4.1a. Dimming and post-eruptive arcades were then observed at EUVI-A shown in Figure 4.1b.

Figure 4.1 - Remote observations of the CME eruption that occurred on 10 November 2021.

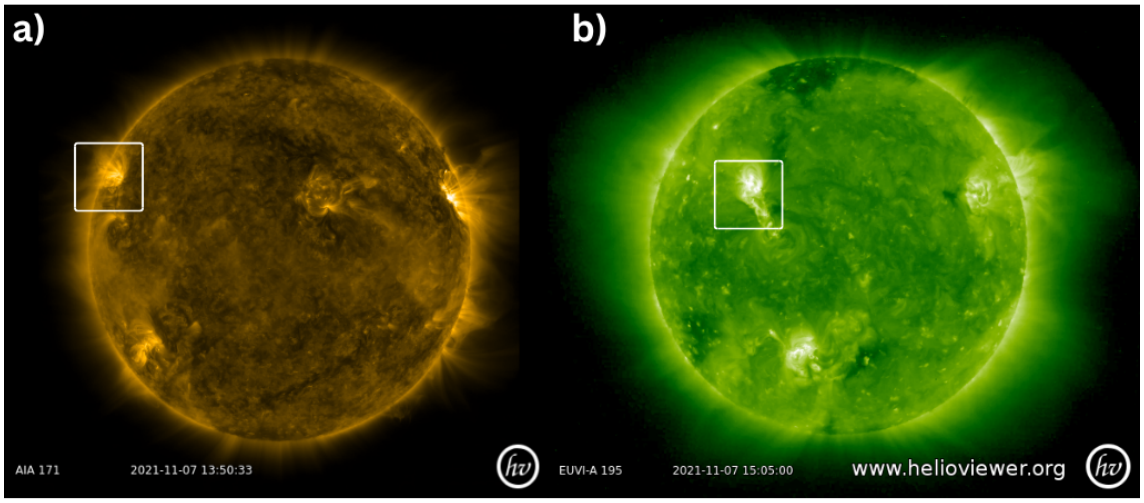

(a) SDO/AIA 171 Å image taken around the time of eruption with the box bounding the approximate source region. (b) STEREO-A/EUVI 195 Å image taken when the CME is at the edge of the corona, visible with a curved loop.

SOURCE: Helioviewer website, Hughitt et al. (2008).

Figure 4.2 - Remote observations.

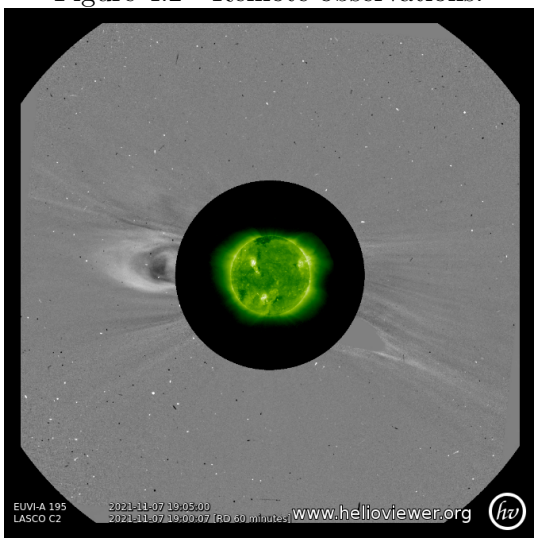

SOHO/LASCO-C2 image (running difference of 60 min) showing the CME in white light with STEREO-A/EUVI 195 Åimage at the center.

SOURCE: Helioviewer website, Hughitt et al. (2008).

Figure 4.2 shows the observation of SOHO/LASCO-C2 and STEREO-A/EUVI 195 Åabout four hours after the eruption. The CME later became visible in STEREO/-COR2 and overlaps with another CME that erupted at 16:12 UT, thus marring the later formation of this CME.

The sources of the CME appear to be from an active region of number 12895 at the northeast of EUVI 195, located in N20E70. Dimming on the active region was observed around 13:25 UT on 7 November 2021. The longitude of the erupting CME is derived to be -80° (HEEQ) and latitude 11°. The velocity of the CME is estimated to be about 397 km/s, which is considered to be an average-speed CME and the half angular width of 26°. By applying these model inputs to the Wang-Sheeley-Arge (WSA)-ENLIL+Cone model, the output of the simulated CME is shown in Figure 4.3. It is a scaled density contour plot for the (a) constant Earth latitude plane, (b) meridional Earth plane and (c) 1 AU sphere in cylindrical projection on 10 November 2021 at 12:00 UT. It indicated no impact on Earth.

Figure 4.3 - Global view of the 10 November 2021 CME at 12:00 UT.

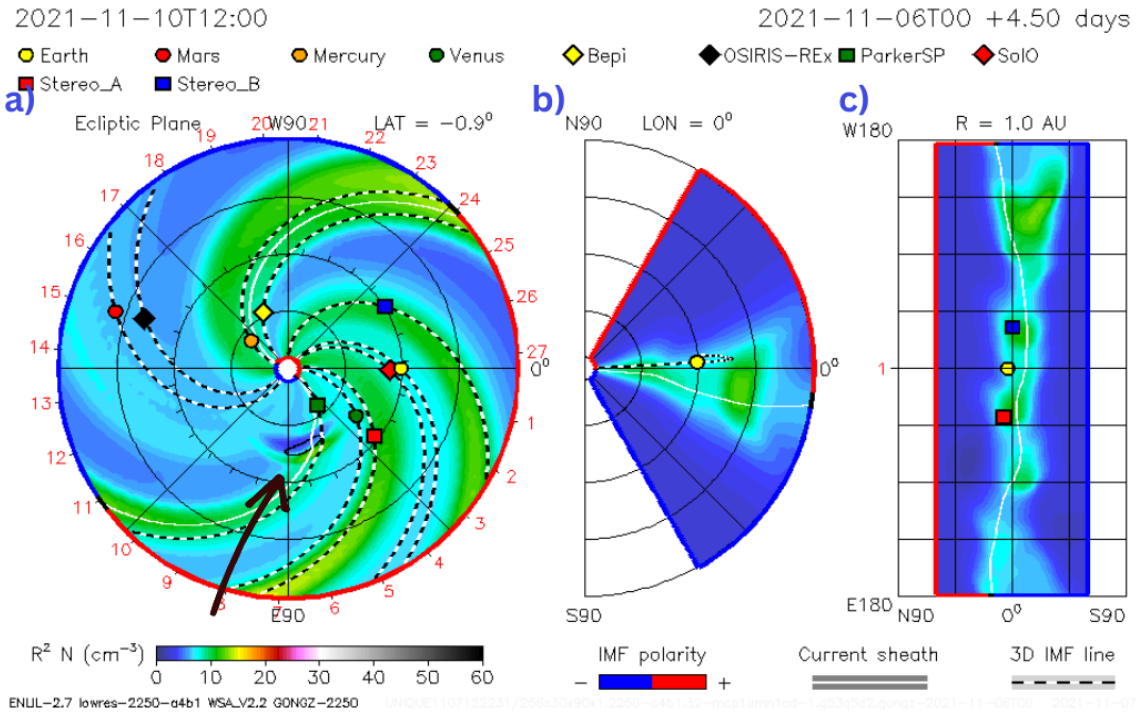

WSA-ENLIL+Cone model of the CME: (a) in the solar equatorial plane, the arrow points to the propagating eruption, (b) in the meridional plane at the Earth longitude, (c) 1 AU sphere in a cylindrical projection with CME input parameters (speed of 397 km/s, direction of -80° longitude, 11° latitude and half-width of 15°) PSP is the green square.

SOURCE: CCMC DONKI, Pizzo (2011).

4.2.1.2 In situ observation of the CME

Parker Solar Probe (PSP) encountered the CME in the interplanetary medium on 9 November 2021 at 16:50 UT. PSP was located at 0.48 AU, 52.8° east of the Sun-Earth line and 0.1° latitude. The magnetic field data in Figure 4.4 were measured by the FIELDS instrument and plasma data by the SWEAP instrument aboard PSP. The WSA-ENLIL+cone model showed that PSP (shown in the green square) observed the glancing bow of the ICME as shown in Figure 4.3.

The ICME was preceded by a shock which was characterised by enhancement in the magnetic field data $\vec{B}$, velocity V, and temperature T which is marked by the dotted vertical violet line. After the ICME shock is the magnetic cloud (MC) region enclosed in blue. The observed MC met the necessary requirements which are: (i) the rotation of the magnetic component (B_n, (Fig 4.4b)), representing a flux rope structure, (ii) depressed density (signifying expansion) and temperature (4.4c & e), (iii) low plasma beta (4.4f) which signifies dominating magnetic pressure within the flux rope structure, and (iv) decreasing velocity component (4.4d), which exhibits expansion of the magnetic cloud as the observing spacecraft passes by. The boundaries were chosen to be points where there are abrupt changes in the observed and derived parameters (ZURBUCHEN; RICHARDSON, 2006).

4.2.1.3 Flux rope-type identification in situ

The flux rope type is first identified by visual observation of the (B_r, B_t, B_n) components of the magnetic field and the angular and the angular variation of the B_{lat} and B_{long} in RTN coordinates. The latitudinal component of the magnetic field (Figure 4.4 g) is seen varying from negative to positive, i.e., southward to northward and the longitudinal component (Figure 4.4 h) is between 180° and 360° which represents westward direction. This signifies a flux rope type **SWN**; this denotes that the chirality is **RH**.

Secondly, we apply minimum variance analysis (MVA), which generates $\theta_{axis} = 13.3°$ and $\phi_{axis} = 81.2°$ that represents the calculated orientation of the FR axis. This is in the intermediate variance direction. The minimum variance direction is: $\theta_{min} = 16.3°$ and $\phi_{min} = 347.2°$. The $\theta_{axis} < 45°$ signifies a bipolar FR and agrees with the orientation deduced from visual inspection.

To estimate the chirality/handedness, we construct the magnetic hodogram of the ICME to estimate the direction of rotation of B_{mva} by visual inspection. The mag-

Figure 4.4 - ICME event encountered by Parker Solar Probe on 10 November 2021.

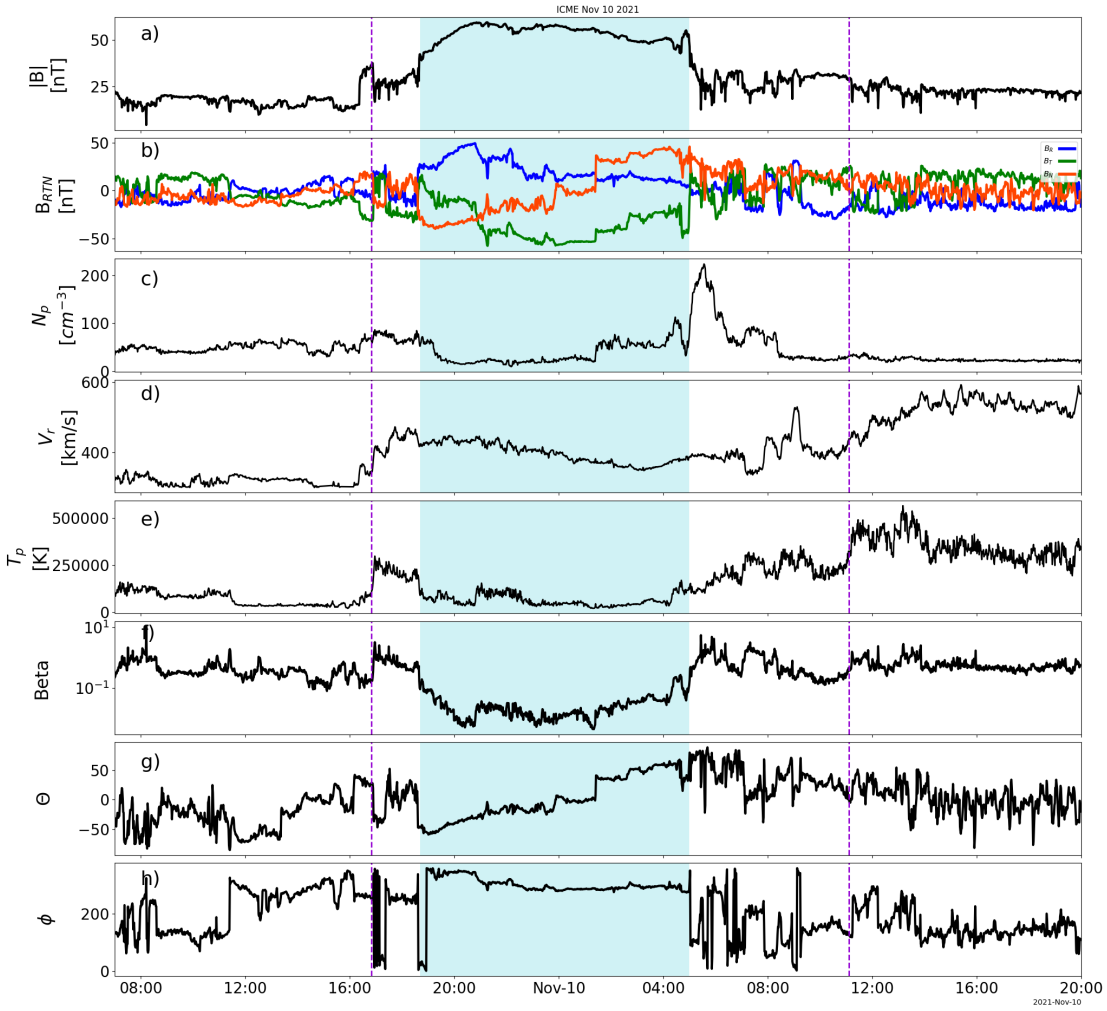

From the top, (a) is the magnitude of the magnetic field $|B|$, (b) magnetic field components B_{RTN}, (c) proton density N_p, (d) solar wind speed R component V_r, (e) proton temperature T_p, (f) plasma beta β, (g) latitude component (polar angle) of $\vec{B}$, B_{Lat} and (h) longitude component (azimuthal angle) of $\vec{B}$, B_{Long}. The red dotted lines enclose the ICME, while the blue region encloses the MC.

SOURCE: Author.

netic hodogram of the maximum and minimum variance plane is shown in Figure 4.5. The closed circle denoted the endpoint of the hodogram plot and the arrow indicates the direction of the rotation of the magnetic field. Figure 4.5a shows a clockwise rotation with -B_t^* values in the maximum variance.

Magnetic hodograms are also used to confirm the smooth rotation of the mag-

netic field components. Using the morphological classification created by Nieves-Chinchilla et al. (2018), Nieves-Chinchilla et al. (2019), the flux rope belongs to category Fr, because it has a single rotation that is between 90° and 180°.

Figure 4.5 - Magnetic Hodograms of the ICME.

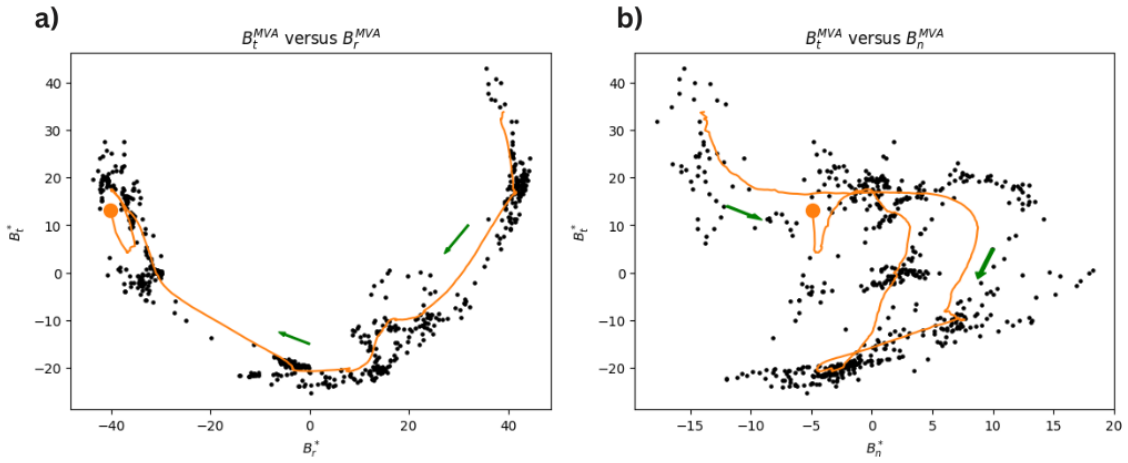

(a) maximum variance plane (B_t^* vs B_r^*) and (b) minimum variance plane (B_t^* vs B_n^*) in the MVA coordinate system represented by the asterisk (*) sign.

SOURCE: Author.

The reliability of the MVA results are then validated using the error criteria given by Lepping and Behannon (1980): $\lambda_2/\lambda_3 = 6.7$; Siscoe and Suey (1972): $\lambda_1/\lambda_2 = 3.2$ and $\lambda_3/\lambda_2 = 0.15$; and Oliveira et al. (2020): $P = 11.86$. The variance was well determined according to these error criteria. χ, the angle of rotation, which is the angle between the first and last value of the field vector was 136°.

The impact parameter p which is calculated along the direction of minimum variance (B_n^*) is 0.15, signifying that PSP did not cross far from the flux rope central axis.

The location angle L is 40° signifying that the spacecraft did not cross close to the nose of the flux rope (Section 3.15.2).

4.2.1.4 Force-free model reconstruction

Here, we performed a linear force-free fit to the magnetic field components based on the force-free constant-α model discussed in Section 2.5.2. The MVA orientation, $\theta_{axis} = 13.3°$ and $\phi_{axis} = 81.2°$ were used to initialise the χ^2 minimisation. As described in Section 3.14, the force-free magnetic field components were generated

from Equation 2.37, with $B_0 = 59.6$ nT, $\alpha = 2.4$ (constant), $H = +1$ (because the orientation is right-handed). Since MVA only gives the axis of the flux rope which is represented by the intermediate eigenvector, the force-free model helps to refine the direction of the axis of the FR.

Figure 4.6 - Force-free fitting for Nov 10, 2021, MC.

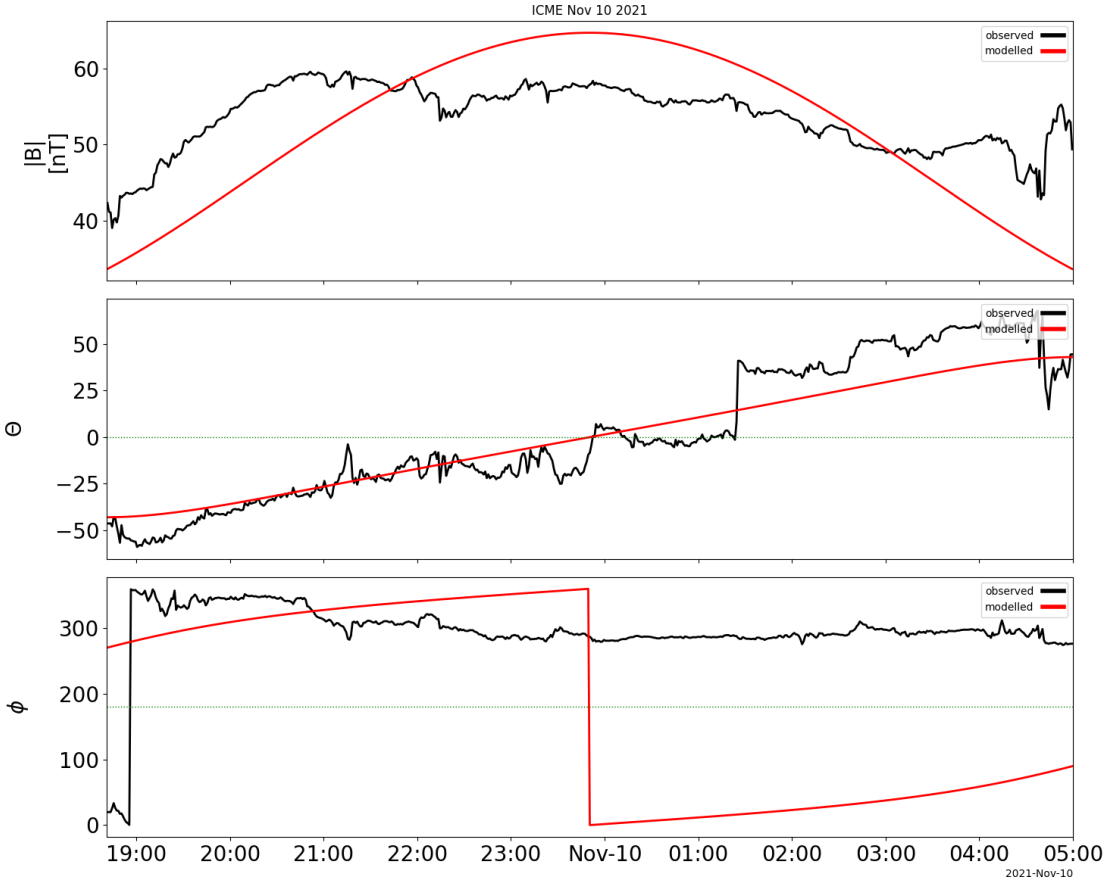

SOURCE: Author.

The fitting result is shown in Figure 4.6. It is known that the force-free model assumes a symmetric shape as seen in the plot as seen in the first panel. This is because the Lundquist solution predicts the amplitude of the magnetic field to be at the axis of the flux rope. However, in practical cases, magnetic field data are usually asymmetric because of expansion and magnetic flux rope erosion (FARRUGIA et al., 1993; PAL et al., 2020).

The latitudinal variation was well fitted and longitudinal variation is not suitably fitted because the longitudinal variation drops to 0° after it reaches 360°. However, it is important to note that 360° and 0° are algebraically equal, but when visualized on the graph, they appear to be at extremes which can result in incorrect classification.

The distance correlation (discussed in Section 3.14.1), between the force-free fit and estimated latitudinal data, is 0.95. The proximity of the value to 1 signifies a good fitting. For the longitudinal variation, the distance correlation is 0.67. This shows a "fair" fitting.

4.2.2 Example 2: August 26, 2021 ICME

Figure 4.7 shows the ecliptic plane map and the locations of multiple spacecraft on 26 August 2021, during which WIND spacecraft detected the transit of the ICME. PSP, in violet, was located at ≈37° east of the CME apex, ≈38° east of L1, and at a heliospheric distance of 0.51 AU from the Sun. The apex of the CME was pointing directly at L1. This configuration allows the observation of ICME at its apex and flank within a close period. However, there was a data gap in PSP observation due to the several manoeuvres it performed during this period. Due to the clear and smooth rotation of the B_n component of this event close to Earth, this section is focused on the analysis of the magnetic structure of the ICME as observed by WIND only.

Figure 4.7 - Map of the location of WIND (black), PSP (violet), and STEREO-A (red) and spacecraft at L1 (black, WIND and ACE) on August 26, 2021. The black arrows represent the central direction of propagation of the CME.

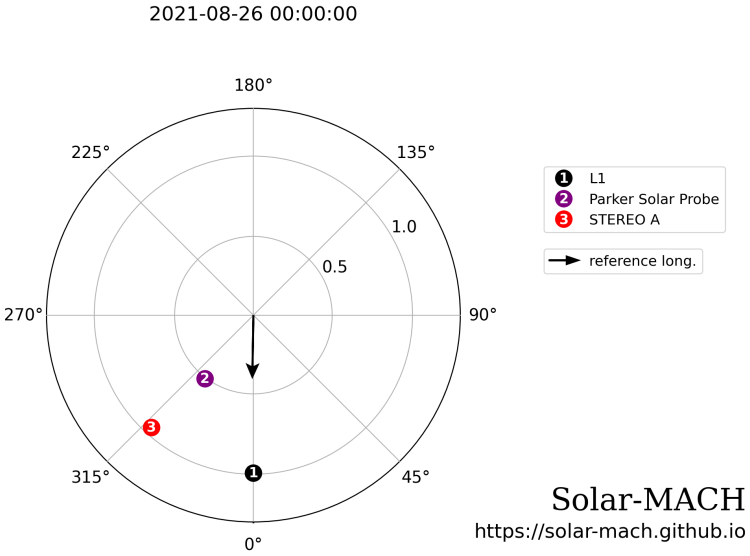

SOURCE: Solar MACH tool, Gieseler et al. (2022).

4.2.2.1 In situ observation and analysis

Figure 4.8 shows the measurement of the magnetic field data by WIND magnetic field instrument. The plot shows the magnitude of the magnetic field, the components in GSE coordinates and the components in spherical coordinates (θ and ϕ). There is a clear shock, marked in violet dotted lines, starting from **00:00 UT on 27 August 2021** and accompanied by a turbulent sheath. During the ≈12 hours turbulent sheath, there were rapid fluctuations in the direction of the magnetic field, which signifies a magnetic sheath, until the magnetic cloud is observed (enclosed in blue). The MC is characterised by a coherent rotation in the magnetic field for ≈22 hours. Compared to observations made in PSP in previous analyses, this is a long observation. However, it agrees with previous research, such as Burlaga et al. (1981), which states that the passage of an MC close to Earth is for about one day. The rotation of the magnetic field components within the magnetic cloud is large, ≈129° which indicated the presence of rotating magnetic flux ropes. and with a maximum of $B_{max} = 16$ nT and an average of $\langle B \rangle = 12.9$ nT, which is twice the magnetic field strength of the solar wind prior to the shock commencement.

Using panels c and d of Figure 4.8 and application of MVA shows that the orientation of the magnetic cloud is **SEN**. That means this is a left-handed low-inclination bipolar flux rope embedded in the magnetic cloud. Application of the MVA allows us to construct the magnetic hodograms where the chirality of the magnetic flux rope can also be confirmed shown in Figure 4.9 MVA application also yields the orientation of the flux rope axis to be, $\phi_{axis} = 264°$ and $\theta_{axis} = 26°$ and satisfies all the error criteria. The impact parameter $p = 0.09$ shows that the spacecraft passes very close to the axis of the flux rope. The location angle, $L = 19°$ shows that the spacecraft was not so far from the nose of the magnetic cloud.

Figure 4.8 - ICMEs encountered by WIND on 27 August 2021.

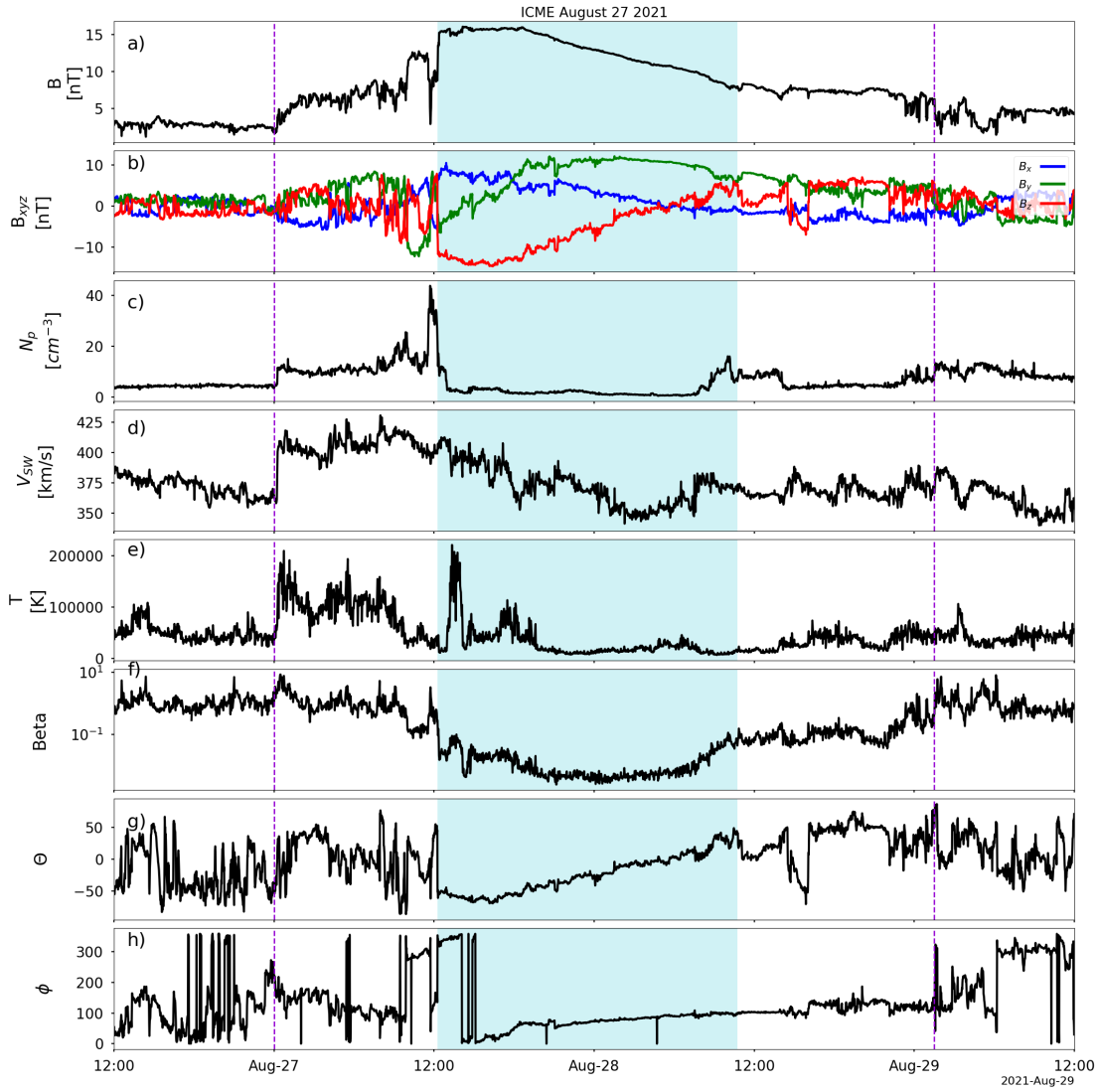

ICME is enclosed in dark violet lines. MC is coloured blue. (a) is the magnitude of the magnetic field $|B|$, (b) magnetic field components B_{xyz}, (c) latitude component (polar angle) of $\vec{B}$, B_{Lat} and (d) longitude component (azimuthal angle) of $\vec{B}$, B_{Long}.

SOURCE: Author.

Figure 4.9 - Magnetic hodogram of August 27 MC observed at WIND spacecraft.

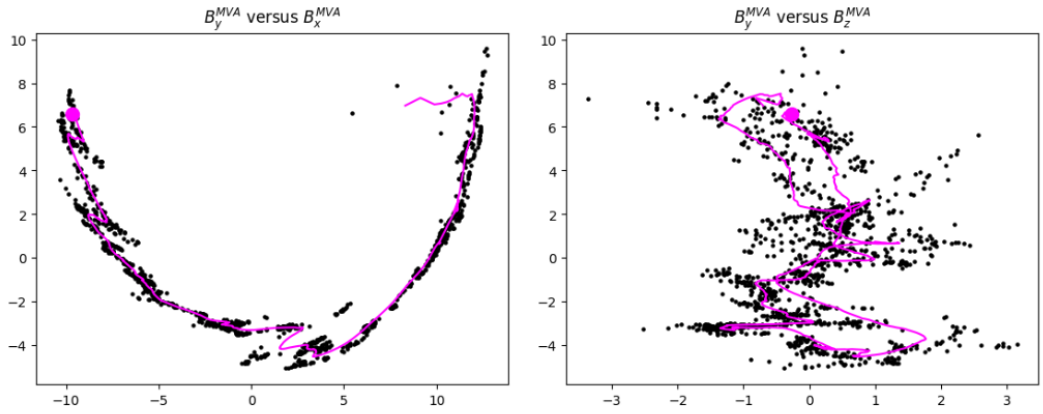

Left: maximum variance plane. Right: minimum variance plane.
SOURCE: Author.

4.2.2.2 Solar and heliospheric observation between August 23–27

To understand the origin of the ICME, the solar surface and its environment were observed through STEREO-A/SECCHI instruments e.g. EUVI and COR2 and SOHO/LASCO instruments. Given the location of PSP, STEREO and L1 spacecraft, with careful processing and use of the CDAW SOHO observation catalogue and WSA-ENLIL catalogue, we identified the source to be an **partial halo CME** that is partially directed towards Earth and seen as an arc around thedi. We deduced that this CME erupted from the region between two active regions AR12859 and AR12861. Figure 4.10 shows the source of the eruption and evolution of the CME. Panel a, b and c contain STEREO-A, and SDO observation at the point of eruption and afterwards. EUVI camera observes the coronal up to ≈1.7 R_S and channel 171 Å is used. STEREO/SECCHI/COR2 outer coronagraph observes the corona between ≈2.5 and 15 R_S at ≈60 minute cadence and it first captured the CME at **03:09 on 23 August 2021**. The CME is visible here, a partial halo, and it is northwest of COR2A. The LASCO/C2 observation of the CME evolution in panel d has a FOV that spans from 2.2. to 6.0 R_S with a cadence of ≈ 12 minutes during the period of observation. The source of the CME is a filament eruption in the north of the solar disk centre in SDO/AIA 193 (panel b) observed at 02:00 UT. The source region in the north-central part of the disk does not allow the study of the evolution of the region.

Figure 4.10 - Evolution of a partial halo CME, August 23, 2021.

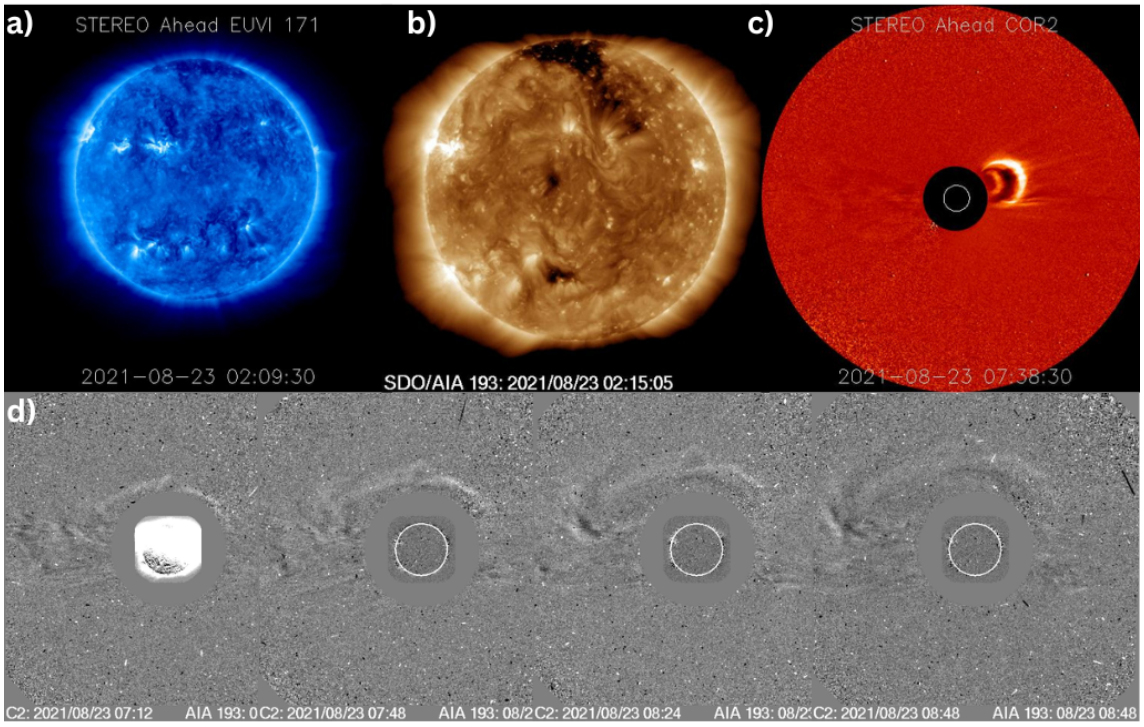

(a) STEREO-A/EUVI 171 image of the Sun at the point of eruption at about 02:00 UT, (b) SDO/AIA image just after the eruption, (c) the CME as it travels outwards from the Northwest region of STEREO-A/COR2 observation of the solar disk, (d) the evolution of the CME in white light captured by SOHO/LASCO-C2 with a running difference.

SOURCE: Adapted from CDAW website, Gopalswamy et al. (2009).

4.2.2.3 Analysis and reconstruction of the ICME

The second method to determine the flux rope orientation and fit the flux rope is using the force-free model with least squares minimization. The initial guesses of the parameters in the magnetic cloud reference frame are: helicity (H = -1, because it is left-handed), constant alpha ($\alpha = 2.4$) and magnetic field amplitude $B_0 = 16$ nT. Then, the least square fitting method is applied and a first series of iterations is to determine the best fitting for the magnetic field magnitude, latitude and longitudinal variation which is shown in Figure 4.11.

It is important to note that the magnetic field profile of the MC is completely skewed to the left. This could be a result of the expansion of the MC (FARRUGIA et al., 1993), or the erosion of the magnetic field (PAL et al., 2020).

Figure 4.11 - Force free fitting of August 27 MC observed by WIND.

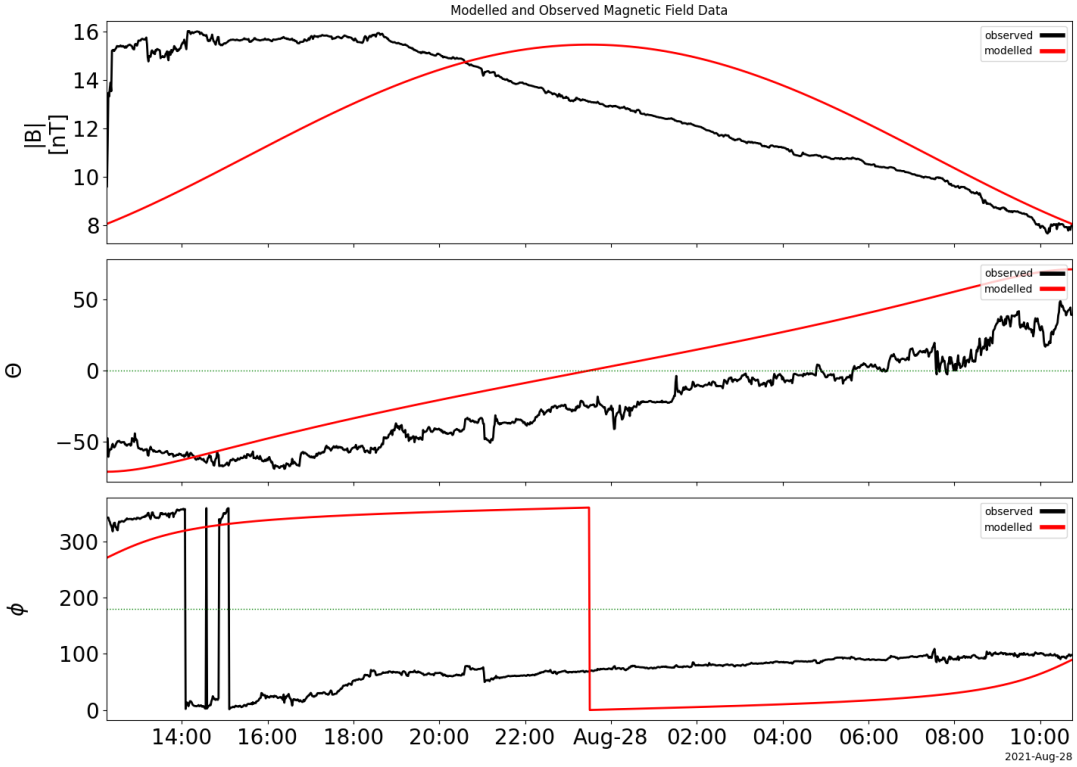

From the top: magnetic field magnitude, latitude and longitudinal variation of the magnetic field.

SOURCE: Author.

The distance correlation, between the Lundquist force-free fitting and the estimated latitudinal data, is 0.98, which signifies a great fitting. For the longitudinal variation, the distance correlation is 0.64. This shows a fair fitting.

4.2.2.4 Geomagnetic effect

The world data centre for geomagnetism based in Kyoto[1] presented provisional hourly equatorial Dst_{min} values. It dropped below -50 nT (signifying a magnetic storm) from 19:00 UT on 27 August 2021 and had the minimum value of **-82 nT** at **00:00 UT on 28 August 2021**. The magnetic storm ($Dst < -50$) persisted until 06:00 UT on 28 August, a total length of 11 hours. Deferring to panel b of Figure 4.8, the southward orientation of the B_z component persisted for a couple of

[1] WDC for Geomagnetism, Kyoto, Hourly Equatorial Dst Values (Provisional) Aug 2021

hours, which is indicative of geoeffectiveness, until it eventually changes to north. Considering WIND observation of B, the intensity of ≈15 nT is of moderate intensity. The world data centre for geomagnetism based in Kyoto[2] presented provisional hourly equatorial Dst_{min} values. It dropped below -50 nT (signifying a magnetic storm) from 19:00 UT on 27 August 2021 and had the minimum value of **-82 nT** at **00:00 UT on 28 August 2021**. The magnetic storm ($Dst < -50$ nT) persisted until 06:00 UT on 28 August, a total length of 11 hours. Deferring to panel b of Figure 4.8, the southward orientation of the B_z component persisted for a couple of hours, which is indicative of geoeffectiveness, until it eventually changes to north. Considering WIND observation of B, the intensity of ≈15 nT is of moderate intensity.

4.3 PART III: multi-spacecraft events: PSP + four other spacecraft

Event No 8 in Table 4.3 is discussed in this Section as a good example for studying the evolution of ICMEs because it was observed by over four spacecrafts in situ. However, it is a 2-in-1 ICME which increases its complexity, yet provides a good opportunity to study interacting flux rope structures in situ. In this section, we will also present Event 11 in Table 4.3 that was observed in situ by PSP and WIND, however, the flux rope configuration at this point differs greatly. Hence, it is a good event to study the effect of longitudinal and radial separation on the evolution of ICMEs.

4.3.1 Example 1: September 26, 2021 ICMEs

4.3.1.1 PSP observation

Figure 4.12 shows the two ICMEs measurements collected by PSP spacecraft. The multi-panel plot shows, from the top, magnetic field magnitude, its components, proton density, solar wind velocity, proton temperature, plasma beta, and latitudinal and longitudinal variation of the magnetic field in spherical coordinates. At the point of observation, PSP is located at 0.78 AU, 42.7° east of the Sun-Earth line and 7° south of the ecliptic plane.

On **September 26, 2021, at 09:00 UT**, PSP experiences abrupt changes across its magnetic field and plasma parameters, which will be referred to as **ICME1**. The magnetic field data initially increased from $B_{max} < 5$ nT to ≈10 nT and further increased to ≈15 nT. The magnetic field magnitude peaked and began to trail off

[2]WDC for Geomagnetism, Kyoto, Hourly Equatorial Dst Values (Provisional) Aug 2021

until ≈14 hours later when another ICME was observed. ICME1 is bounded in red dotted lines in Figure 4.12.

At **22:50 UT**, on the same day, September 26, another sudden enhancement is observed which was also accompanied by abrupt changes in the plasma parameters and will be called **ICME2**. The second ICME persisted for ≈19 hours, with a fairly constant magnetic field magnitude, until an abrupt end time is observed at 18:00 UT on September 27, 2021. ICME2 is bounded in violet dotted lines in Figure 4.12.

Figure 4.12 - ICMEs encountered by Parker Solar Probe on 26 September 2021.

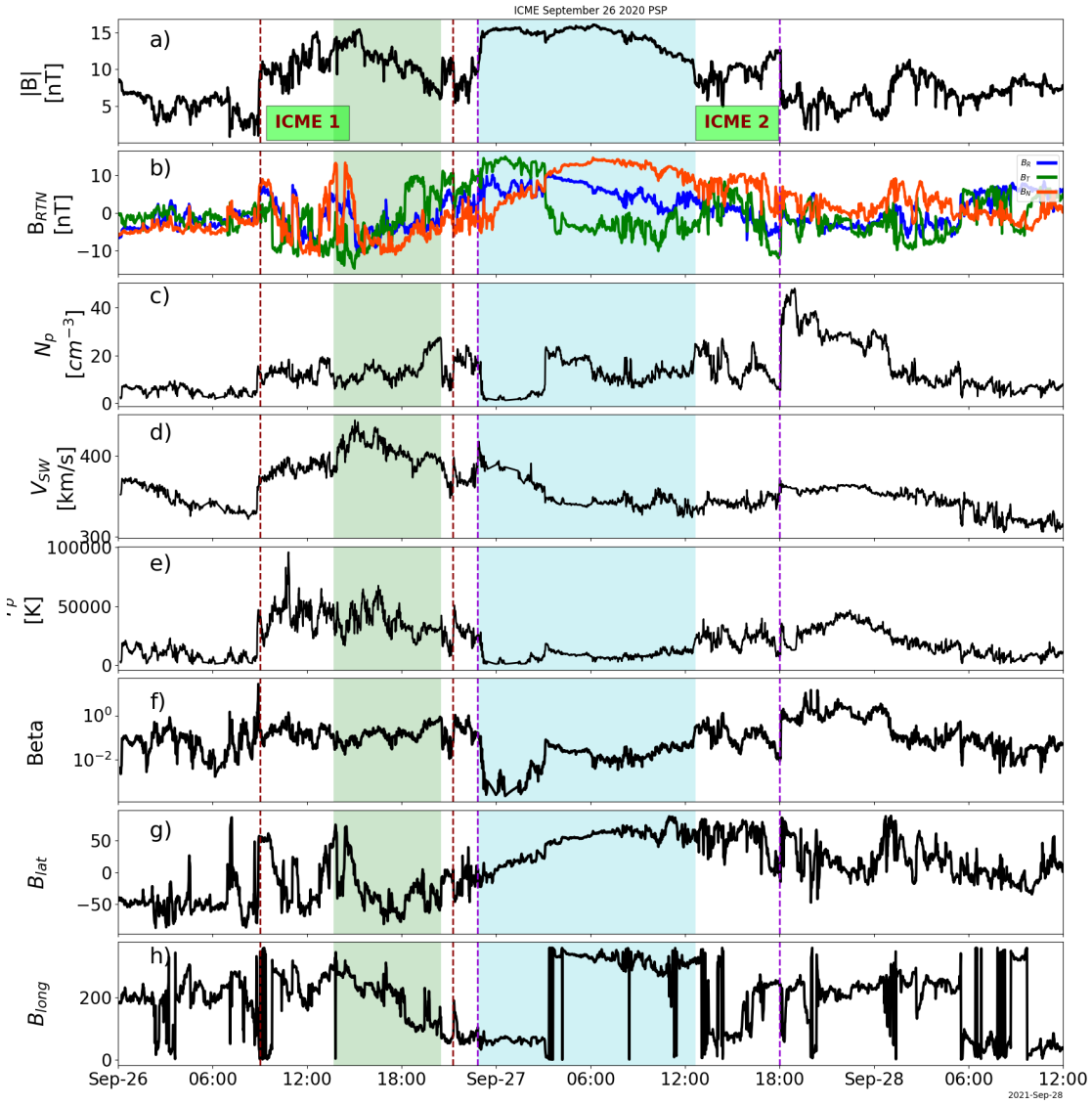

ICME1 is enclosed in red lines, and ICME2 is enclosed in dark violet lines. MC1 is coloured green and MC2 is coloured blue. From the top, (a) is the magnitude of the magnetic field $|B|$, (b) magnetic field components B_{RTN}, (c) proton density N_p, (d) solar wind speed R component V_r, (e) proton temperature T_p, (f) plasma beta β, (g) latitude component (polar angle) of $\vec{B}$, B_{Lat} and (h) longitude component (azimuthal angle) of $\vec{B}$, B_{Long}.

SOURCE: Author.

The computation of the average speed of the ICMEs shows that ICME1 is travelling at an average speed of 54 km/s faster than ICME2. This is the reverse of the inferred velocity from the remote observations. ICME1 appears to have accelerated while ICME2 decelerated such that it appears that the separation between the two events has increased from ≈11 hours at the Sun to ≈14 hours in situ at PSP. However, since

there are no perfect boundaries for the ICMEs, and their selection is based on visual observation, it could also be reasoned that the two ICMEs are gradually overlapping, and ICME1 magnetic field components are getting deformed. It is observed that ICME2 has a clear and simple FR rotation for ≈13 hours, while ICME1 appears to have a complex, altered or compressed FR rotation for ≈7 hours.

4.3.1.2 Remote observations

To ascertain the direction of propagation and source condition of the ICMEs, it is important to locate their origin on the Sun. The ICMEs were tracked and connected to two of the eruptions that occurred on 23 September 2021.

ICME1 from PSP observation was linked to the first of the two eruptions, **CME1**, which started at about **05:48 UT on 23 September, 2021** as observed by the SDO/AIA in Figure 4.13b. It was later captured by the C2 and C3 coronagraphs of LASCO aboard the SOHO space mission. The top panel of Figure 4.13 shows the evolution of CME1 eruption as observed by SOHO/C2. There are multiple CMEs erupting almost simultaneously towards the East of the CME, forming a "spiral-like" structure, as captured in Figure 4.13, but they do not appear to interfere with CME1.

CME1 erupted from the active region 12871, shown in Figure 4.13b. It erupted when the active region was located at S22E28 on the Sun and was detected by STEREO-A instruments, SECCHI/COR2. An M2.8 class solar flare is also linked to the eruption of CME1[3]. It erupted from the same region at 04:20 UT (≈1 hour prior) and was observed by the GOES spacecraft. The dimming and post-eruption brightening was also observed in EUVI-A 195.

CME1 was estimated to have a linear speed of 264 km/s and decelerated by 0.8 km/s^2 (uncertain value). It is important to note that the linear speed increased so much that its maximum speed observed at PSP was $V_{max} = 444$ km/s. This could be explained by the action of CME2 which was travelling at a much faster linear speed of 435 km/s. Thus, pushing the CME1 ahead, such that the speed of ICME1 in situ rapidly increased by PSP observation. The angular width is 42° and the quality index is considered to be "fair"[4]. Using CME input parameters, the WSA-ENLIL+cone model predicted that the glancing bow of CME1 will touch Earth and could impact PSP, Solar Orbiter and STEREO-A.

[3]CCMC DONKI WSA-ENLIL+Cone model simulations
[4]SOHO/LASCO CME Catalogue

Figure 4.13 - Evolution of CME1 that erupted on 23 September 2021 at 05:48 UT.

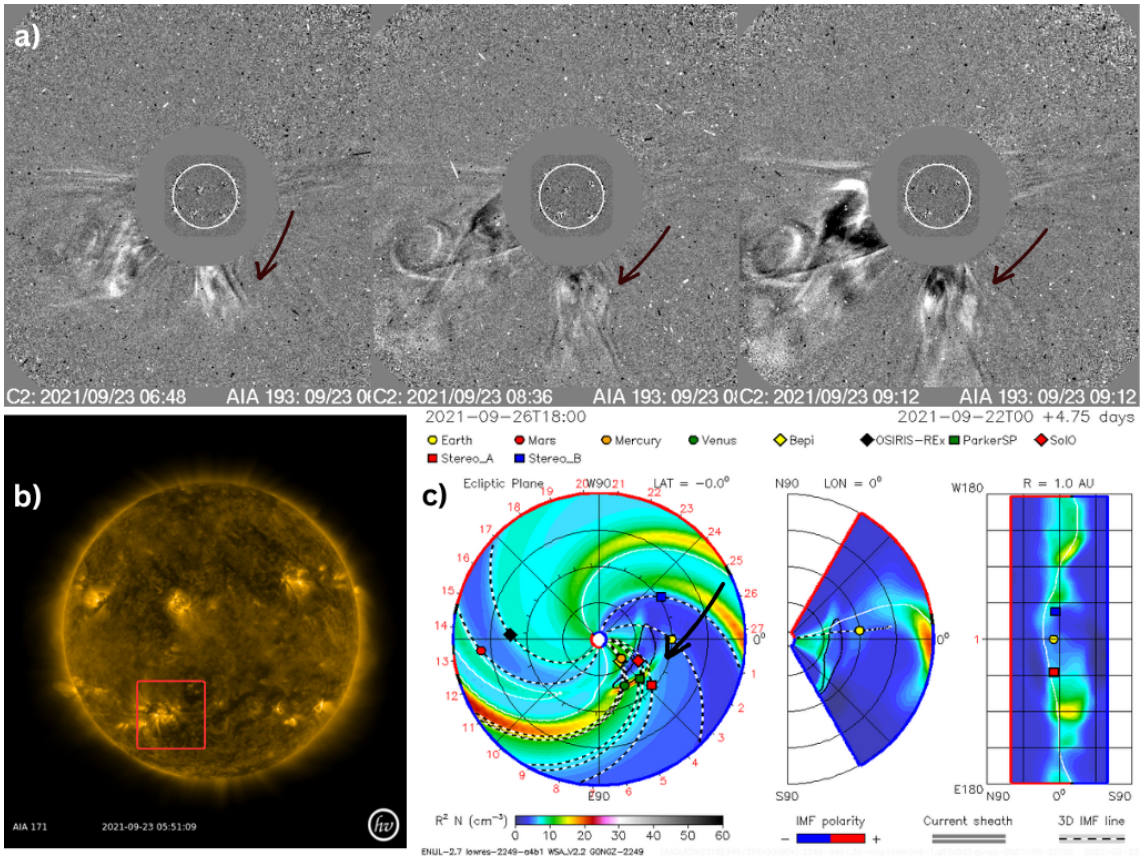

a) CME1 in white light as captured by SOHO/LASCO-C2 with a running difference. b) SDO AIA showing the active region 12871 where it erupted from. c) WSA-ENLIL+cone model simulation of the CME propagating (arrow points towards it) from the Sun.

SOURCE: CDAW website and CCMC DONKI, Gopalswamy et al. (2009), Pizzo (2011).

ICME2 was tracked and connected to the second CME eruption (**CME2**) that erupted at **16:12 UT on September 23, 2021** using the catalogue on NASA/GSFC/CDAW website[5]. This will be called CME2. It was visible from the C2 and C3 coronagraphs of the LASCO instrument aboard SOHO. The linear speed of the CME is estimated to be 435 km/s, which is moderately fast and estimated to be accelerating at the rate of 22.2 m/s^2. This is not so far off from its maximum speed of (ICME2) that was observed by PSP which is $V_{max} = 418$ km/s. The "averagely" fast linear speed of CME2 explains why it was able to catch up with the slow linear speed of CME1 which was 264 km/s. CME2 has an angular width of 104°, which is slightly more than CME1, and the quality index of this CME is considered to

[5]SOHO/LASCO CME Catalogue

be "fair" also. The observations of CME2 as it evolves outward are shown in Figure 4.14.

Figure 4.14 - Evolution of CME2 in white light as captured by SOHO/LASCO-C2 with a running difference. The CME erupted on 23 September 2021 at 16:12 UT.

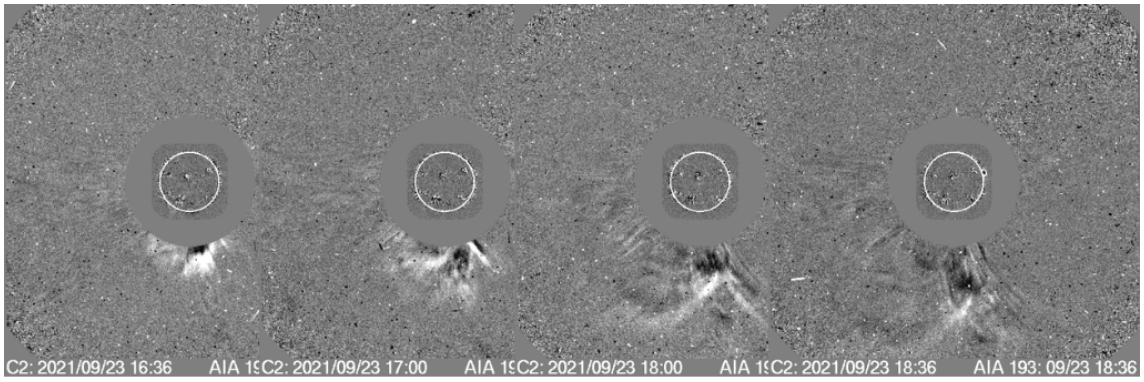

SOURCE: Adapted from CDAW website Gopalswamy et al. (2009).

CME2 erupted from the same active region number 12871, where CME1 also ejected from, but when it was located at S28W16 and was also observed by STEREO-A/SECCHI/COR2. The longitude of the CME is 16° to the east of the Sun-Earth line and has a latitude of −21°. This eruption has been linked to an M1.8 class solar flare that started at 15:23 UT and ended at 15:39 UT on 23 September which was observed by GOES spacecraft. The solar flare was released from the same active region and could have triggered it[6]. Using these parameters as input into the WSA-ENLIL+cone model, it also predicted that the glancing bow of CME2 will hit Earth and the CME would also be observed by PSP, Solar Orbiter and STEREO-A (with minor impact).

4.3.1.3 Multiple in situ observations

In an attempt to study the structure of the ICMEs before and after observation at PSP, we traced the ICME towards the Sun and outwards. We identified five more spacecrafts that are within close longitudinal distances and observed the two ICMEs: Solar Orbiter, BepiColombo, STEREO-A, ACE and WIND. ACE and WIND are located near L1, and thus had similar measurements of the events. A summary of the spacecrafts and their location with respect to Earth and the ICMEs apex is given in Table 4.4.

[6]CCMC DONKI WSA-ENLIL+Cone model simulations

Table 4.4 - The location of the spacecrafts that observed the ICMEs at the time of PSP measurement on September 26, 2020.

	BepiColombo	**SolO**	**PSP**	**STEREO-A**	**L1**
Stonyhurst longitude [°]	-47.0	-29.8	-42.7	-39.9	0.0
Stonyhurst latitude [°]	-0.0	1.9	3.5	6.8	6.9
Heliocent. distance [AU]	0.43	0.61	0.78	0.96	0.99
Longitud. separation to Earth longitude [°]	-47.0	-29.8	-42.7	-39.9	0.0
Latitud. separation to Earth latitude [°]	-7.0	-5.0	-3.4	-0.1	-0.0
Longitud. separation to ICME1 apex [°]	-31.0	-13.8	-26.7	-23.9	16.0
Latitud. separation to ICME1 apex [°]	21.0	22.9	24.5	27.8	27.9
Longitud. separation to ICME2 apex [°]	-15.0	2.2	-10.7	-7.9	32.0
Latitud. separation to ICME2 apex [°]	14.0	15.9	17.5	20.8	20.9

Note: Heliocent. distance represents heliocentric distance. SolO is Solar Orbiter and L1 represents two of the spacecrafts located there, ACE and WIND.

SOURCE: Adapted from SOLAR MACH tool, Gieseler et al. (2022).

From the table, BepiColombo is the only spacecraft located at heliocentric distance < 0.5 AU. Also, Solar Orbiter has the least longitudinal separation from ICME1, while BepiColombo has the least for ICME2. ACE and WIND (at L1) have the highest deviation from both ICMEs, thus aiding the study of their flanks.

Table 4.4 and Figure 4.15 shows that spacecrafts 1–4 are closer to the apex of ICME2 (CME2) than the apex of ICME1 (CME1). However, CME2 has a wider angular width of 104° compared to CME1 with an angular width of 42°[7]. So, due to the propagation direction of the events and their angular width, they were well observed by the six spacecrafts. However, data from BepiColombo was not used for the study.

Figure 4.17 shows the plot of the magnetic field magnitude and components measured by Solar Orbiter (SolO), PSP, STEREO-A, ACE and WIND. SolO, PSP, and STEREO-A data measure these parameters in the RTN coordinate system, WIND measures in the GSE coordinate and ACE measures in RTN, GSE and GSM coordinate system. The variation of the magnetic field components in RTN B_{RTN} can

[7]SOHO/LASCO CME Catalogue

Figure 4.15 - Map of the location of BepiColombo (yellow), Solar Orbiter (blue), Parker Solar Probe (violet), STEREO-A (red) and spacecraft at L1 (black, WIND and ACE) on September 26, 2021. The black arrows represent the central direction of propagation of the CMEs.

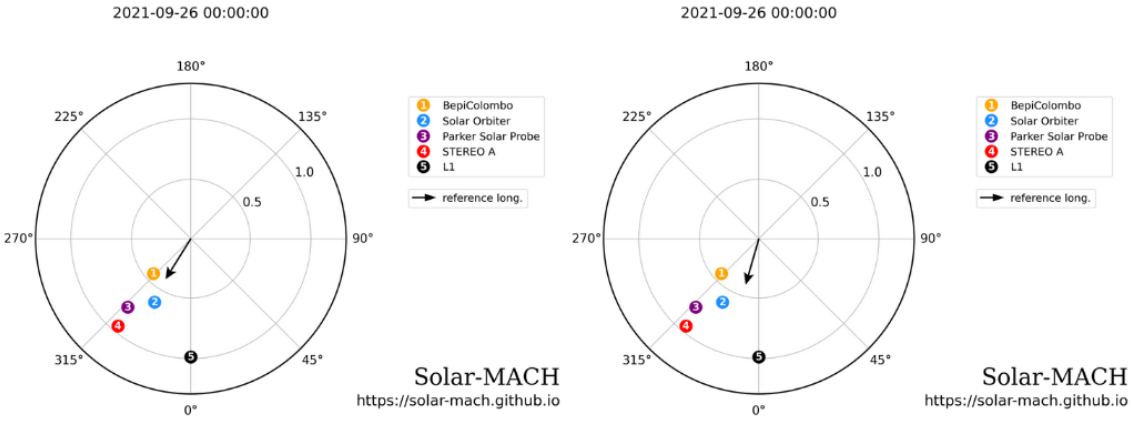

Left panel: CME1 (ICME1) of longitude $-32°$ and latitude $-14°$. Right panel: CME2 (ICME2) of longitude $-16°$ and latitude $-21°$.

SOURCE: Solar MACH tool, Gieseler et al. (2022).

be visually compared with that measured in GSE B_{xyz} knowing that $B_r \equiv -B_x$ (x points from Earth to Sun but r points outward from the Sun), $B_t \equiv B_y$ (y is on the ecliptic plane but opposite planetary motion and t is along planetary motion). B_z is directly compared to B_n since they both point northward, perpendicular to the ecliptic plane.

Figure 4.15 shows that **SolO** made the second observation of the ICMEs on **25 September 2021 at 07:10 UT** (Figure 4.16), and crossed closest to the apex of the ICMEs. However, the data gap that started at 18:00 UT made it hard to identify the leading edge of ICME1 and ICME2. It is suspected that ICME1 arrived at about 07:00 UT characterised by the sudden enhancement in magnetic field magnitude and the rotation of its flux rope, FR1, began at about 09:00 UT.

Figure 4.16 - In situ observation of $|B|$ and components of ICME1 and ICME2 by Solar Orbiter in RTN coordinate.

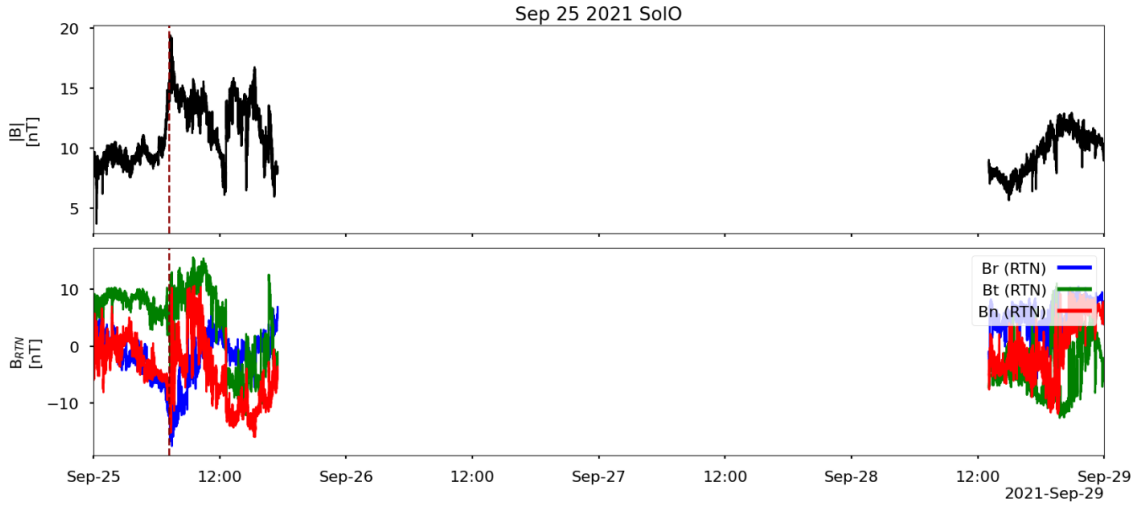

SOURCE: Author.

For the **PSP** observation (measured in RTN coordinates) on 26–27 September (Figure 4.17b), the B_n component of ICME1 rotates between 13:40 UT and 20:30 UT on September 26 which gives the flux rope structure (FR1) an orientation of **WSE**, by the visual observation of the longitudinal and latitudinal variation of the B components (Figure 4.12g and h). This orientation shows that the axis of the flux rope points southward. The second flux rope rotation, FR2, is observable from 22:50 UT on September 26 to 12:40 on September 27 which gives a flux rope orientation of **ENW**, i.e., the axis of the flux rope points is northward (Figure 4.12g and h).

Also, the eruption of CME1 and CME2 is about 11 hours apart, with CME2 travelling at a much higher speed than CME1. So, at PSP, ICME2 (CME2) is seen to be gradually merging with ICME1 (CME1) ahead, and still propagating at a higher speed.

The next observation of the ICMEs was at **STEREO-A** (Figure 4.17c) located at 0.96 AU, a close radial distance from L1, however, separated by 40° longitudinally. When the ICME arrived at STEREO at **22:00 UT on 26 September**, the two ICMEs are merged, but not completely, as a discontinuity is visible along the enhanced magnetic field magnitude and components. The discontinuity suggests the region where ICME1 is compressing ICME2. MC1 is measured from 04:30 UT to 13:00 UT on September 27 and MC2 is measured from 16:00 UT on September 27 to

Figure 4.17 - In situ observation of $|B|$ and components of ICME1 and ICME2 by Parker Solar Probe, STEREO-A, WIND and ACE.

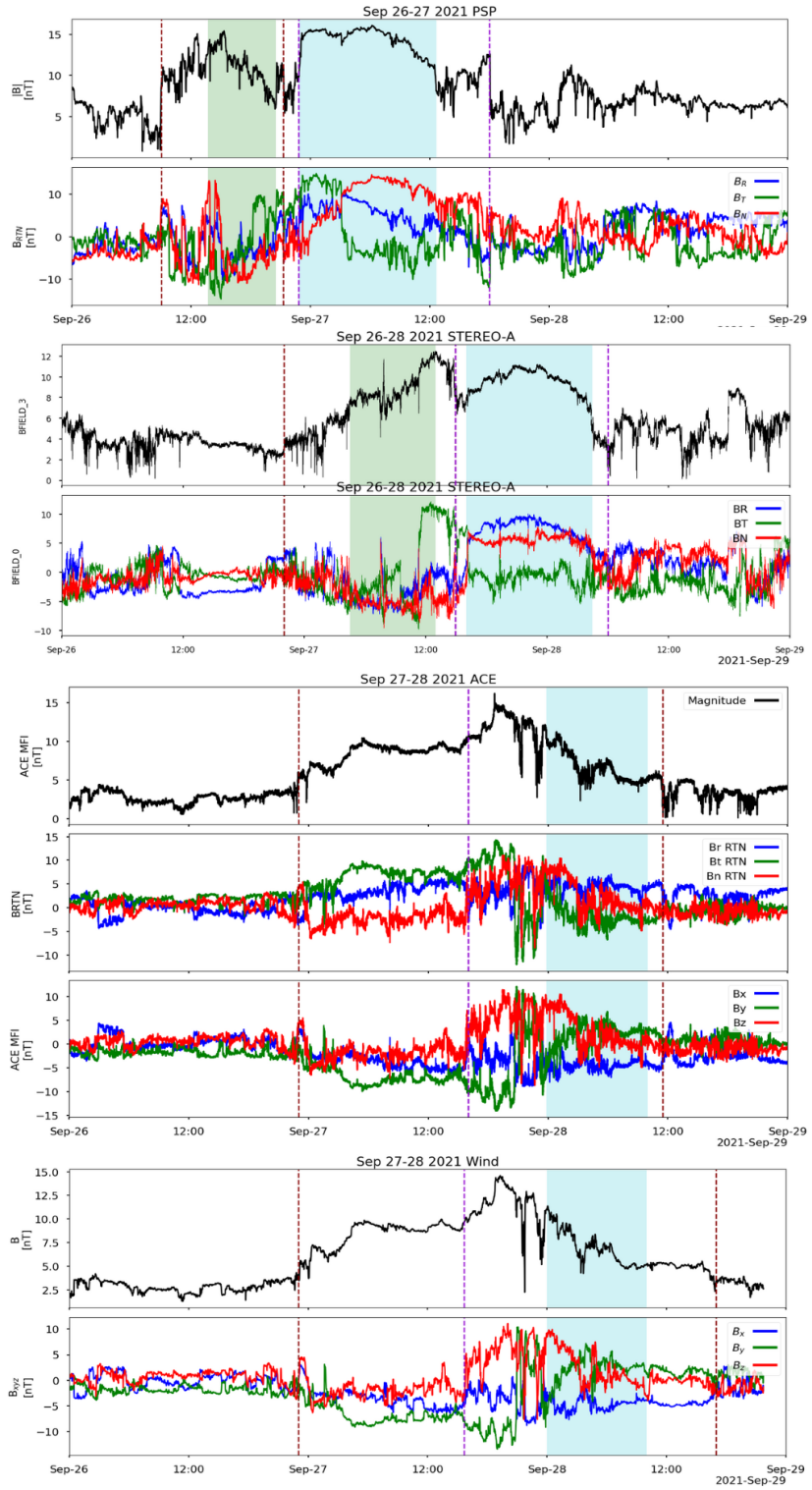

(a) SolO (RTN), (b) PSP (RTN), (c) STEREO-A (RTN), (d) ACE (RTN and GSE), and WIND (GSE). The plots are in the same time axis.

SOURCE: Author.

04:30 UT on September 28. From visual observation, the B_n component, measured in RTN coordinates, is still pointing southward and abruptly changes northward at the point of discontinuity. This is similar to the observation at PSP.

Finally, ACE and **WIND** located around L1 made observations of the ICMEs just before they hit Earth (Figure 4.17d & e). As expected, the shape and distribution of the magnetic field data look similar. The ICMEs (now merged) reached WIND at **23:00 UT on 26 September** and their trailing edge is observed at 17:00 UT on 28 September. The flux rope structure is deformed at this point and can be categorised as a complex flux rope with multiple rotations C_x as enumerated in Section 2.7 (NIEVES-CHINCHILLA et al., 2019), but a discontinuity can be observed from WIND measurement at 15:40 UT on 27 September.

This discontinuity is also observable from **ACE** measurement at **16:00 UT on 27 September**. So, we observe that the B_n component was still pointing southward just before the discontinuity and pointed northward afterwards. The orientations and behaviour of the magnetic field structures measured by WIND are the same as that measured by ACE in RTN and GSE coordinate systems.

It is also important to note that STEREO and the spacecraft at L1, WIND and ACE measured the merged ICMEs from opposite sides at approximately the same radial distances. **Did the spacecrafts observe similar magnetic structures at these opposite sides?** No they did not. It is hard to make a direct comparison here because the ICMEs appeared to have merged more at ACE compared to STEREO-A measurements. Yet, we could still observe from Figure 4.17, in the first part of both measurements, the B_n component is southward, and at the peak (B_{max}) and after, the B_n component points northward. This could suggest that the orientation of the magnetic structure of the interacting ICME is the same across the different longitudinal separations. This could also suggest that the interaction of the ICMEs was probably "uniform" across the longitudinal distances.

We studied the evolution of the ICMEs between **PSP and STEREO-A**. From Table 4.4, we see that the longitudinal separation between PSP and STEREO-A is 2.8°, latitudinal separation is 3.3°, and radial separation is 0.18 AU. The small separation distances and the pristine observation of the MCs by the spacecrafts make it a good case to investigate the evolution of the MC parameters.

The visualisation of the ICMEs plasma parameters in Figure 4.18 also shows similarities in the solar wind parameters measured by PSP and STEREO-A. The first panel

is the magnitude of the magnetic field $|B|$, followed by the density N_p, speed V_{SW}, and proton temperature T_p. The magnetic field magnitude (first panel, Figure 4.18) shows that the MCs are more merged at STEREO than at PSP. The plasma parameters have characteristics representative of MC, especially in the ICME2 region. The velocity is seen to be slowly decreasing in both spacecraft, signifying expansion and the temperature was depressed within the MC2 region. The compressed MC1 rather has an increased temperature in comparison with the ambient solar wind and MC2.

Figure 4.18 - Magnetic field magnitude and solar wind parameters: density, velocity and temperature measured by PSP (left) and STEREO (right).

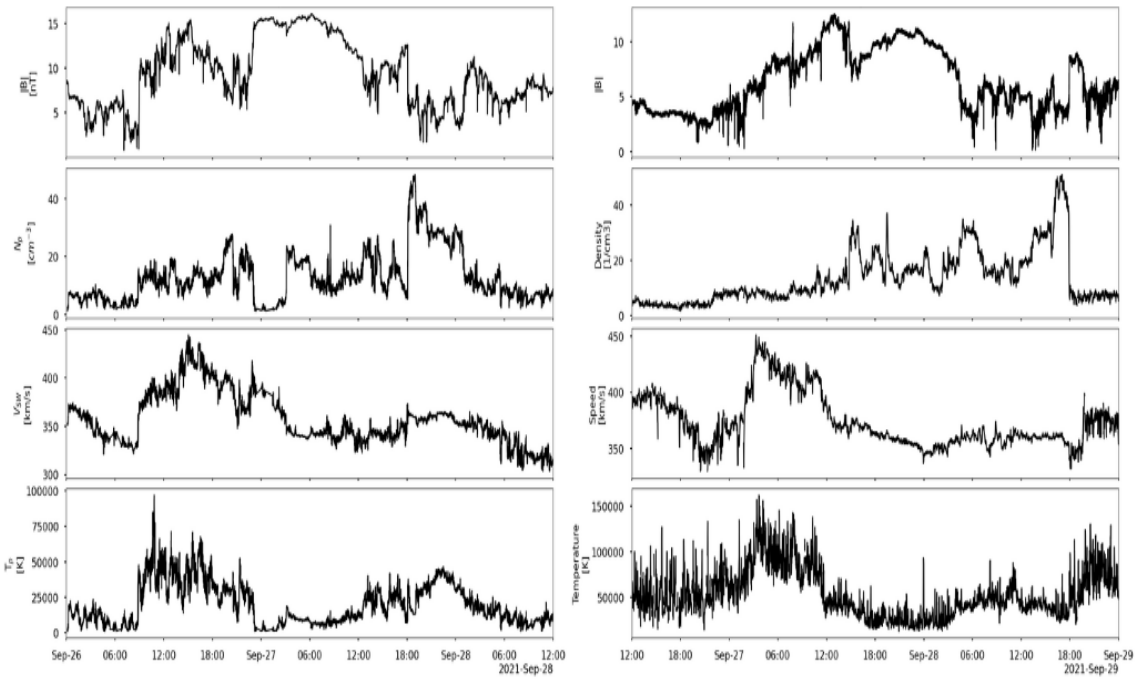

SOURCE: Author.

Table 4.5 presents a quantitative comparison between MC1 and MC2 as observed by Parker Solar Probe and STEREO-A. The table shows that there is negligible change in the flux rope type, chirality, radius, average velocity and impact parameter p estimated in both spacecraft observations. The different orientations of the axis of the flux ropes (derived from MVA) in the different spacecrafts could be due to different spacecraft crossing distances. Since the impact parameter, p is low for both spacecraft observations, the MVA estimations are considered to be accurate.

The decrease in the magnetic field intensity B is expected as it could be a result of erosion (PAL et al., 2020) as they interact with the ambient solar wind or expansion. A more detailed quantitative comparison of this event and other events studied in this research is presented in Table 4.6 in the final section.

Table 4.5 - Comparison of the MCs parameters as observed by PSP and STEREO-A, located at different longitudinal, latitudinal and radial positions.

	PSP [RTN]	**STEREO-A [RTN]**
MC1		
FR type	WSE	WSE
Chirality	LH	LH
ϕ_{axis}, θ_{axis}	(226°, -56°)	(167°, -34°)
χ [°]	165	92
R_{MC} [AU]	0.07	0.08
V_{avg} [km/s]	408	409
V_{exp} [km/s]	13	21
B_{max} [nT]	15	12
p	0.18	0.18
MC2		
FR type	ENW	SEN/ENW
Chirality	LH	LH
MVA axis	(186°, -18°)	(62°, 16°)
χ [°]	113	104
Radius [AU]	0.12	0.11
V_{avg} [km/s]	353	358
V_{exp} [km/s]	27	13
B_{max} [nT]	16	11
p	0.20	0.24

Note: χ is rotation angle which must be greater than 30° to be considered a FR. ϕ_{axis}, θ_{axis} is the orientation of the FR as determined from the MVA application. p is the impact parameter which must be low to validate the accuracy of MVA results.

SOURCE: Author.

Also, shown in Figure 4.19 are the magnetic hodograms for **PSP and WIND** observations of MC2 embedded in ICME2. The hodogram for WIND is calculated in the FR region shown in Figure 4.17e.

Figure 4.19 - Magnetic hodogram of MC2 derived from PSP (top panel) and WIND (lower panel) measurements.

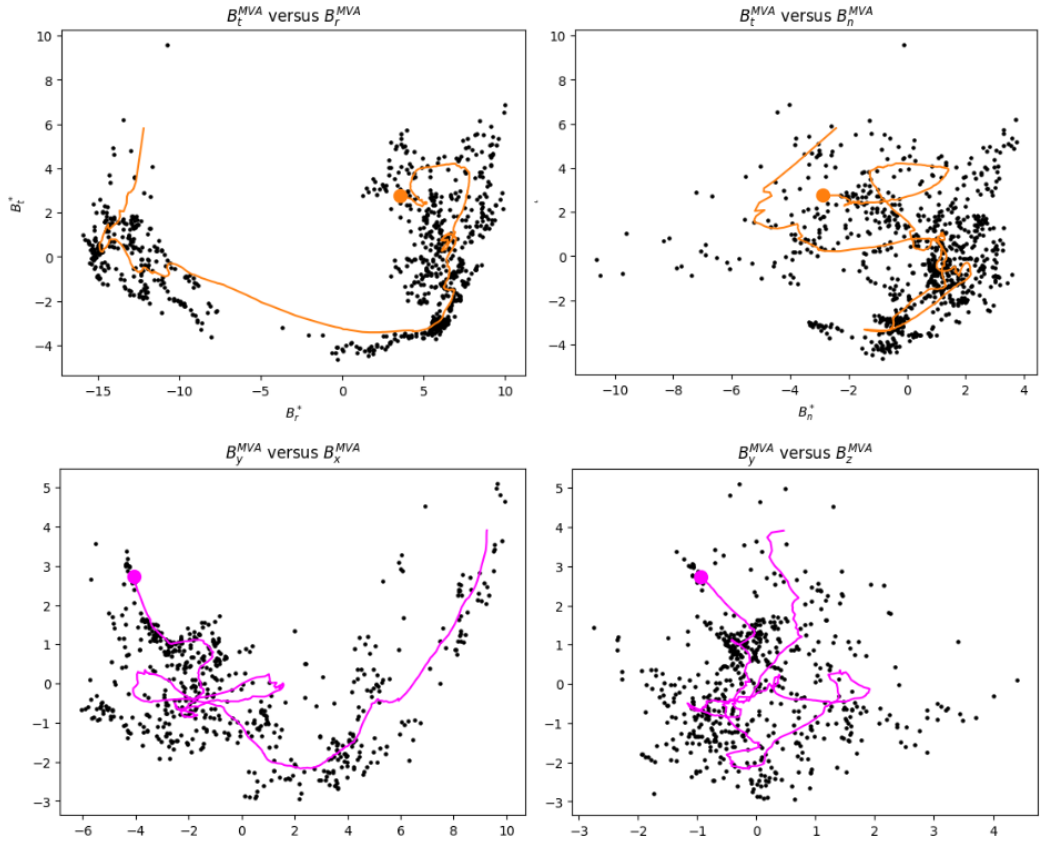

Left panel: maximum variance plane. Right panel: minimum variance plane.

SOURCE: Author.

4.3.1.4 Force-free modelling

Of all the ICMEs and their embedded flux rope structures, the magnetic cloud found in ICME2 observed by PSP has the clearest and simplest rotation. So we applied the force-free model to see if the magnetic field magnitude and its spherical components can be reproduced by the force-free model. The result is shown in Figure 4.20.

The model was able to mimic the direction of the longitudinal variation (ϕ) of the magnetic field and its magnitude $|B|$. But the latitudinal component (θ) is Southward within the MC, while the force-free fitting shows a variation from South to North.

The distance correlation, between the Lundquist force-free fitting and the estimated latitudinal data, is 0.87, which signifies a good fitting. The distance correlation for the longitudinal variation is 0.78. This shows a good fitting too.

Figure 4.20 - Force free fitting of MC2 observed by PSP.

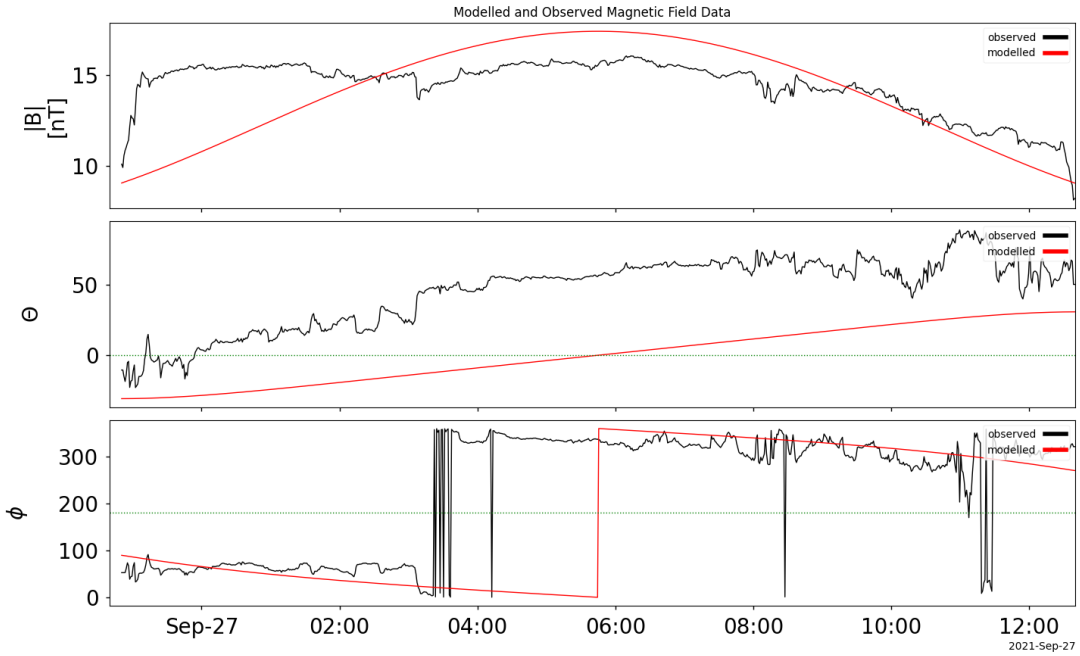

From the top: magnetic field magnitude, latitude and longitudinal variation of the magnetic field.

SOURCE: Author.

4.3.1.5 Geomagnetic impact of the interacting ICMEs

The ICMEs' eventual arrival at Earth was captured by ACE and WIND (Figure 4.17). An initial increase in $|B|$ began at about 23:00 UT on 26 September 2021, crossing 10 nT at 04:00 UT on 27 September. We could not visualise the solar wind data due to its unavailability. Nevertheless, with the northward configuration and low $|B|$ intensity observed just before the ICMEs interacted with Earth, a geomagnetic storm is not expected.

Visual observation of the B_n and B_z components of the interacting ICMEs observed by WIND and ACE (Figure 4.17d & e) shows a majorly northward component. We checked the world data centre for geomagnetism for the Dst index values and observed that there was no depression of the horizontal component of Earth's magnetic field, such that the Dst values were increasingly positive during this period until 12:00 UT on 28 September when it crossed to negative. The Dst_{min} observed was

at 14:00 which was -2.0 nT.

4.3.2 Example 2: July 7, 2022 ICMEs

On the **3rd of July, 2022, at 03:09 UT**, STEREO-A/SECCHI/COR2 and SOHO/LASCO/C2 observed a very, very faint partial halo CME. The partial halo CME was extremely faint and barely observed at the West of the COR2 image. Only the front is distinguishable. It **overlapped** with a more observable but faster and narrower CME that erupted approximately an hour later at 04:12 UT, shown in the top panel of Figure 4.21. This is pointed to by the brown arrow in the Figure, and almost simultaneously a bigger CME was erupting, which is shown by the green arrow.

According to the simulation provided by the WSA-ENLIL+cone model, shown in Figure 4.21d, the partial halo CME eruption of 03:09 is linked to the in-situ observation (of the ICME flank) at PSP on 4 July 2022. It is also linked to the observations made by spacecrafts located close to Earth (represented by a yellow circle): WIND and ACE on 7 July 2022. However, due to the faintness of the CME, it is difficult to ascertain the properties of the CME on the Sun, thus causing uncertainties in the CME analysis presented.

However, from the input parameters used in the DONKI space weather database[8], the longitude of the CME is estimated to be -2°, latitude of 6°. They also deduced that the eruption could be associated with a very slow, large and central filament eruption, because of post-eruptive arcades that close out more than half a coronal hole observable at the southern side of the Sun. It is important to note that the analysis should not be taken with certainty.

[8] CCMC DONKI WSA-ENLIL+Cone model simulations

Figure 4.21 - Remote observation and outward propagation of July 3, 2022 CME.

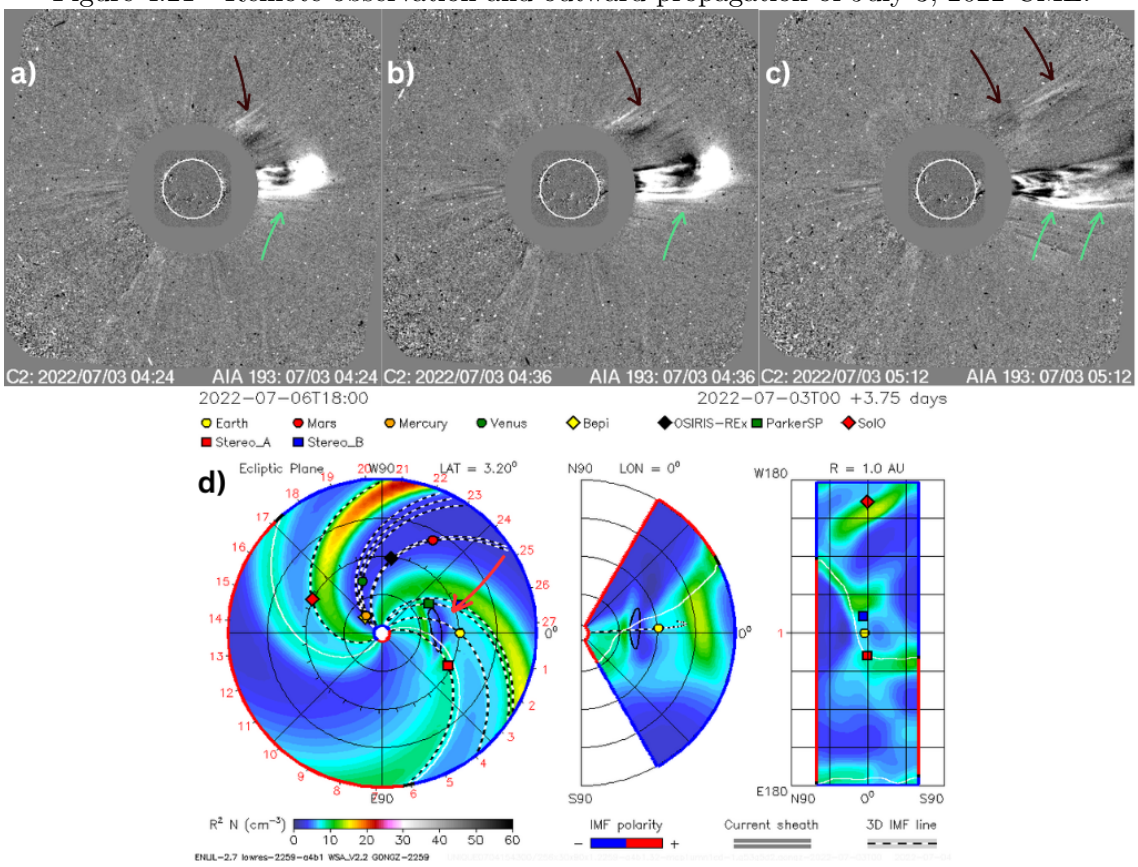

Top panel: (Brown arrows) SOHO/LASCO/C2 image (running difference) showing the overlapping CME that erupted around 04:12 UT. (Green arrows) Another CME erupting almost simultaneously in another direction. Bottom panel: WSA-ENLIL+Cone model of the CME in the solar equatorial plane, meridional plane at the Earth longitude and 1 AU sphere in cylindrical projection. PSP is the green square and WIND is close to Earth (yellow circle) and the arrow points to the CME.

SOURCE: CDAW website and DONKI CCMC simulation Gopalswamy et al. (2009), Pizzo (2011).

4.3.2.1 In situ observations

From the simulation and the derived direction of the CME propagation, it is expected that the flank of the ICME will hit PSP and the spacecrafts located at L1, will cross the ICME close to its apex. This is confirmed in the visualization of the in-situ observation, as the time-series plot created from PSP observation barely shows a flux rope rotation while there is a very clear and pristine flux rope rotation observed at the WIND spacecraft.

The observation at **Parker Solar Probe** is shown in Figure 4.22 with the ICME at **20:50 UT on July 4, 2022** and ending at 9:40 UT on July 6, 2022. The

Figure 4.22 - ICME encountered by Parker Solar Probe on July 5, 2022.

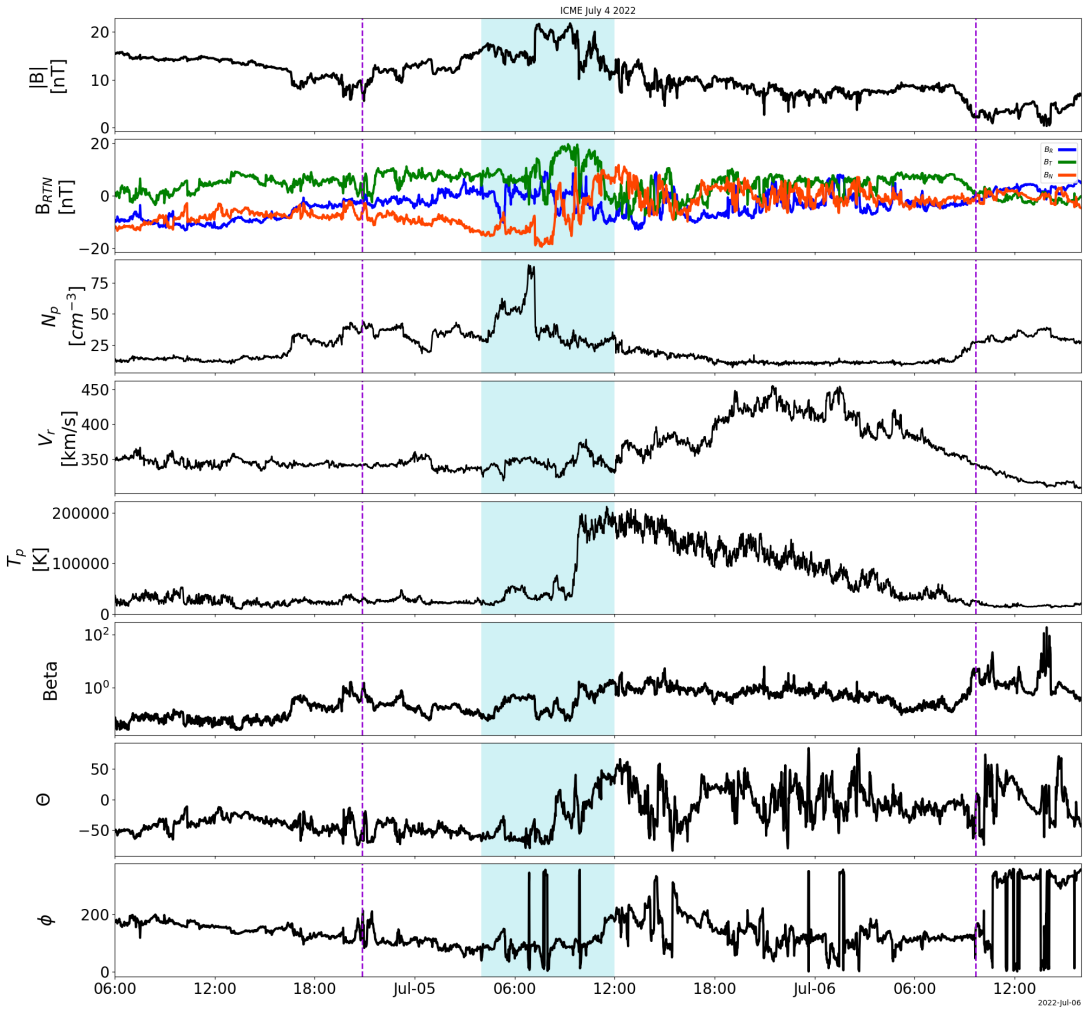

ICME is enclosed in dark violet lines. FR is coloured blue. From the top, (a) magnitude of the magnetic field $|B|$, (b) magnetic field components B_{RTN}, (c) proton density N_p, (d) solar wind speed R component V_r, (e) proton temperature T_p, (f) plasma beta β, (g) latitude component (polar angle) of $\vec{B}$, θ and (h) longitude component (azimuthal angle) of $\vec{B}$, ϕ.

SOURCE: Author.

boundaries of the ICME are marked with violet dotted lines. Between 04:00 UT and 12:00 UT on July 5, 2022, a small "flux rope" rotation could be seen embedded in the ICME which is enclosed in blue in Figure 4.22. From the time-series plot of PSP observation, $B_{max} \approx 21.7$ nT and B_n is rotating from south to north. The orientation of the magnetic field can be deduced to be **SEN**. In the region of the small-scale flux rope rotation, it is marked by a sudden increase and then a decrease in the density from ≈80 cm^{-3} to ≈25 cm^{-3}. The temperature is observed to experience a sudden increase from ≈48000 K to ≈200,000 Kelvin, followed by a gradual decrease until the original range. There is no depression in the plasma beta β, but the values were majorly below 1. Hence, in the absence of good qualities expected of a magnetic cloud, we could not conclude that the PSP spacecraft observed an MC at the flank of the propagating ICME.

For further understanding of this ICME, we studied the observation close to the Earth by the WIND and ACE spacecraft. The time series of **WIND** observation is shown in Figure 4.23, as the ICME observation began at **08:00 UT on 7 July 2022** and ended at about 20:10 UT on 8 July 2022. The observed magnetic field data increased from about 5 nT observed in the solar wind to ≈23 nT within the magnetic cloud, and B_{mean} within the magnetic cloud is 19.46 nT. The rotation of Bz component, depressed density, temperature and beta signified the presence of the magnetic cloud and aid the selection of the boundaries, unlike the in situ measurement by PSP in Figure 4.22. The clear flux rope structure observed can be alluded to the location of WIND which is close to the apex of the erupting CME. There appears to be rotation in both B_t and B_n components of the magnetic flux rope, which is not always observed. This is a "double" flux rope rotation. We enclosed the region of the flux rope in blue within the minimum and maximum value of the B_n component. Consequentially, the θ and ϕ shown in Figure 4.23 yield an orientation of **SWN/ESW** and the chirality of both configurations is **right-handed**. The application of the force-free model will aid in the selection of the most accurate representation of the orientation.

Furthermore, we applied MVA and create a plot of magnetic hodogram of the WIND spacecraft observation only, due to poor rotation in the PSP observation. The hodogram, shown in Figure 4.24, further confirms that the chirality of this magnetic cloud is right-handed as a clockwise rotation is observed in the maximum plane (right hand). The closed dot signifies the end of the rotation.

From the application of MVA, the axis of the flux rope is, $\phi_{axis} = 98°$ and $\theta_{axis} = 44°$.

Figure 4.23 - ICMEs encountered by WIND on 7 July 2022.

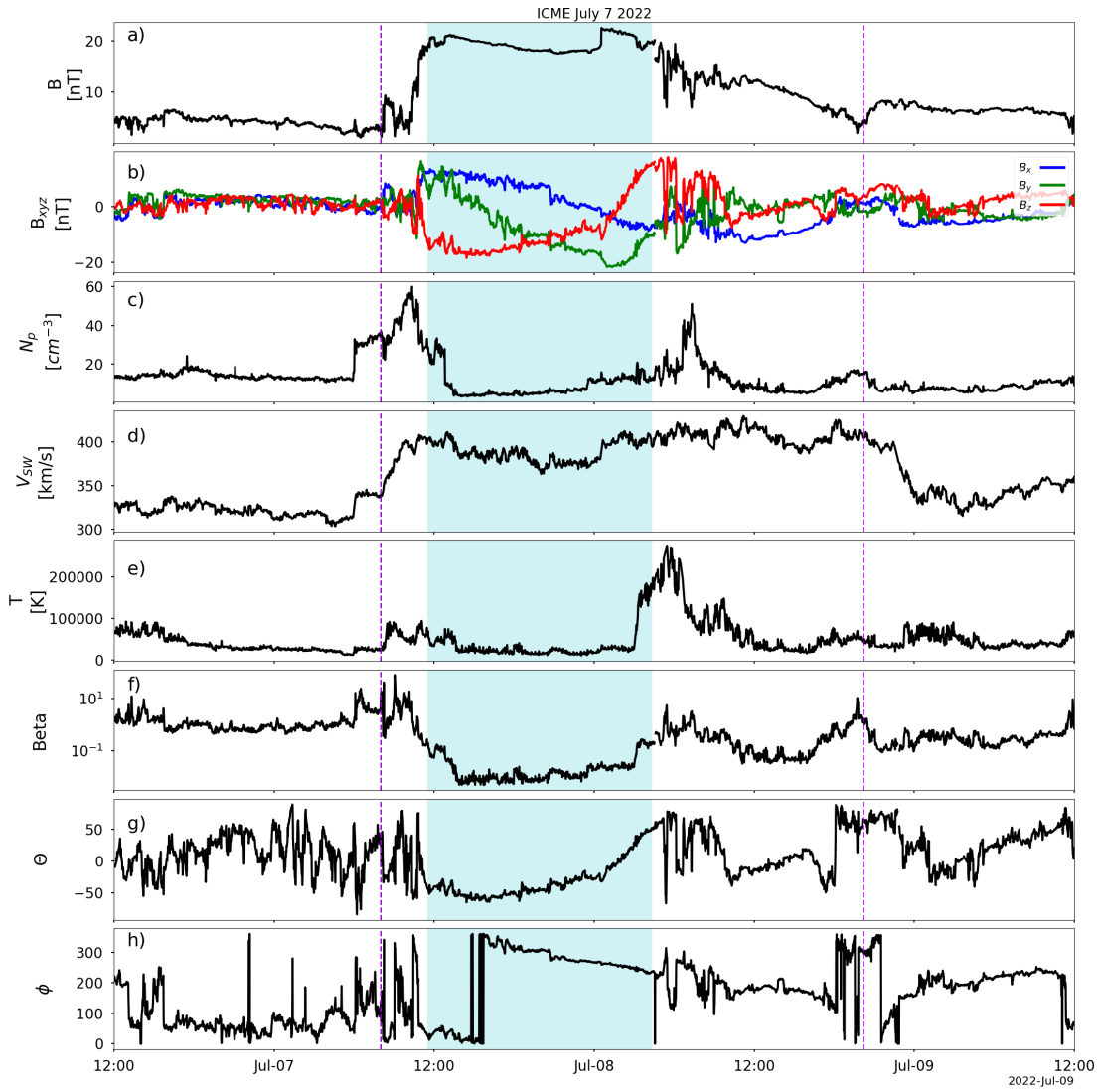

ICME is enclosed in dark violet lines; MC is coloured blue. (a) magnetic field magnitude $|B|$, (b) magnetic field components B_{xyz}, (c) proton density N_p, (d) solar wind speed V_{SW}, (e) proton temperature T, (f) plasma beta β, (g) $\vec{B}$ latitude component, θ and (h) $\vec{B}$ longitude component, ϕ.

SOURCE: Author.

Figure 4.24 - Magnetic hodogram of July 7, 2022, MC observed at WIND spacecraft.

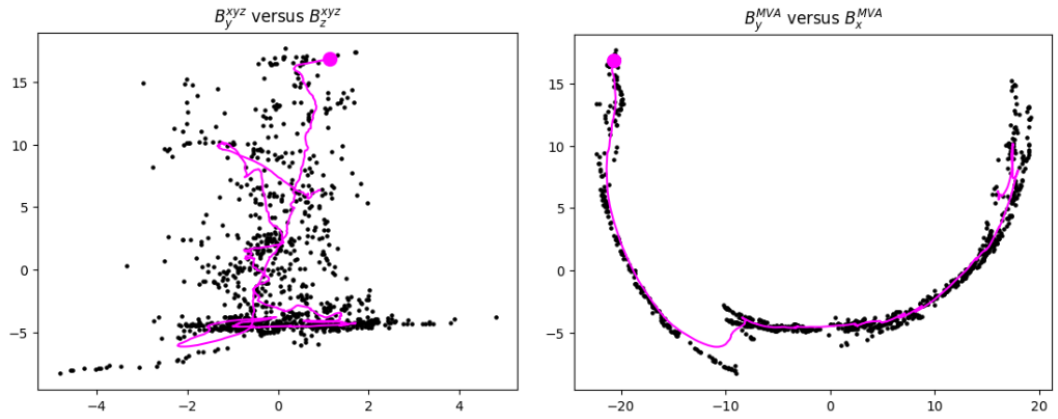

Left: minimum variance plane. Right: maximum variance plane.
SOURCE: Author.

Since the θ_{axis} is $< 45°$ (just above the limit), it represents a bipolar flux rope with a low inclination. We can conclude that the orientation of the flux rope is **SWN**. At the evaluation of the error criteria for the MVA application, it is seen that its application can be considered accurate as $\lambda_2/\lambda_3 = 25$ and $\lambda_1/\lambda_2 = 3.18$. The P metric is 18.1 and the angle of rotation of the magnetic field components is 157°. The impact parameter $p = 0.07$ shows that WIND crossed close to the axis of the flux rope and the location angle $L = 3.6°$ represents a very close proximity to the nose of the ICME as the observation is being made.

4.3.2.2 Force-free reconstruction

Finally, we create a force-free fitting of the magnetic field magnitude and its spherical components to further fine-tune the orientation of the analysed magnetic flux rope. One of the input parameters, H, was set to be $H = 1$ and theta was rotated by 90° in order for the model to imitate the direction of variation of θ and ϕ. This is shown in Figure 4.25.

Finally, we verified the accuracy of the Lundquist fitting using the distance correlation parameter. For the latitudinal variation, the value is 0.85 and for longitudinal variation it is 0.75. Both values are close, so it shows that the fittings were good enough.

Figure 4.25 - Force free fitting of July 7, 2022, MC observed by WIND.

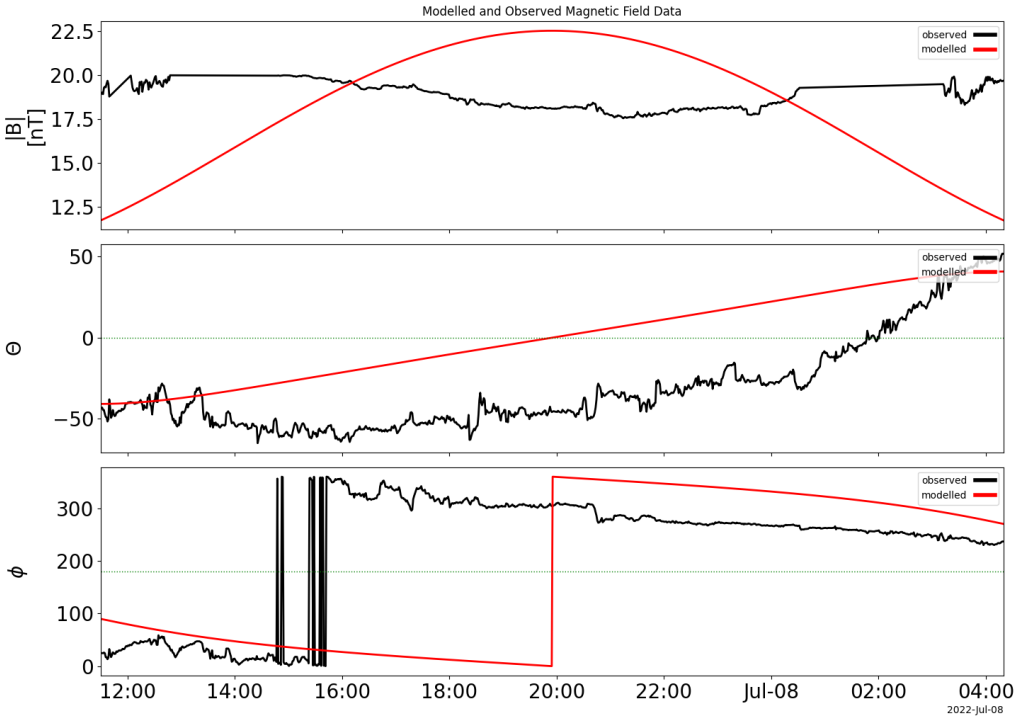

From the top: magnetic field magnitude, latitude and longitudinal variation of the magnetic field.

SOURCE: Author.

4.3.2.3 ICME arrival at Earth

The earthward direction of the ICME with strong magnetic field intensity and rotation of its components already suggested a strong impact on Earth's magnetopause. A strong compression of the magnetosphere was then confirmed by the measured values of the *Dst* index by the world data centre for geomagnetism in Kyoto.

The *Dst* index dropped sharply from 6 nT to -21 nT at 15H on July 7, 2022. It soon reached a minimum value of -82 nT at 23H the same day, signifying a geomagnetic storm. The *Dst* index remained below -50 nT until 04H on July 8, 2022.

4.4 PART IV: controversial events

Multispacecraft observations are important for understanding the global configuration of interplanetary coronal mass ejections (ICMEs) when properly connected with the source CME, and within the interplanetary medium. This section contains

analysed multipoint events whose results contradict a previously done research.

4.4.1 June 23 – 30, 2020 ICMEs

A certain event was observed in situ on **June 25, 2020**, by **PSP**, and it was connected with **BepiColombo** observation on the **29th of June, 2020** and to **WIND** observation on the **30th of June, 2020**. The interplanetary observations were connected to the **June 23 eruption** observed by **STEREO-A/COR-2 and LASCO**. This analysis was extensively done in an article by Möstl et al. (2022).

However, when this event was re-analysed, it was discovered that there were three overlapping eruptions from sources with short separating distances and within a short period, thus leading to wrong ICME connections between PSP and WIND spacecraft in the second ICME, but the connection with the CME source was accurate. The three CMEs and ICMEs are analysed below, with a brief overview of the first event. However, the major focus was on the second event, because it had the clearest flux rope structure at PSP with a fair quality at WIND spacecraft and was erroneously linked to the third event observed by WIND.

4.4.1.1 First eruption: June 23, 2020, ICME observed by PSP

On the **23rd of June, 2020, at 03:20 UT**, a shock was observed at **PSP** with abrupt changes in the magnetic field, density and beta parameters. PSP was situated at 0.47 AU, 17.4° longitude from Earth's longitude, 5.9° away from the apex of the CME longitude and 0.2° latitude away from Earth's latitude given in HEEQ. There was no sheath following the shock, but at 06:55 UT, the same day the magnetic flux rope-like structure was observed, which was characterised by a small rotation until 16:40 UT the same day. The MC speed is greater than the ambient solar wind by about 60 km/s and is seen decreasing gradually as it expands past the observing spacecraft. With an average speed of $\approx$ 360 km/s, this is an ICME of average speed.

Given below in Figure 4.26 is the plot of the observation at PSP with the MC characterised by a small rotation in the B_n component of the magnetic field (Figure 4.26b), reduced density (Figure 4.26c), decreasing velocity (Figure 4.26d), reduced temperature (Figure 4.26e) and depressed beta (Figure 4.26f) in comparison with the ambient solar wind. The trailing edge of the ICME was hardly noticeable due to the erosion of the ICME, but it was marked at 04:00 UT on 24 June 2020.

Application of the MVA results in a bipolar flux rope orientation of **SWN** with an axis of 339° longitude and −36° latitude. It met the error criteria which determines

the accuracy of the MVA application. The resulting hodograms are shown in Figure 4.26 where the rotation in the minimum variance plane is seen to be poor but still right-handed which agrees with orientation SWN derived using the longitudinal and latitudinal variation of B (Figure 4.26g & h).

As the event is traced to the Sun, it is observed that the source of this CME is a filament eruption that was observed on **SDO/AIA 304** around N40W40 starting on **21 June 2020 at 01:54 UT**. The brightening related to this eruption was observed by SDO/AIA 193 and the propagation is observed on COR2-A (Figure 4.27a). We used the result of the WSA-ENLIL+Cone model which deduced that the longitude of the CME is 41° west of the Sun-Earth line and the latitude is 2° south of the Sun-Earth line. Figure 4.27b-d shows the model of the propagating CME that is shown with the arrow. The initial speed of the CME was about 280 km/s and accelerated to about 370 km/s at 20 R_S; the speed of the CME at PSP observation reflects an initial acceleration and deceleration of the ICME. The angular width of the CME is 54°.

There was a slight enhancement in the magnetic field magnitude of **WIND** observation at **11:00 UT on 26 June 2020**, and we suspect that this is the flank of the ICME observed by PSP. This is shown in the overall plot shown in Figure 4.30. The Dst_{min} estimated at 01:00 UT on 27 June 2020, by the world data centre for geomagnetism was -13 nT, which signifies a mild geomagnetic storm.

Figure 4.26 - June 23, 2020, ICME plot and hodograms from PSP observation.

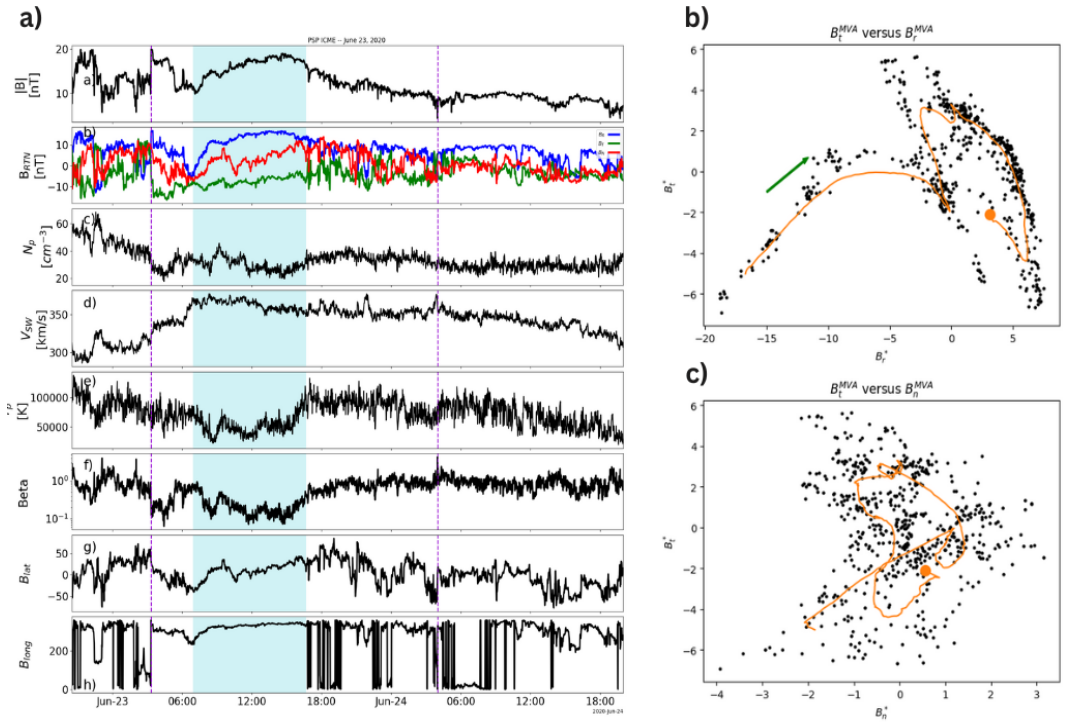

(a) Full plot of the ICME, (b) maximum variance plane and (c) minimum variance plane in the MVA coordinate system represented by the asterisk (*) sign.

SOURCE: Author.

Figure 4.27 - Remote Observation and Outward Propagation of the CME.

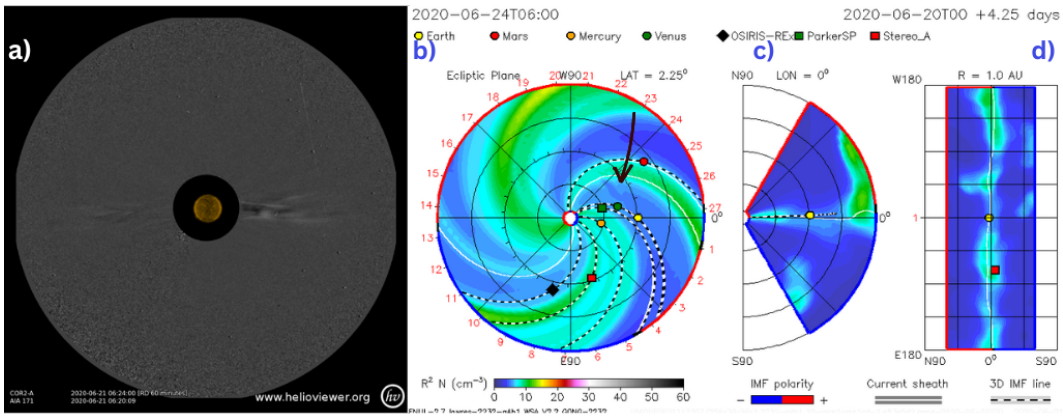

(a) STEREO-A/COR2 image (running difference of 60 min) showing the CME in white light. WSA-ENLIL+Cone model of the CME in the: (b) solar equatorial plane, the arrow points to the CME, (b) meridional plane at the Earth longitude, (c) 1 AU sphere in cylindrical projection. PSP is the green square and WIND is close to Earth (yellow circle).

SOURCE: Helioviewer and CCMC DONKI website Hughitt et al. (2008), Pizzo (2011).

4.4.1.2 Second eruption: June 25, 2020, ICME observed by PSP

On **25 June 2020 at 11:30 UT**, the shock of an ICME arrived at **PSP**, with the magnetic flux rope structure beginning at 16:00 the same day. PSP was located at 0.54 AU, 19.4° longitude from Earth's longitude, and 0.1° latitude away from Earth's latitude, 10.1° away from the CME's apex longitude, and 4.4° from the CME's apex latitude given in Heliocentric Earth Equatorial (HEEQ) coordinate. There was a smooth and clear rotation of the B_n component (Figure 4.28ab) of the FR and was further characterised by an increased N_p (Figure 4.28ac), decreasing V (Figure 4.28ad), reduced T_p (Figure 4.28ae) and reduced β (Figure 4.28af). It was slower than the previous ICME, with an average speed of 303 km/s.

At the application of the MVA, the orientation of the flux rope is **SEN** with an axis of 84° longitude and −19° latitude. It met all the MVA error criteria and the angle of rotation $\chi^2 = 139°$. The hodograms show the chirality of left-handedness.

The source of this ICME was linked to the same CME given in the previous research (MÖSTL et al., 2022) shown in Figure 4.29. The faint eruption was visible through **SDO/AIA 198** at about **13:00 UT on 22 June 2020** from the centre of the Earth-facing disk around S20W08. The application of the SSEF30 model shows that the CME apex direction was 16° west of the Sun-Earth line (MÖSTL et al., 2022), while our application of the WSA-ENLIL+cone model used a direction of 19.9°. The latitude was −8°, and the speed of the CME was 288 km/s with a half angle of 13°.

Connecting this event to the **WIND** spacecraft results located near Earth results in an ICME that arrived at **03:10 on 27 June 2020**. This is in contrast with the ICME that occurred on 30 June 2020, which was the event that Möstl et al. (2022) linked with the PSP observation. As seen in (Figure 4.28b), the flux rope has been deformed, but there the rotation of the B_n component persisted. At the application of MVA, the rotation is also observable in the hodogram created from the magnetic field components in the minimum variance plane (Figure 4.28d). A lower Dst_{min} was estimated at 04:00 UT on 28 June 2020 which was -18 nT. This also signifies a mild geomagnetic storm.

The MVA results, from WIND measurements in GSE coordinates, result in a flux rope orientation of **SWN**. The flux rope axis is 127° longitude and −17° latitude. The orientation is the same as that of the PSP result if the PSP observation is changed to the WIND coordinate system (RTN to GSE).

Figure 4.28 - ICME plots and hodograms of June 25 (PSP in RTN coordinates) and June 27, 2020 (WIND in GSE coordinates) observations.

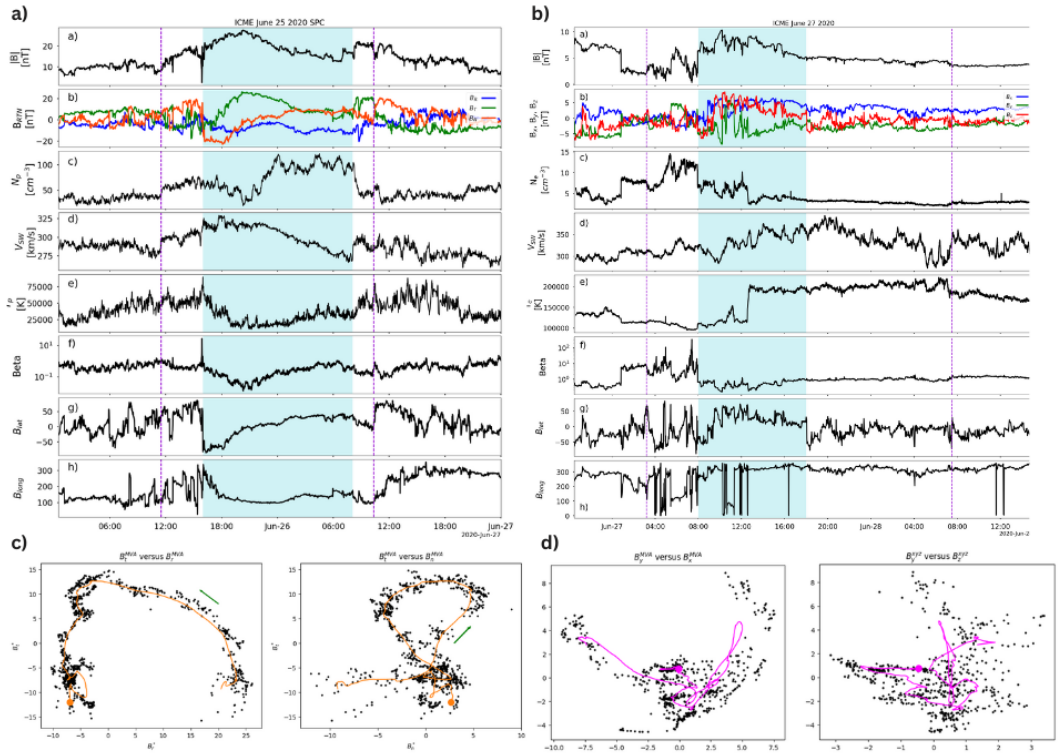

(a) PSP, (b) WIND. Hodograms of (c) maximum and minimum variance plane (PSP), (d) maximum and minimum variance plane (WIND), in MVA coordinate system.

SOURCE: Author.

Figure 4.29 - STEREO-A/COR2 image and WSA-ENLIL+Cone model of the CME in solar equatorial plane, meridional plane and cylindrical projection.

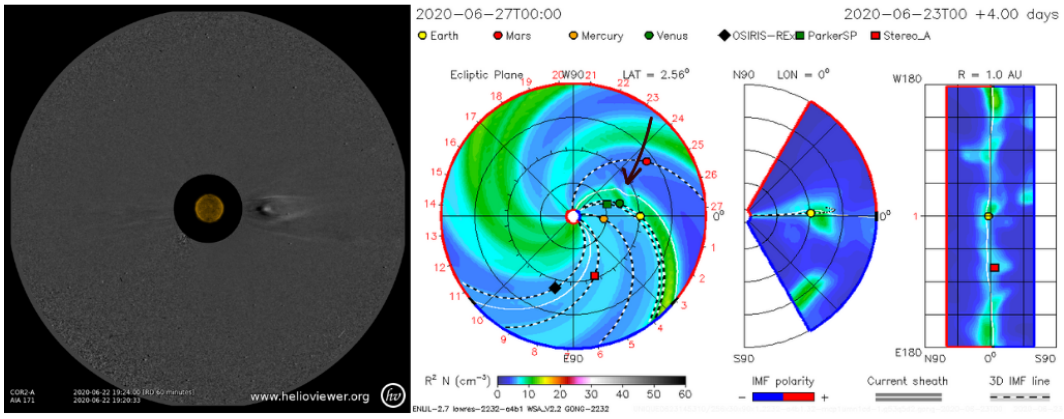

Note: arrow points to the CME. PSP is a green square and WIND is near the yellow circle.

SOURCE: Helioviewer and CCMC DONKI website Hughitt et al. (2008), Pizzo (2011).

4.4.1.3 Third eruption: June 27, 2020, ICME observed by PSP

The last of the eruption of the linked June ICME events was that which was observed by WIND on 30 June 2020 at 01:12. The author linked this event to the second eruption observed by PSP (June 25, 2020 event), but with close observation, this appears to be incorrect.

Based on our observation, the event in question can be attributed to the third eruption observed by PSP on 27 June 2020 at 12:00, located at 0.55 AU, longitude 20.8° and latitude 0.1° away from Earth's longitude and latitude and given in HEEQ. The shape of their magnetic field magnitude appears similar, but there appears to be no deformed FR, such that their orientations were not deduced nor compared. The possibility of PSP and WIND observing similar events throughout this WINDow is due to the small longitudinal separation between the two spacecraft which is approximately 20°. WIND spacecraft will most likely miss an ICME observed by PSP during this period if the event's direction is to the west of PSP, and PSP only observed the flank or it was a very narrow ICME.

Figure 4.30 shows the three ICMEs simultaneously observed at PSP linked to WIND spacecraft. A visual study of the magnitude of B observed by PSP and WIND shows that they exhibit a high degree of similarity. The peaks and distribution of the magnetic field data appear to be similar; while the B_{max} have reduced by over 10 nT, this can be explained to be caused by magnetic erosion as the ICME propagates. The variation of B components B_x, B_r and B_y, B_t can not be directly compared because they are measured in different coordinate systems and there is no smooth rotation embedded in them. Nonetheless, a Dst_{min} value of -12 nT was estimated at 05:00 UT on July 1, 2020.

The first CME (green), called ICME1 has the highest speed of all the 3 observed by PSP, and it agrees with what is seen in the WIND observation in that it has moved closer to ICME2 (blue). ICME3 (red) with a higher speed than ICME2 in PSP observation is also seen to have moved farther from ICME2 when capture at WIND.

Finally, this ICMEs linkages is currently a hypothesis that requires further scientific investigation to confirm their interconnectivity.

Figure 4.30 - The 3 ICMEs observed in June 2020 by PSP in RTN coordinates and WIND in GSE coordinates.

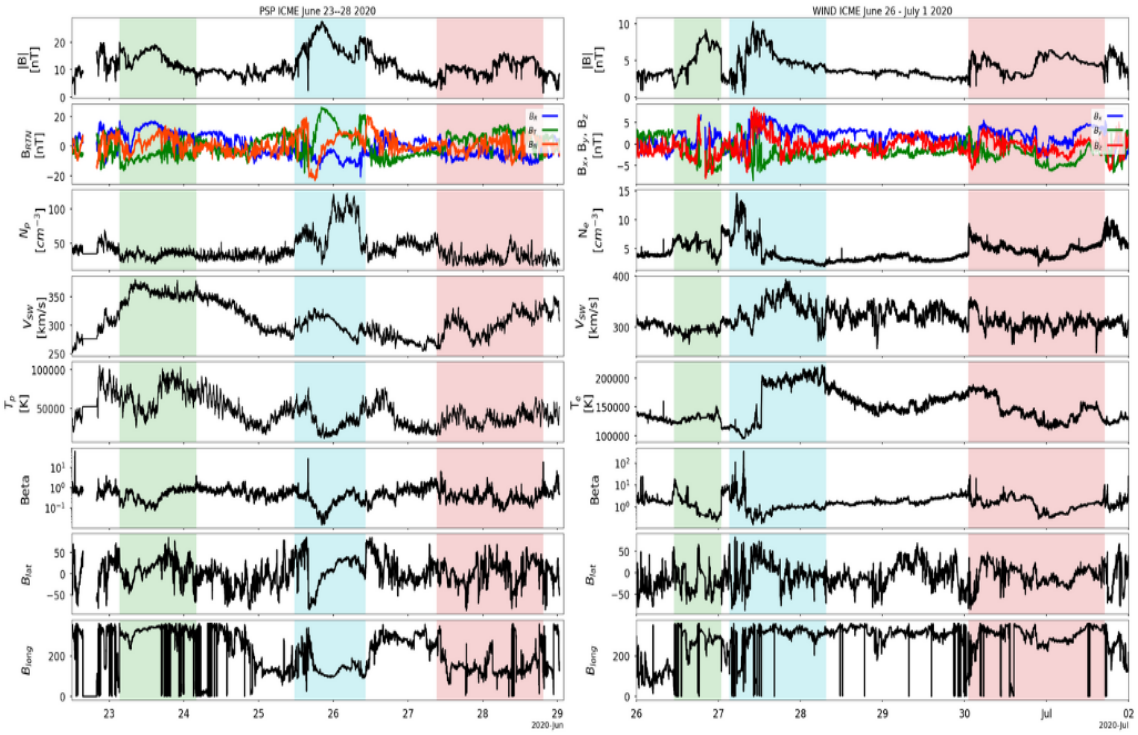

Left: PSP observations. Right: WIND observations. ICME1 is enclosed in green, ICME2 in blue and ICME3 in red.

SOURCE: Author.

4.5 Summary of derived flux rope parameters

The numbering of the events listed in Table 4.6 below corresponds to Table 4.3, so both can be combined to present the complete overview of the events from the eruption conditions on the Sun, to the estimated characteristics in situ. The Tables present 11 of the 44 identified magnetic clouds in the interplanetary medium. For the seven multi-point events observed in situ, presented in the Tables, the *criterion* is to connect spacecrafts that observe the same event at less than 40° longitudinal separation.

Table 4.6 contains 11 single and multi-spacecraft events. When we include the seven additional observations of some of the MCs, by other spacecraft (STA & WIND), we have a total of 18 events that were fully analysed. Event #6b observed by WIND on December 2, 2020, was not duly analysed because WIND observed the magnetic cloud at its flank, such that the flux rope properties are almost indistinguishable.

Thus, the flux rope parameters are labelled "not applicable" (NA). The events that are not Earthward do not have their Dst_{min} determined and are also marked NA. For event #4, the flux rope was complex and some of the derived flux rope parameters are considered to be inaccurate, so the results are not displayed in the Table.

Also, the plots of some of the listed events in Table 4.6 are presented in the Appendix. Event # 1 observed by PSP on May 28, 2020, is Figure A.2, and Event # 5 observed by PSP on September 13, 2020, is shown in Figure A.3. Event # 6 observed by both PSP and WIND from December 1–4, 2020 is shown in Figure A.4 and A.5 respectively. In Figure A.5, it can be observed more vividly why the magnetic cloud properties are tagged "NA" due to their poor quality.

Table 4.6 - The results of the analysis of the magnetic structure of the flux rope in situ.

#	MC Date-Time			Magnetic Flux Rope (MFR) Parameters											
	Start Time [UTC]	End Time [UTC]	S/C	$(\phi_{axis}, \theta_{axis})$	FR Type^{+}	Chirality	λ_2/λ_3	P_{Rosa}	p	L-angle [°]	Dst_{min} [nT]	B_{max} [nT]	V_{avg} [km/s]	V_{exp} [km/s]	R_{MC} [AU]
1	28-05-2020 09:00	28-05-2020 15:00	PSP	(71°, 260°)	WNE	RH	7.8	13.1	0.14	15	NA	46.8	284	9.2	0.04
2	23-06-2020 06:55	23-06-2020 17:00	PSP	(339°, −36°)	SWN	RH	4.5	10.0	0.18	-54	-13	16.8	322	8.4	0.07
	26-06-2020 18:00	27-06-2020 00:50	WIND	(125°, 13°)	NWS	LH	4.8	12.4	0.16	26	-13	9.2	294	-0.5	0.05
3	25-06-2020 16:00	26-06-2020 05:50	PSP	(84°, −19°)	SEN	LH	6.6	7.2	0.20	66	-18	27.7	303	26	0.12
	27-06-2020 08:00	27-06-2020 18:00	WIND	(127°, −17°)	SWN	RH	4.3	6.5	0.26	-1	-18	10.3	328	-30	0.08
4	28-06-2020 09:20	28-06-2020 17:00	PSP	(280°, 24°)	SEN	LH	8.0	9.2	0.17	-30	-12	13.2	323	10	0.06
	30-06-2020 20:48	01-07-2020 16:10	WIND	(297°, 17°)	SWN	RH	2.0	5.1	0.18	NA	-12	6.4	306	NA	NA
5	12-09-2020 12:30	12-09-2020 20:40	PSP	(208°, 69°)	SWN	RH	2.4	3.6*	0.27	43	NA	18.8	309	9	0.07
6	01-12-2020 03:17	01-12-2020 11:42	PSP	(125°, −28°)	ENW	LH	7.7	12.9	0.14	-31	-11	38.8	657	89	0.13
	02-12-2020 17:00	02-12-2020 21:00	WIND	NA	NA	NA	NA	NA	NA	NA	-11	NA	NA	NA	NA
7	27-08-2021 12:15	28-08-2021 10:45	WIND	(263°, 26°)	SEN/ WSE	LH	13.2	15.7	0.09	19	-82	16.0	400	-47	0.22
8	26-09-2021 13:40	26-09-2021 20:30	PSP	(226°, −56°)	WSE	LH	7.4	6.5	0.18	45	-2	15.4	408	13	0.07
	27-09-2021 04:30	27-09-2021 13:00	STA	(167°, −34°)	WSE	LH	3.2	8.15	0.18	59	-2	12.5	409	21	0.08
9	26-09-2021 22:50	27-09-2021 12:40	PSP	(186°, −18°)	ENW	LH	1.2*	1.5*	0.20	-58	-2	16.1	353	27	0.12
	27-09-2021 14:55	28-09-2021 03:30	STA	(62°, 15°)	SEN/ENW	LH	2.5	6.4	0.2	-15	-2	11.2	358	13	0.08
10	09-11-2021 18:41	10-11-2021 05:00	PSP	(81°, 13°)	SWN	RH	6.7	11.9	0.15	40	NA	59.6	400	56	0.10
11	05-07-2022 04:00	05-07-2022 12:00	PSP	(265°, 9°)	SEN	LH	4.4	9.0	0.19	-8	-82	21.8	346	-8	0.07
	07-07-2022 11:30	08-07-2022 04:20	WIND	(98°, 44°)	SWN	RH	25.5	18.1	0.07	4	-82	22.6	366	-2	0.15

$^{+}$ FR types are inferred from RTN coordinates in PSP/STA measurements and GSE coordinates in WIND measurements.

* Values that do not fall within the criteria for MVA application reliability.

L-R: Start and end time of the MC, observing spacecraft, FR axis from MVA, in-situ flux rope type, handedness of the FR, MVA error criteria (intermediate-to-minimum eigenvalue ratio, (BOTHMER; SCHWENN, 1998)), MVA metric (OLIVEIRA et al., 2020), impact parameter $\langle|B_{min}|\rangle/\langle B\rangle$ (spacecraft crossing distance from FR axis), location angle (spacecraft crossing distance from the ICME nose, and minimum Dst index value, MC maximum magnetic field, MC average velocity, MC expansion velocity and MC radius. NA means not applicable.

SOURCE: Author.

Figure 4.31 - Average linear velocities of the coronal mass ejections on the Sun, at PSP and STEREO-A or WIND.

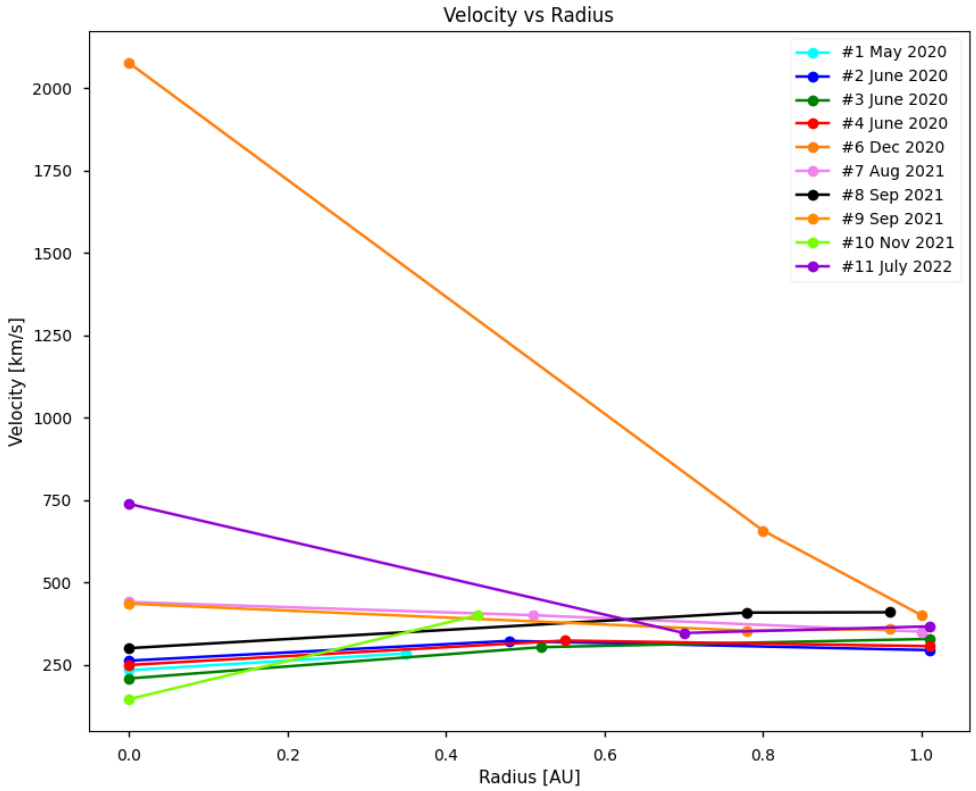

Note: Circle markers represent near the Sun (estimated from SOHO/LASCO observation), mid-way and near-Earth observations. Event #5 was skipped because we could not connect the in-situ observation to its remote observation counterpart.

SOURCE: Author.

Figure 4.31 shows the relationship between the velocities of the MCs with respect to the point of observation. There are three points of measurement marked by circles. The first marker is on the Sun at ≈0 AU, the second is the mid-way observation by PSP, and the third marker is near Earth observed either by STEREO-A or WIND. It is observed that the starting velocities of the CMEs range widely from 145 km/s to 2077 km/s, mid-way velocities ranged from 284 km/s to 657 km/s, and final velocities near Earth ranged from 294 km/s to 409 km/s.

The event with the greatest deceleration, marked in orange is event #6. The V_{avg} of the MC was marked to be NA in Table 4.6 because there were no clear observable MC properties at the far-edge observation by WIND. Its initial velocity was about 2077 km/s, PSP that was about just 15° from its apex crossed the ICME at 657

km/s, while WIND observed its remnant travelling at the speed of 400 km/s. There were, however, two ICMEs observed around this window, and the preceding ICME could have contributed to this great deceleration. These events were extensively studied by Nieves-Chinchilla et al. (2022).

Another event that shows rapid deceleration is event #11 which had an initial linear speed of 738 km/s, reduced to 346 km/s and increased back to 366 km/s near Earth. The low velocity in the mid-observation of PSP can also be alluded to the spacecraft separation distance of 36° from the CME's apex, while the WIND observational position was only 2° away. There are other events shown in Figure 4.31 that appear to accelerate first and then decelerate such as events #2 and #4. The near-Earth observations of both events were also farther from the CME apex in comparison with the mid-way observations with higher velocity. Some others consistently accelerated even until arrival near Earth such as event #3, with velocities 208 km/s, 303 km/s and 328 km/s from Sun to Earth respectively. We could infer from these case events that the farther we move away from the apex of an ICME, the lower the linear speed observed.

Of the 11 single and multi-spacecraft observed MCs, we picked 5 events that the longitudinal separation between the two observing spacecrafts was less than 20° and made Figure 4.32 show the changes in the maximum magnetic field data from one spacecraft to the other. The longitudinal separation distance was limited so that the plot can highlight the radial evolution of B_{max} more.

Presented in Figure 4.33 is the rate of occurrence of the 8 different flux rope types. Bipolar flux ropes are seen to be more abundant in this pool of events in comparison with unipolar events, with the maximum occurring flux rope type being SWN, followed by the SEN type.

Figure 4.32 - In situ maximum magnetic field data PSP to WIND or STEREO-A.

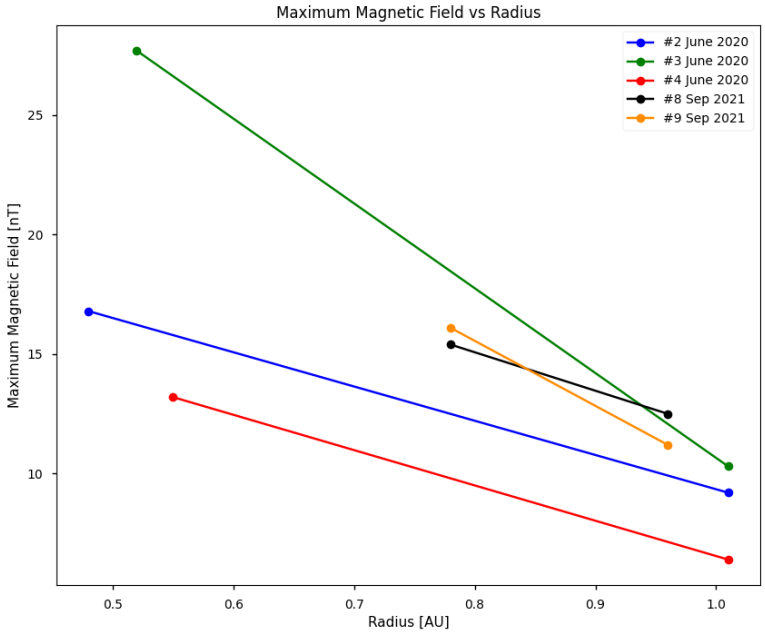

Note: Circle markers represent mid-way and near-Earth observations. Five events with longitudinal separation less than 20° were used in this plot.

SOURCE: Author.

Figure 4.33 - The rate of occurrence of the 8-flux rope types as measured by PSP, WIND and STEREO-A.

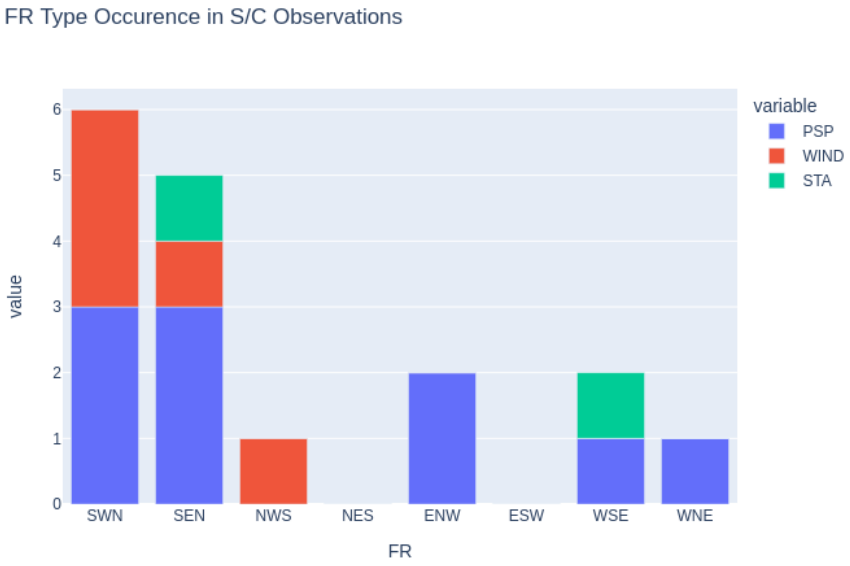

SOURCE: Author.

Finally, this work attempted to portray the relationship of the analysed magnetic cloud parameters with the radial distances. The parameters considered are plasma beta, density and temperature. The colour gradient in the Figures represents the longitudinal separation of the point of observation from the CME apex. This is done because it has been observed earlier that it has a negative relationship with measured magnetic field and velocity data (i.e. they increase as the longitudinal separation decreases), so it could impact other parameters. Figure 4.34 is a visualisation of the average density of the magnetic clouds against the radial distances in AU. It shows that, for the analysed MCs in this work, the density tends to reduce with increasing propagation distance as expected. The event with the highest density was observed close to the Sun (< 0.4 AU) and close to the CME apex.

Plasma beta, the ratio of plasma pressure to magnetic pressure has been noted to be less than one in magnetic clouds because magnetic pressure dominates over thermal pressure in clouds. In Figure 4.35, the relationship between beta and the distances of the analysed events appeared to be neutral. In Figure 4.36, there appears to be a slight positive correlation between the temperature of the MCs and the distances, as higher temperatures are observed for observations by WIND spacecraft near Earth for events measured close and far from their apex (LEWIS et al., 2020).

Figure 4.34 - Plot of the density of the MCs versus radial distances.

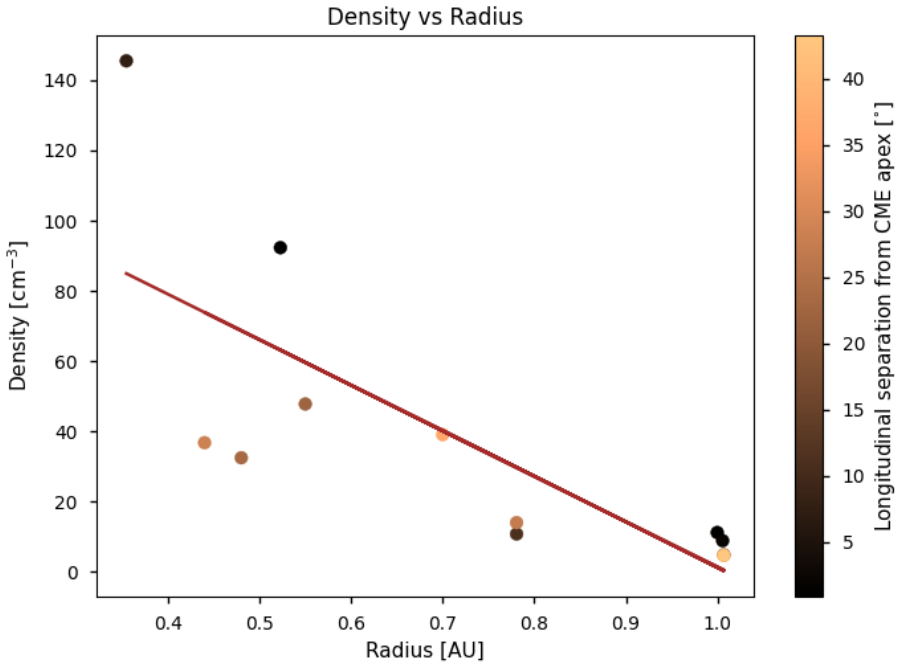

SOURCE: Author.

Figure 4.35 - Plot of plasma beta of the analysed MCs against radial distances of observation.

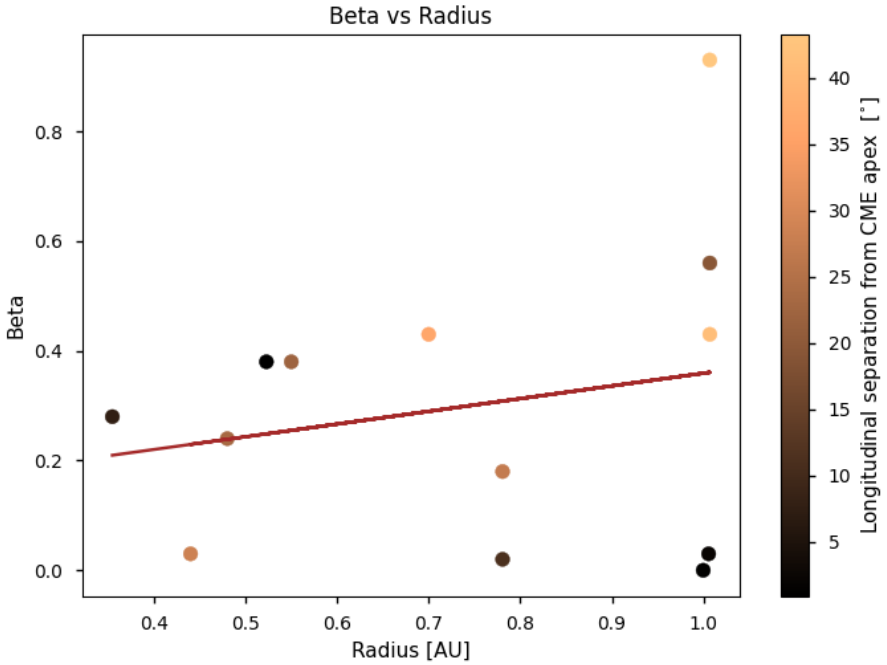

SOURCE: Author.

Figure 4.36 - Plot of the temperature of the analysed MCs against radial distances of observation.

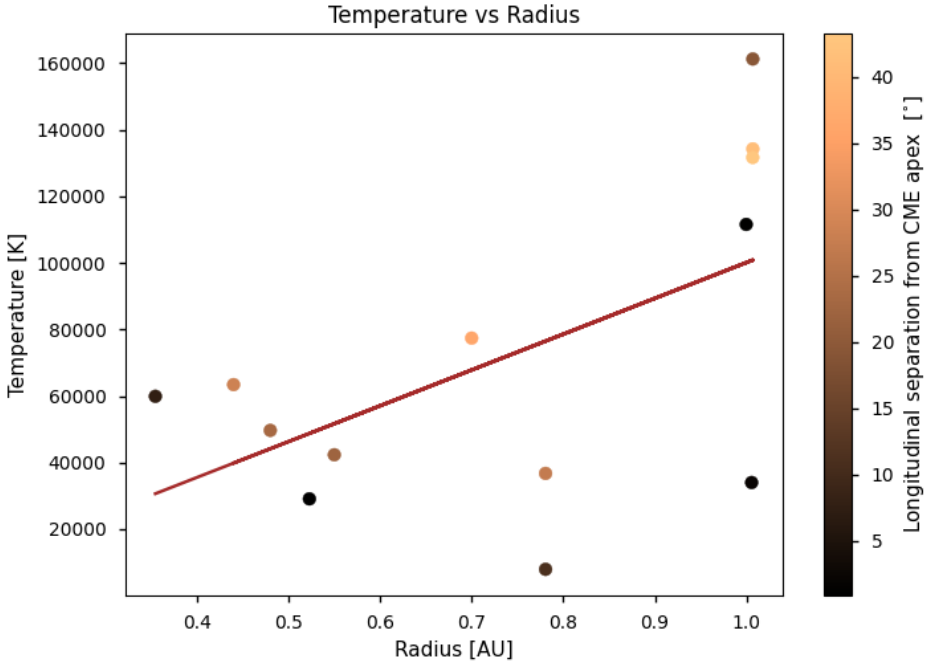

SOURCE: Author.

5 DISCUSSIONS

The first objective of this research is to **identify magnetic cloud structures** which are a subset of interplanetary coronal mass ejections with distinct characteristics. The three major characteristics used are enhanced magnetic field, rotation of the magnetic field component(s) and depression of plasma beta. Sometimes, we observe decreasing velocity in the r direction and depressed temperature. This was achieved by the visualization of the observational data from PSP from around its operational stage, November 2018 until September 2022. Through the time-series plot creates in combination with existing catalogues, we identified 54 ICMEs within this period, which was observed by PSP. There could have been more events listed, but there were a lot of data gaps when PSP is carrying out some operational manoeuvres which impairs the observation of the needed characteristics. Further study of the identified ICMEs shows that 44 contain magnetic cloud, which is 81% of the identified ICME. The year 2021 had the highest number of identified ICMEs (19 events) as well as the highest MC found in the ICMEs (16 events). Out of the 44 MCs, we studied and analysed 11 single and multi-spacecraft ICMEs (18 in total) that had good MC and data quality at PSP and other interplanetary spacecraft.

This percentage of MC occurrence in this study cannot be considered a good representation of the occurrence of MCs within ICMEs because of the rate of poor data and the period studies spanned the tail end of solar cycle 24 and the beginning of cycle 25. Previous research has statistically shown that about 30% of ICMEs contain MCs, about 15% in the solar minimum and up to 70% in the solar maximum (GOSLING, 1990; RICHARDSON; CANE, 2010; CANE; RICHARDSON, 2003). Also, the identification of magnetic clouds can be complicated sometimes as the idealised rotation are not often observed.

Secondly, we aimed to **determine the orientation of the magnetic clouds using the minimum variance analysis** method. Out of the total events studied in detail, only two of them did not meet the error criteria needed to show that the MVA results are reliable. These are marked with an asterisk in the summary values provided in Table 4.6. In the remaining events that were analysed, MVA gave us a good representation of the orientation of the axis of the flux rope which agrees with the deductions obtained from visual observation and served as an accurate input parameter for the force-free fitting. From the orientation deduced from the total of 17 MCs (Event #6b excluded), 10 are bipolar, especially of type SWN. Five are unipolar and two are considered to be bipolar or unipolar. Bipolar FRs are flux

ropes with low inclination to the ecliptic. i.e., almost parallel to the ecliptic plane. The hodogram created also shows that most of the events analysed are left-handed.

Furthermore, another goal was to be able to **fit the magnetic field data and its spherical components with the Lundquist force-free model**. This is to validate the accuracy of the force-free model in being able to reconstruct the magnetic field profiles of the MCs using input parameters such as B_{max}, constant α and parameters derived from the MVA application: θ, ϕ, and H. The results presented in this thesis agree with previous research such that the force-free model could imitate the variational direction of θ and ϕ but does not match well with the magnetic field magnitude. This is because it generates an ideal magnetic field profile that is symmetric, but due to complex processes in the interplanetary medium such as magnetic erosion and compression, that causes the apex to tilt away from the centre.

To achieve the last objective of **studying the evolution of the MCs**, we used magnetic field and plasma data from spacecraft located around 1 AU such as PSP, SolO, WIND, ACE, and STEREO-A. We used the data to evaluate the changes that have occurred in these parameters when observed across different radial, longitudinal and latitudinal separations. There are changes in every observable parameter of the ICMEs as they propagate due to the interaction of ICMEs with other ICMEs and the solar wind as they propagate, which causes the FR structures to expand, compress, get deformed or completely erode. The velocities can even increase by an order >100 km/s, as observed in the September 2021 events where the linear speed of CME1 increased from 264 km/s when observed by SOHO/LASCO to 444 km/s when observed in situ as ICME1 at PSP. Also, it is inferred that longitudinal separation from the apex of the ICME correlates to a decrease in velocity observed. This agrees with previous research that have shown that the leading edge of ICMEs moves faster than its trailing edge which results in the radial expansion of ICMEs. The magnetic field, temperature, and density are also observed to decrease from mid-way observation to observations closer to Earth. Finally, the density of the analysed MCs is noted to decrease with increasing distances of observations from the Sun while the temperature gradually increased with increased radial distance. Plasma beta, on the other hand, appears to be relatively constant across 0 – 1 AU in the events presented in this work.

6 CONCLUSIONS

CMEs that are connected from imaging on the Sun to multipoints observations in the interplanetary medium are the most valuable for understanding the global configuration of coronal mass ejections. Only a few research have been used to explore Parker Solar Probe observation of ICMEs in conjunction with other spacecrafts within 1 AU. We take it a step further by exploring a particular ICME event that was observed by 5 spacecrafts in situ: Solar Orbiter, Parker Solar Probe, STEREO-A, ACE and WIND, and was also captured by multiple coronagraphs.

Events that are observed by single spacecraft in situ and connected with coronagraph images are also important as they help us understand the relationship between CME morphology and other characteristics observed remotely and flux rope properties observed in situ such as their orientation, speed, shock, etc. These are used to validate and improve CME evolution models.

Using the available set of plasma and magnetic field data of the Parker Solar Probe spacecraft from 2018 to 2022, we identified 54 ICMEs between 0.1 and 1 AU. In addition, we used magnetic field and plasma data from WIND, ACE and STEREO data and coronagraph images from SOHO, STEREO-A and SDO. All these are used to identify the presence of magnetic clouds in the interplanetary medium, investigate their orientation and present the evolution of their major properties between the Sun and 1 AU.

Here are the conclusions drawn from the analyses of 17 single and multispacecraft observations of flux ropes in the interplanetary medium.

a) ICMEs maintain the orientation of their magnetic field structure across radial distances. For example, the B_n component of ICME1 in the September 2021 event is southward and northward in ICME2 for all observations at the five different spacecrafts.

b) The B_n component of the interacting September 2021 ICME also retained the same orientation across longitudinal distances, e.g, on opposite sides of the ICME which suggests a fair interaction across the longitudinal distance of the ICME. However, due to the direction of the apex of interacting ICMEs, the overlapping of the ICMEs was more at one end than the other.

c) The re-analysis of an "extremely long" June 2020 ICME (travelled for 7 days from the Sun observation to WIND at 300 km/s) studied in Möstl

et al. (2022) shows that there is an alternate explanation for the unusual length of propagation period. There was another ICME observed at PSP about 1 day after that could have impacted WIND spacecraft as well.

d) For interacting ICMEs such as those observed in September 2021, it is observed that deformation of the embedded FR structure begins at the ICME behind travelling at a faster speed and catching up with the ICME ahead.

e) Density and temperature of the magnetic clouds analysed correlated negatively and positively with radial distances respectively, while plasma beta values were relatively constant across the radial distances.

f) The Lundquist model shows that the force-free fitting is still generally capable of reproducing the angular variation of the magnetic field magnitude of the magnetic clouds. With new models, considering other parameters such as non-force-free, expansion, and magnetic erosion, the solar physics community will be able to predict magnetic cloud structures more accurately in time.

g) The use of minimum variance analysis (MVA) to deduce the axis of the flux rope orientation has proven to be a useful tool as the events met all the necessary error criteria used to determine the reliability of MVA with exception of two events.

The September 2021 event is a rare event that presented the opportunity to understand the evolution of interacting CMEs when observed at multiple points in the interplanetary medium that are separated radially, longitudinally and latitudinally. Unfortunately, the structures of the ICMEs became complicated due to their interaction with each other. With the solar cycle 25 gradually reaching its peak, earlier than predicted and the presence of multiple heliospheric missions, there will be more favourable windows to study magnetic clouds. These will help us to further understand the configuration, and evolution of multi-point ICMEs, and also understand their impact on other processes in the interplanetary medium. With more interacting ICMEs being observed, we can also understand more how these changes are reflected in their magnetic field, density, velocity and temperature parameters.

REFERENCES

AL-HADDAD, N.; NIEVES-CHINCHILLA, T.; SAVANI, N.; MÖSTL, C.; MARUBASHI, K.; HIDALGO, M.; ROUSSEV, I.; POEDTS, S.; FARRUGIA, C. J. Magnetic field configuration models and reconstruction methods for interplanetary coronal mass ejections. **Solar Physics**, v. 284, n. 1, p. 129–149, 2013. 14, 15

AL-HADDAD, N.; ROUSSEV, I. I.; MÖSTL, C.; JACOBS, C.; LUGAZ, N.; POEDTS, S.; FARRUGIA, C. J. On the internal structure of the magnetic field in magnetic clouds and interplanetary coronal mass ejections: Writhe versus twist. **The Astrophysical Journal Letters**, v. 738, n. 2, p. L18, 2011. 14, 29

BALE, S. et al. The fields instrument suite for solar probe plus. **Space Science Reviews**, v. 204, n. 1, p. 49–82, 2016. 45, 46, 55

BHATTACHARJEE, D.; SUBRAMANIAN, P.; BOTHMER, V.; NIEVES-CHINCHILLA, T.; VOURLIDAS, A. On modeling icme cross-sections as static mhd columns. **arXiv preprint arXiv:2203.06996**, 2022. 18

BITTENCOURT, J. A. **Fundamentals of plasma physics**. [S.l.: s.n.], 2004. 19, 20

BOTHMER, V.; SCHWENN, R. The structure and origin of magnetic clouds in the solar wind. **Annales Geophysicae**, v. 16, n. 1, p. 1–24, 1998. Available from: <https://angeo.copernicus.org/articles/16/1/1998/>. 17, 29, 37, 38, 41, 69, 70, 71, 74, 123

BRUECKNER, G. et al. The large angle spectroscopic coronagraph (lasco) visible light coronal imaging and spectroscopy. **The SOHO Mission**, p. 357–402, 1995. 52

BURLAGA, L. Magnetic clouds and force-free fields with constant alpha. **Journal of Geophysical Research: Space Physics**, v. 93, n. A7, p. 7217–7224, 1988. 17, 21, 27, 29

BURLAGA, L.; KLEIN, L. **Magnetic clouds in the solar wind**. [S.l.], 1980. 2, 5, 11, 13

BURLAGA, L.; SITTLER, E.; MARIANI, F.; SCHWENN, a. R. Magnetic loop behind an interplanetary shock: voyager, helios, and imp 8 observations. **Journal of Geophysical Research: Space Physics**, v. 86, n. A8, p. 6673–6684, 1981. 2, 10, 13, 14, 29, 88

BURLAGA, L. F.; BEHANNON, K. Magnetic clouds: voyager observations between 2 and 4 au. **Solar Physics**, v. 81, n. 1, p. 181–192, 1982. 13, 32, 44, 74

CANE, H.; RICHARDSON, I. Interplanetary coronal mass ejections in the near-earth solar wind during 1996–2002. **Journal of Geophysical Research: Space Physics**, v. 108, n. A4, 2003. 10, 129

CASE, A. W. et al. The solar probe cup on the parker solar probe. **The Astrophysical Journal Supplement Series**, v. 246, n. 2, p. 43, 2020. 47

CID, C.; HIDALGO, M.; NIEVES-CHINCHILLA, T.; SEQUEIROS, J.; VIÑAS, A. Plasma and magnetic field inside magnetic clouds: a global study. **Solar Physics**, v. 207, n. 1, p. 187–198, 2002. 15

COLANINNO, R. C. **Investigation of the forces that govern the three-dimensional propagation and expansion of coronal mass ejections from sun to earth**. [S.l.: s.n.], 2012. 7

DASSO, S.; MANDRINI, C.; DÉMOULIN, P.; FARRUGIA, C. J. Magnetic helicity analysis of an interplanetary twisted flux tube. **Journal of Geophysical Research: Space Physics**, v. 108, n. A10, 2003. 15

DASSO, S.; MANDRINI, C. H.; DÉMOULIN, P.; LUONI, M. L.; GULISANO, A. M. Large scale mhd properties of interplanetary magnetic clouds. **Advances in Space Research**, v. 35, n. 5, p. 711–724, 2005. 14

DAVIES, E. E.; FORSYTH, R. J.; GOOD, S. W.; KILPUA, E. K. On the radial and longitudinal variation of a magnetic cloud: ace, wind, artemis and juno observations. **Solar Physics**, v. 295, n. 11, p. 1–25, 2020. 11, 71

DOMINGO, V.; FLECK, B.; POLAND, A. I. The soho mission: an overview. **Solar Physics**, v. 162, p. 1–37, 1995. 52

DUNBAR, B. **Parker solar probe: humanity's first visit to a star**. 2021. Available from: <https://www.nasa.gov/content/goddard/parker-solar-probe-humanity-s-first-visit-to-a-star>. 45

ECHER, E.; GONZALEZ, W. Geoeffectiveness of interplanetary shocks, magnetic clouds, sector boundary crossings and their combined occurrence. **Geophysical Research Letters**, v. 31, n. 9, 2004. 1

EDDY, J. A. **The sun, the earth, and near-earth space: a guide to the sun-earth system**. [S.l.: s.n.], 2009. 5

EYLES, C. et al. The heliospheric imagers onboard the stereo mission. **Solar Physics**, v. 254, p. 387–445, 2009. 52

FARRUGIA, C. J.; BURLAGA, L.; OSHEROVICH, V.; RICHARDSON, I.; FREEMAN, M.; LEPPING, R.; LAZARUS, A. A study of an expanding interplanetary magnetic cloud and its interaction with the earth's magnetosphere: The interplanetary aspect. **Journal of Geophysical Research: Space Physics**, v. 98, n. A5, p. 7621–7632, 1993. 11, 86, 91

FARRUGIA, C. J.; OSHEROVICH, V.; BURLAGA, L. Magnetic flux rope versus the spheromak as models for interplanetary magnetic clouds. **Journal of Geophysical Research: Space Physics**, v. 100, n. A7, p. 12293–12306, 1995. 17

FARRUGIA, C. J. et al. A uniform-twist magnetic flux rope in the solar wind. v. 471, n. 1, p. 745–748, 1999. 14, 17

GALVIN, A. B. et al. The plasma and suprathermal ion composition (plastic) investigation on the stereo observatories. **The STEREO Mission**, p. 437–486, 2008. 52

GIESELER, J. et al. Solar-mach: an open-source tool to analyze solar magnetic connection configurations. **arXiv preprint arXiv:2210.00819**, 2022. 87, 99, 100

GOLDSTEIN, H. On the field configuration in magnetic clouds. **JPL Solar Wind Five**, 1983. 14, 16, 17, 18, 21, 26

GONZÁLEZ, A. O.; JUNIOR, O. M.; MENCONI, V. E.; DOMINGUES, M. O. Daubechies wavelet coefficients: a tool to study interplanetary magnetic field fluctuations. **Geofísica internacional**, v. 53, n. 2, p. 101–115, 2014. 9

GONZALEZ, W.; JOSELYN, J.-A.; KAMIDE, Y.; KROEHL, H. W.; ROSTOKER, G.; TSURUTANI, B.; VASYLIUNAS, V. What is a geomagnetic storm? **Journal of Geophysical Research: Space Physics**, v. 99, n. A4, p. 5771–5792, 1994. 8

GONZALEZ, W. D.; TSURUTANI, B. T. Criteria of interplanetary parameters causing intense magnetic storms (dst<- 100 nt). **Planetary and Space Science**, v. 35, n. 9, p. 1101–1109, 1987. 1

GONZáLEZ, A. O. **Identification and characterization of interplanetary magnetic clouds.** [S.l.]: Instituto Nacional de Pesquisas Espaciais- INPE. Tese (Doutorado), 2013. 40 p. Available at: http://www.inpe.br/posgraduacao/ges/arquivos/teses/tese_arian_ojeda_gonzaleza_2013.pdf. 21

GOOD, S.; KILPUA, E.; LAMOURY, A.; FORSYTH, R.; EASTWOOD, J.; MÖSTL, C. Self-similarity of icme flux ropes: observations by radially aligned spacecraft in the inner heliosphere. **Journal of Geophysical Research: Space Physics**, v. 124, n. 7, p. 4960–4982, 2019. 71

GOPALSWAMY, N.; YASHIRO, S.; MICHALEK, G.; STENBORG, G.; VOURLIDAS, A.; FREELAND, S.; HOWARD, R. The soho/lasco cme catalog. **Earth, Moon, and Planets**, v. 104, p. 295–313, 2009. 5, 91, 97, 98, 109

GOSLING, J.; ASBRIDGE, J.; BAME, S.; FELDMAN, W. Solar wind speed variations: 1962–1974. **Journal of Geophysical Research**, v. 81, n. 28, p. 5061–5070, 1976. 1

GOSLING, J.; HANSEN, R.; BAME, S. Solar wind speed distributions: 1962–1970. **Journal of Geophysical Research**, v. 76, n. 7, p. 1811–1815, 1971. 1

GOSLING, J.; PIZZO, V.; BAME, S. J. Anomalously low proton temperatures in the solar wind following interplanetary shock waves—evidence for magnetic bottles? **Journal of Geophysical Research**, v. 78, n. 13, p. 2001–2009, 1973. 12

GOSLING, J.; RILEY, P.; MCCOMAS, D.; PIZZO, V. Overexpanding coronal mass ejections at high heliographic latitudes: Observations and simulations. **Journal of Geophysical Research: Space Physics**, v. 103, n. A2, p. 1941–1954, 1998. 9

GOSLING, J. T. Coronal mass ejections and magnetic flux ropes in interplanetary space. **Physics of magnetic flux ropes**, v. 58, p. 343–364, 1990. 10, 129

GULISANO, A. M.; DASSO, S.; MANDRINI, C. H.; DÉMOULIN, P. Estimation of the bias of the minimum variance technique in the determination of magnetic clouds global quantities and orientation. **Advances in Space Research**, v. 40, n. 12, p. 1881–1890, 2007. 16, 33, 34, 69

HEYNER, D. et al. The bepicolombo planetary magnetometer mpo-mag: what can we learn from the hermean magnetic field? **Space Science Reviews**, v. 217, p. 1–71, 2021. 55

HIDALGO, M.; NIEVES-CHINCHILLA, T.; CID, C. Elliptical cross-section model for the magnetic topology of magnetic clouds. **Geophysical Research Letters**, v. 29, n. 13, p. 15–1, 2002. 14, 15

HOWARD, R. A.; MOSES, J.; VOURLIDAS, A.; NEWMARK, J.; SOCKER, D. G.; PLUNKETT, S. P.; KORENDYKE, C. M.; COOK, J.; HURLEY, A.; DAVILA, J. et al. Sun earth connection coronal and heliospheric investigation (secchi). **The STEREO Mission**, p. 67–115, 2008. 51

HU, Q.; SONNERUP, B. U. Reconstruction of magnetic flux ropes in the solar wind. **Geophysical Research Letters**, v. 28, n. 3, p. 467–470, 2001. 14

_____. Reconstruction of magnetic clouds in the solar wind: orientations and configurations. **Journal of Geophysical Research: Space Physics**, v. 107, n. A7, p. SSH–10, 2002. 14

HU, Q.; ZHENG, J.; CHEN, Y.; ROUX, J. le; ZHAO, L. Automated detection of small-scale magnetic flux ropes in the solar wind: first results from the wind spacecraft measurements. **The Astrophysical Journal Supplement Series**, v. 239, n. 1, p. 12, 2018. 38

HUGHITT, V.; IRELAND, J.; LYNCH, M.; SCHMEIDEL, P.; DIMITOGLOU, G.; MÜELLER, D.; FLECK, B. Helioviewer: a web 2.0 tool for visualizing heterogeneous heliophysics data. **AGU Fall Meeting Abstracts**, 12 2008. 81, 117, 119

IVANOV, K.; HARSHILADZE, A. Dynamics of hydromagnetic clouds from powerful solar flares. **Solar Physics**, v. 92, n. 1, p. 351–362, 1984. 22

JANVIER, M.; DÉMOULIN, P.; DASSO, S. Global axis shape of magnetic clouds deduced from the distribution of their local axis orientation. **Astronomy & Astrophysics**, v. 556, p. A50, 2013. 75

KAMIDE, Y.; CHIAN, A. **Handbook of the solar-terrestrial environment**. [S.l.: s.n.], 1990. 7, 8, 11

KARNEY, C.; DEAKIN, R. E. Fw bessel (1825): the calculation of longitude and latitude from geodesic measurements. **Astronomische Nachrichten**, v. 331, n. 8, p. 852–861, 2010. 35

KASPER, J. C. et al. Solar wind electrons alphas and protons (sweap) investigation: design of the solar wind and coronal plasma instrument suite for solar probe plus. **Space Science Reviews**, v. 204, n. 1, p. 131–186, 2016. 45, 47, 55

KILPUA, E.; BALOGH, A.; STEIGER, R. V.; LIU, Y. Geoeffective properties of solar transients and stream interaction regions. **Space Science Reviews**, v. 212, n. 3-4, p. 1271–1314, 2017. 1

KILPUA, E.; KOSKINEN, H. E.; PULKKINEN, T. I. Coronal mass ejections and their sheath regions in interplanetary space. **Living Reviews in Solar Physics**, v. 14, n. 1, p. 1–83, 2017. 9, 11, 17

KLEIN, L.; BURLAGA, L. Interplanetary magnetic clouds at 1 au. **Journal of Geophysical Research: Space Physics**, v. 87, n. A2, p. 613–624, 1982. 2, 14, 32, 33, 37, 38, 69

LEMEN, J. R. et al. The atmospheric imaging assembly (aia) on the solar dynamics observatory (sdo). **Solar Physics**, v. 275, p. 17–40, 2012. 54, 80

LEPPING, R.; BEHANNON, K. Magnetic field directional discontinuities: 1. minimum variance errors. **Journal of Geophysical Research: Space Physics**, v. 85, n. A9, p. 4695–4703, 1980. 33, 34, 35, 68, 85

LEPPING, R.; BERDICHEVSKY, D. Interplanetary magnetic clouds: Sources, properties, modeling, and geomagnetic relationship. **Recent Research Developments in Geophysics**, p. 77–96, 2000. 12

LEPPING, R.; BERDICHEVSKY, D.; WU, C.-C.; SZABO, A.; NAROCK, T.; MARIANI, F.; LAZARUS, A.; QUIVERS, A. A summary of wind magnetic clouds for years 1995-2003: model-fitted parameters, associated errors and classifications. **Annales Geophysicae**, v. 24, n. 1, p. 215–245, 2006. 13, 71

LEPPING, R.; JONES, J.; BURLAGA, L. Magnetic field structure of interplanetary magnetic clouds at 1 au. **Journal of Geophysical Research: Space Physics**, v. 95, n. A8, p. 11957–11965, 1990. 14, 15, 28, 29, 71

LEPPING, R. et al. The wind magnetic field investigation. **Space Science Reviews**, v. 71, p. 207–229, 1995. 49

LEWIS, G. N.; RANDALL, M.; PITZER, K. S.; BREWER, L. **Thermodynamics**. [S.l.: s.n.], 2020. 127

LIN, R. Particle acceleration in solar flares and coronal mass ejections. In: SYMPOSIUM INTERNATIONAL ASTRONOMICAL UNION, 195., 2000. **Proceedings...** [S.l.], 2000. p. 15–25. 1

LINDSAY, G.; LUHMANN, J.; RUSSELL, C.; GOSLING, J. Relationships between coronal mass ejection speeds from coronagraph images and interplanetary characteristics of associated interplanetary coronal mass ejections. **Journal of Geophysical Research: Space Physics**, v. 104, n. A6, p. 12515–12523, 1999. 9

LIVI, R. et al. The solar probe analyzer-ions on parker solar probe. 2020. 47

LUHMANN, J. et al. Stereo impact investigation goals, measurements, and data products overview. **The STEREO Mission**, p. 117–184, 2008. 52

LUNDQUIST, S. Magnetohydrostatic fields. **Arkiv för Fysik**, v. 2, p. 361–365, 1950. 21, 27, 71

MARUBASHI, K. Structure of the interplanetary magnetic clouds and their solar origins. **Advances in Space Research**, v. 6, n. 6, p. 335–338, 1986. 2, 39

MCCOMAS, D.; GOSLING, J.; WINTERHALTER, D.; SMITH, E. Interplanetary magnetic field draping about fast coronal mass ejecta in the outer heliosphere. **Journal of Geophysical Research: Space Physics**, v. 93, n. A4, p. 2519–2526, 1988. 53

MCCOMAS, D. et al. Integrated science investigation of the sun (isis): design of the energetic particle investigation. **Space Science Reviews**, v. 204, n. 1, p. 187–256, 2016. 45, 46

MOLDWIN, M.; FORD, S.; LEPPING, R.; SLAVIN, J.; SZABO, A. Small-scale magnetic flux ropes in the solar wind. **Geophysical research letters**, v. 27, n. 1, p. 57–60, 2000. 38

MONTAGNON, E.; BUDNIK, F.; CASALE, M.; FUENTE, S. de la; MARTINEZ, S.; MURAKAMI, G.; OGAWA, M.; SEKI, T.; STEIGER, C.; YAMASHITA, M. Bepicolombo ground segment and mission operations. **Space Science Reviews**, v. 217, p. 1–23, 2021. 55

MONTGOMERY, D.; MATTHAEUS, W. H. Anisotropic modal energy transfer in interstellar turbulence. **The Astrophysical Journal**, v. 447, p. 706, 1995. 44

MÖSTL, C. et al. Multipoint interplanetary coronal mass ejections observed with solar orbiter, bepicolombo, parker solar probe, wind, and stereo-a. **The Astrophysical Journal Letters**, v. 924, n. 1, p. L6, 2022. 59, 115, 118, 132

MULLIGAN, T.; RUSSELL, C.; LUHMANN, J. Solar cycle evolution of the structure of magnetic clouds in the inner heliosphere. **Geophysical Research Letters**, v. 25, n. 15, p. 2959–2962, 1998. 38, 41

NATIONAL AERONAUTICS AND SPACE ADMINISTATION (NASA); EUROPEAN SPACE AGENCY (ESA); SOLAR AND HELIOSPHERIC OBSERVATORY (SOHO) MISSION. **SOHO Gallery**. July 2020. Available from: <https://soho.nascom.nasa.gov/gallery/Spacecraft/SOHOUpper.html>. Access in: 24 March 2023. 52

NATIONAL AERONAUTICS AND SPACE ADMINISTRATION (NASA). PARKER SOLAR PROBE (PSP) MISSION. **Parker Solar Probe instruments**. 2018. Available from: <http://parkersolarprobe.jhuapl.edu/Spacecraft/index.php#Instruments>. Access in: 24 March 2023. 46, 47

NATIONAL AERONAUTICS AND SPACE ADMINISTRATION (NASA). STEREO MISSION. **STEREO spacecraft & instruments**. February 2021. Available from: <https://www.nasa.gov/mission_pages/stereo/spacecraft/index.html>. Access in: 24 March 2023. 51

NIEVES-CHINCHILLA, T.; HIDALGO, M.; SEQUEIROS, J. Magnetic clouds observed at 1 au during the period 2000–2003. **Solar Physics**, v. 232, n. 1, p. 105–126, 2005. 14, 15

NIEVES-CHINCHILLA, T.; JIAN, L. K.; BALMACEDA, L.; VOURLIDAS, A.; SANTOS, L. F. dos; SZABO, A. Unraveling the internal magnetic field structure of the earth-directed interplanetary coronal mass ejections during 1995–2015. **Solar Physics**, v. 294, n. 7, p. 1–46, 2019. 40, 43, 85, 103

NIEVES-CHINCHILLA, T.; LINTON, M.; HIDALGO, M.; VOURLIDAS, A. Elliptic-cylindrical analytical flux rope model for magnetic clouds. **The Astrophysical Journal**, v. 861, n. 2, p. 139, 2018. 42

NIEVES-CHINCHILLA, T.; LINTON, M.; HIDALGO, M. A.; VOURLIDAS, A.; SAVANI, N. P.; SZABO, A.; FARRUGIA, C.; YU, W. A circular-cylindrical flux-rope analytical model for magnetic clouds. **The Astrophysical Journal**, v. 823, n. 1, p. 27, 2016. 14, 42

NIEVES-CHINCHILLA, T. et al. Direct first parker solar probe observation of the interaction of two successive interplanetary coronal mass ejections in 2020 november. **The Astrophysical Journal**, v. 930, n. 1, p. 88, 2022. 125

NIEVES-CHINCHILLA, T.; VOURLIDAS, A.; RAYMOND, J. C.; LINTON, M.; AL-HADDAD, N.; SAVANI, N.; SZABO, A.; HIDALGO, M. A. Understanding the internal magnetic field configurations of icmes using more than 20 years of wind observations. **Solar Physics**, v. 293, n. 2, p. 1–31, 2018. 37, 38, 85

ODSTRCIL, D.; VANDAS, M.; PIZZO, V. J.; MACNEICE, P. Numerical Simulation of Interacting Magnetic Flux Ropes. **AIP Conference Proceedings**, v. 679, n. 1, p. 699–702, 09 2003. Available from: <https://doi.org/10.1063/1.1618690>. 14

OGILVIE, K. et al. Swe, a comprehensive plasma instrument for the wind spacecraft. **Space Science Reviews**, v. 71, p. 55–77, 1995. 50

OJEDA-GONZÁLEZ, A.; GONZÁLEZ-AVILÉS, J.; LUZ, V.; SANTOS, L. Magnetohydrodynamic wave modes influenced by displacement current. **Revista Brasileira de Ensino de Física**, v. 43, 2021. 19

OJEDA-GONZÁLEZ, A.; KLAUSNER, V.; MENDES, O.; DOMINGUES, M. O.; PRESTES, A. Characterization of the complex ejecta measured in situ on 19–22 march 2001 by six different methods. **Solar Physics**, v. 292, p. 1–23, 2017. 71

OLIVEIRA, R. A. R.; OLIVEIRA, M. W. da S.; OJEDA-GONZÁLEZ, A.; LUZ, V. D. L. New metric for minimum variance analysis validation in the study of interplanetary magnetic clouds. **Solar Physics**, v. 295, n. 3, p. 1–16, 2020. 32, 34, 36, 37, 85, 123

OLIVEIRA, R. A. R.; OLIVEIRA, M. W. da S.; OJEDA-GONZÁLEZ, A.; PILLAT, V. G.; ECHER, E.; NIEVES-CHINCHILLA, T. Resolving the ambiguity of a magnetic cloud's orientation caused by minimum variance analysis comparing it with a force-free model. **Solar Physics**, v. 296, n. 12, p. 1–35, 2021. 29, 34, 35, 37, 68, 71, 72

PAL, S.; DASH, S.; NANDY, D. Flux erosion of magnetic clouds by reconnection with the sun's open flux. **Geophysical Research Letters**, v. 47, n. 8, p. e2019GL086372, 2020. 86, 91, 105

PALMERIO, E.; KILPUA, E. K.; MÖSTL, C.; BOTHMER, V.; JAMES, A. W.; GREEN, L. M.; ISAVNIN, A.; DAVIES, J. A.; HARRISON, R. A. Coronal

magnetic structure of earthbound cmes and in situ comparison. **Space Weather**, v. 16, n. 5, p. 442–460, 2018. 40

PESNELL, W. D.; THOMPSON, B. J.; CHAMBERLIN, P. **The solar dynamics observatory (SDO)**. [S.l.: s.n.], 2012. 54, 80

PETUKHOVA, A.; PETUKHOV, I.; PETUKHOV, S. Theory of the formation of forbush decrease in a magnetic cloud: dependence of forbush decrease characteristics on magnetic cloud parameters. **The Astrophysical Journal**, v. 880, n. 1, p. 17, 2019. 11

PIZZO, V. Wang-sheeley-arge-enlil cone model transitions to operations. **Space Weather**, v. 9, n. 3, 2011. 82, 97, 109, 117, 119

PRIEST, E. The equilibrium of magnetic flux ropes (tutorial lecture). **Physics of Magnetic Flux Ropes**, v. 58, p. 1–22, 1990. 16

RICHARDSON, I. G.; CANE, H. V. Near-earth interplanetary coronal mass ejections during solar cycle 23 (1996–2009): catalog and summary of properties. **Solar Physics**, v. 264, n. 1, p. 189–237, 2010. 10, 129

RICKETT, B.; SIME, D.; JR, N. S.; CROCKETT, W.; TOUSEY, R. High-latitude observations of solar wind streams and coronal holes. **Journal of Geophysical Research**, v. 81, n. 22, p. 3845–3850, 1976. 1

RILEY, P.; LINKER, J.; MIKIĆ, Z.; ODSTRCIL, D.; ZURBUCHEN, T.; LARIO, D.; LEPPING, R. P. Using an mhd simulation to interpret the global context of a coronal mass ejection observed by two spacecraft. **Journal of Geophysical Research: Space Physics**, v. 108, n. A7, 2003. 15

ROCKENBACH, M. et al. Global muon detector network used for space weather applications. **Space Science Reviews**, v. 182, n. 1, p. 1–18, 2014. 10

RODRIGUEZ, L. et al. Typical profiles and distributions of plasma and magnetic field parameters in magnetic clouds at 1 au. **Solar Physics**, v. 291, n. 7, p. 2145–2163, 2016. 12

ROMASHETS, E.; VANDAS, M. Force-free field inside a toroidal magnetic cloud. **Geophysical Research Letters**, v. 30, n. 20, 2003. 14

SAITO, Y.; SAUVAUD, J.; HIRAHARA, M.; BARABASH, S.; DELCOURT, D.; TAKASHIMA, T.; ASAMURA, K.; BEPICOLOMBO, M.; TEAM, M. et al.

Scientific objectives and instrumentation of mercury plasma particle experiment (mppe) onboard mmo. **Planetary and Space Science**, v. 58, n. 1-2, p. 182–200, 2010. 55

SAVIAN, J. F.; SILVA, M. R. d.; LAGO, A. D.; ECHER, E.; VIEIRA, L. E. A.; MUNAKATA, K.; GONZALEZ, W. D.; SCHUCH, N. J. Forbush decreases on november 6-12, 2004 observed by the muon detector network. **Revista Brasileira de Geofísica**, v. 25, p. 169–173, 2007. 10

SCHERRER, P. H.; SCHOU, J.; BUSH, R.; KOSOVICHEV, A.; BOGART, R.; HOEKSEMA, J.; LIU, Y.; DUVALL, T.; ZHAO, J.; TITLE, A. et al. The helioseismic and magnetic imager (hmi) investigation for the solar dynamics observatory (sdo). **Solar Physics**, v. 275, p. 207–227, 2012. 54

SHI, C.; ZHAO, J.; HUANG, J.; WANG, T.; WU, D.; CHEN, Y.; HU, Q.; KASPER, J. C.; BALE, S. D. Parker solar probe observations of alfvénic waves and ion-cyclotron waves in a small-scale flux rope. **The Astrophysical Journal Letters**, v. 908, n. 1, p. L19, 2021. 34, 38

SISCOE, G.; SUEY, R. Significance criteria for variance matrix applications. **Journal of Geophysical Research**, v. 77, n. 7, p. 1321–1322, 1972. 34, 68, 85

SMITH, C. W.; L'HEUREUX, J.; NESS, N. F.; ACUNA, M. H.; BURLAGA, L. F.; SCHEIFELE, J. The ace magnetic fields experiment. **Space Science Reviews**, v. 86, p. 613–632, 1998. 53

SOLAR TERRESTRIAL RELATIONS OBSERVATORY (STEREO). **Two for the Show**. 2011. Available from: <https://stereo.gsfc.nasa.gov/gallery/item.shtml?id=stereoimages&iid=160>. Access in: 24 March 2023. 6

SOLAR WIND ELECTRONS ALPHAS AND PROTONS (SWEAP) SCIENCE TEAM. **User guide for parker solar probe SWEAP investigation data products**. Jan. 2020. Available from: <https://cdaweb.gsfc.nasa.gov/pub/data/psp/sweap/sweap_data_user_guide.pdf>. Access in: 24 March 2023. 49

SONNERUP, B. Ö.; CAHILL, J. L. Magnetopause structure and attitude from explorer 12 observations. **Journal of Geophysical Research**, v. 72, n. 1, p. 171–183, 1967. 29, 32

SONNERUP, B. U.; SCHEIBLE, M. Minimum and maximum variance analysis. **Analysis methods for multi-spacecraft data**, v. 1, p. 185–220, 1998. 29, 34

STASIEWICZ, K.; GUSTAFSSON, G. Alfvén waves and structures: what can we learn with multipoint measurements on cluster-ii. In: CLUSTER WORKSHOP MULTISCALE/MULTIPOINT PLASMA MEASUREMENTS, 2., 2000. **Proceedings...** [S.l.], 2000. p. 177. 44

STONE, E.; FRANDSEN, A.; MEWALDT, R.; CHRISTIAN, E.; MARGOLIES, D.; ORMES, J.; SNOW, F. The advanced composition explorer. **Space Science Reviews**, v. 86, n. 1-4, p. 1, 1998. 53

TELLONI, D.; BRUNO, R.; D'AMICIS, R.; PIETROPAOLO, E.; CARBONE, V. Wavelet analysis as a tool to localize magnetic and cross-helicity events in the solar wind. **The Astrophysical Journal**, v. 751, n. 1, p. 19, 2012. 44

THOMPSON, W. T. et al. The cor1 inner coronagraph for stereo-secchi. In: SPIE. **Innovative Telescopes and Instrumentation for Solar Astrophysics**. [S.l.], 2003. v. 4853, p. 1–11. 52

TOUSEY, R.; RYCROFT, M.; KUNCORN, S. **The solar corona-space research XIII**. [S.l.]: Akademie-Verlag Berlin, 1973. 1

TSURUTANI, B. T.; GOLDSTEIN, B. E.; SMITH, E. J.; GONZALEZ, W. D.; TANG, F.; AKASOFU, S. I.; ANDERSON, R. R. The interplanetary and solar causes of geomagnetic activity. **Planetary and space science**, v. 38, n. 1, p. 109–126, 1990. 9

UNIVERSITY OF WASHINGTON. **The WIND spacecraft experiment**. November 2011. Available from: <https://earthweb.ess.washington.edu/space/SpaceExp/WIND/>. Access in: 24 March 2023. 50

VANDAS, M.; FISCHER, S.; PELANT, P.; GERANIOS, A. Spheroidal models of magnetic clouds and their comparison with spacecraft measurements. **Journal of Geophysical Research: Space Physics**, v. 98, n. A7, p. 11467–11475, 1993. 14

VANDAS, M.; GERANIOS, A.; ROMASHETS, E. On expansion of magnetic clouds in the solar wind. **Astrophysics and Space Sciences Transactions**, v. 5, n. 1, p. 35–38, 2009. 17

VANDAS, M.; ODSTRČIL, D.; WATARI, S. Three-dimensional mhd simulation of a loop-like magnetic cloud in the solar wind. **Journal of Geophysical Research: Space Physics**, v. 107, n. A9, p. SSH–2, 2002. 14

VIEIRA, L. R.; ECHER, E.; SCHUCH, N. J.; SILVA, M. R. D.; KEMMERICH, N.; STEKEL, T. R. C. Correlations between cosmic ray decreases and forward shock parameters in 2001. In: INTERNATIONAL CONGRESS OF THE BRAZILIAN GEOPHYSICAL SOCIETY, 11., 2009. **Proceedings...** [S.l.], 2009. p. 195. 11

VIRTANEN, P. et al. Scipy 1.0: fundamental algorithms for scientific computing in python. **Nature Methods**, v. 17, n. 3, p. 261–272, 2020. 73

VOURLIDAS, A.; BALMACEDA, L. A.; STENBORG, G.; LAGO, A. D. Multi-viewpoint coronal mass ejection catalog based on stereo cor2 observations. **The Astrophysical Journal**, v. 838, n. 2, p. 141, 2017. 6

VOURLIDAS, A. et al. The wide-field imager for solar probe plus (wispr). **Space Science Reviews**, v. 204, n. 1, p. 83–130, 2016. 5, 45, 47

VOURLIDAS, A.; WEBB, D. F. Streamer-blowout coronal mass ejections: their properties and relation to the coronal magnetic field structure. **The Astrophysical Journal**, v. 861, n. 2, p. 103, 2018. 7

WHITTLESEY, P. L. et al. The solar probe analyzers—electrons on the parker solar probe. **The Astrophysical Journal Supplement Series**, v. 246, n. 2, p. 74, 2020. 47

WIEGELMANN, T.; SAKURAI, T. Solar force-free magnetic fields. **Living Reviews in Solar Physics**, v. 18, n. 1, p. 1–67, 2021. 5

WOODS, T. N.; EPARVIER, F.; HOCK, R.; JONES, A.; WOODRASKA, D.; JUDGE, D.; DIDKOVSKY, L.; LEAN, J.; MARISKA, J.; WARREN, H. et al. Extreme ultraviolet variability experiment (eve) on the solar dynamics observatory (sdo): overview of science objectives, instrument design, data products, and model developments. **Solar Physics**, v. 275, p. 115–143, 2012. 54

WÜLSER, J.-P. et al. Euvi: the stereo-secchi extreme ultraviolet imager. In: SPIE. **Telescopes and instrumentation for solar astrophysics**. [S.l.], 2004. v. 5171, p. 111–122. 52

ZHAO, L.-L. et al. Identification of magnetic flux ropes from parker solar probe observations during the first encounter. **The Astrophysical Journal Supplement Series**, v. 246, n. 2, p. 26, 2020. 44

ZHAO, X.; HOEKSEMA, J. Central axial field direction in magnetic clouds and its relation to southward interplanetary magnetic field events and dependence on disappearing solar filaments. **Journal of Geophysical Research: Space Physics**, v. 103, n. A2, p. 2077–2083, 1998. 70

ZURBUCHEN, T.; RICHARDSON, I. In-situ solar wind and mag-4301 netic field signatures of interplanetary coronal mass ejections. **Space Science**, v. 4302, p. 1–3, 2006. 83

APPENDIX A - PLOTS OF THE EVENTS ANALYSED IN THIS WORK

This section contains some of the plots of events that were created in this research but not included in the main text, some of these are presented in Table 4.6. The ICMEs are enclosed in violet lines and the magnetic clouds are enclosed in a blue rectangular shade.

Figure A.1 - November 11, 2018 event observed by Parker Solar Probe spacecraft.

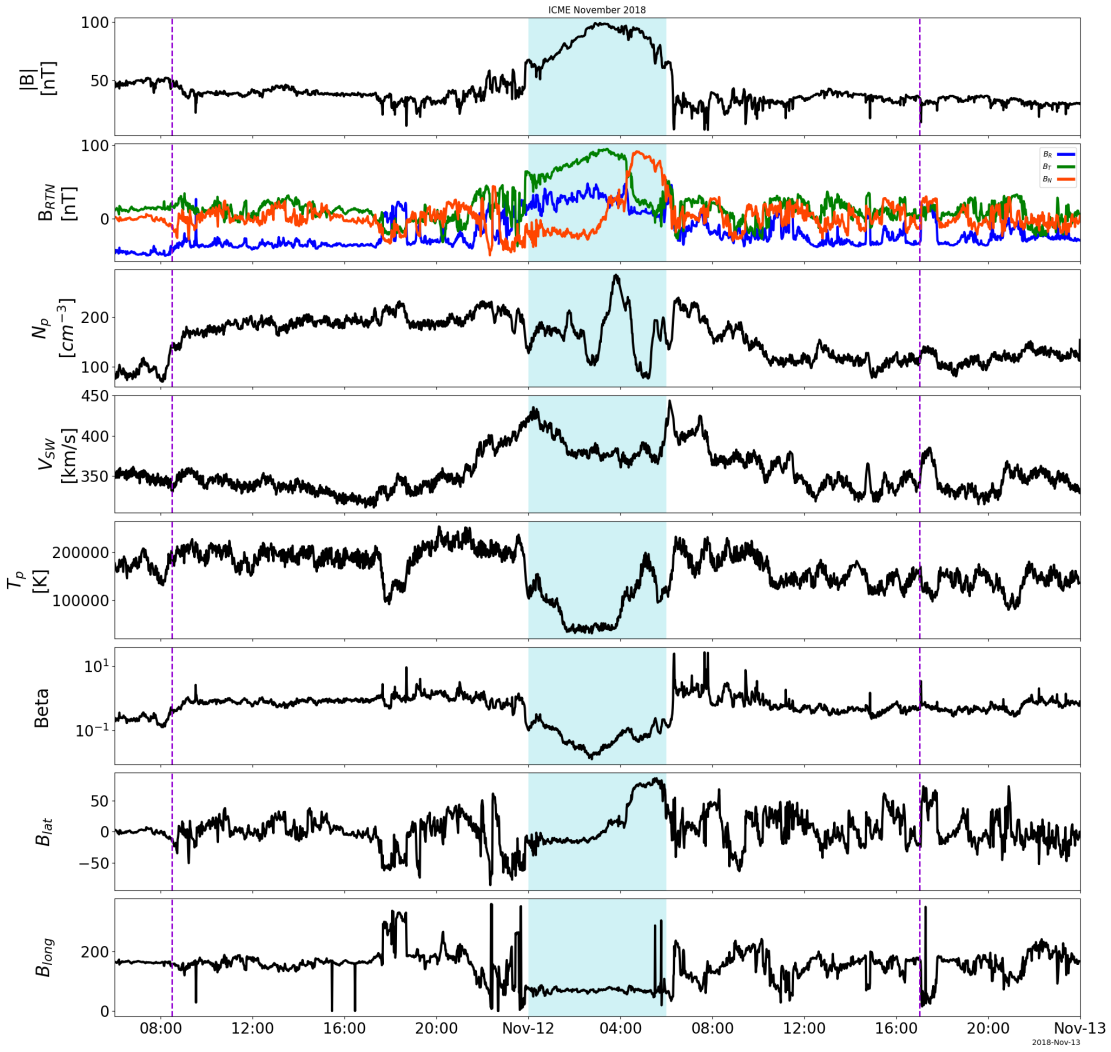

SOURCE: Author.

Figure A.2 - May 28, 2020 event observed by Parker Solar Probe spacecraft.

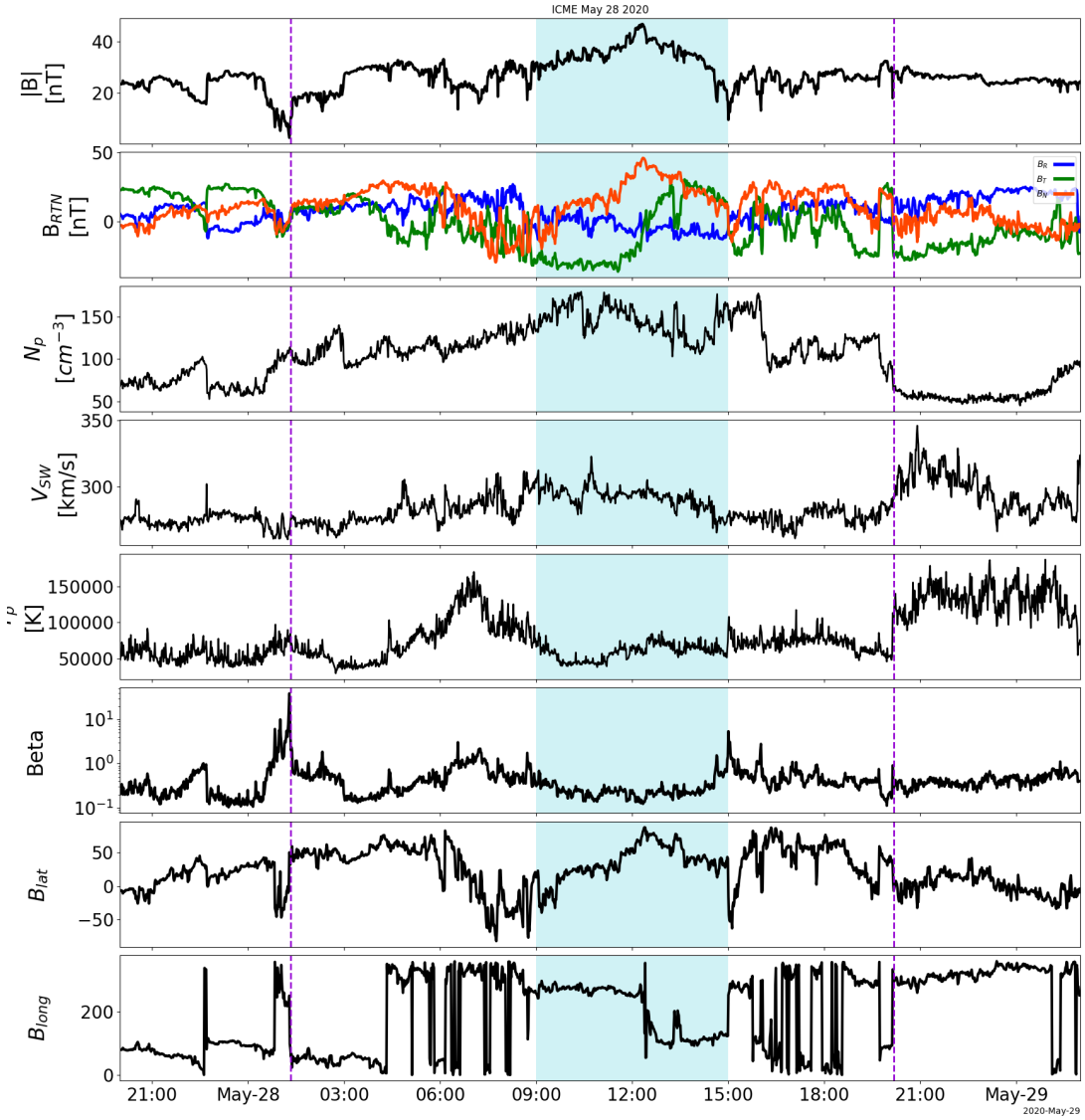

SOURCE: Author.

Figure A.3 - September 12, 2020 event observed by Parker Solar Probe spacecraft.

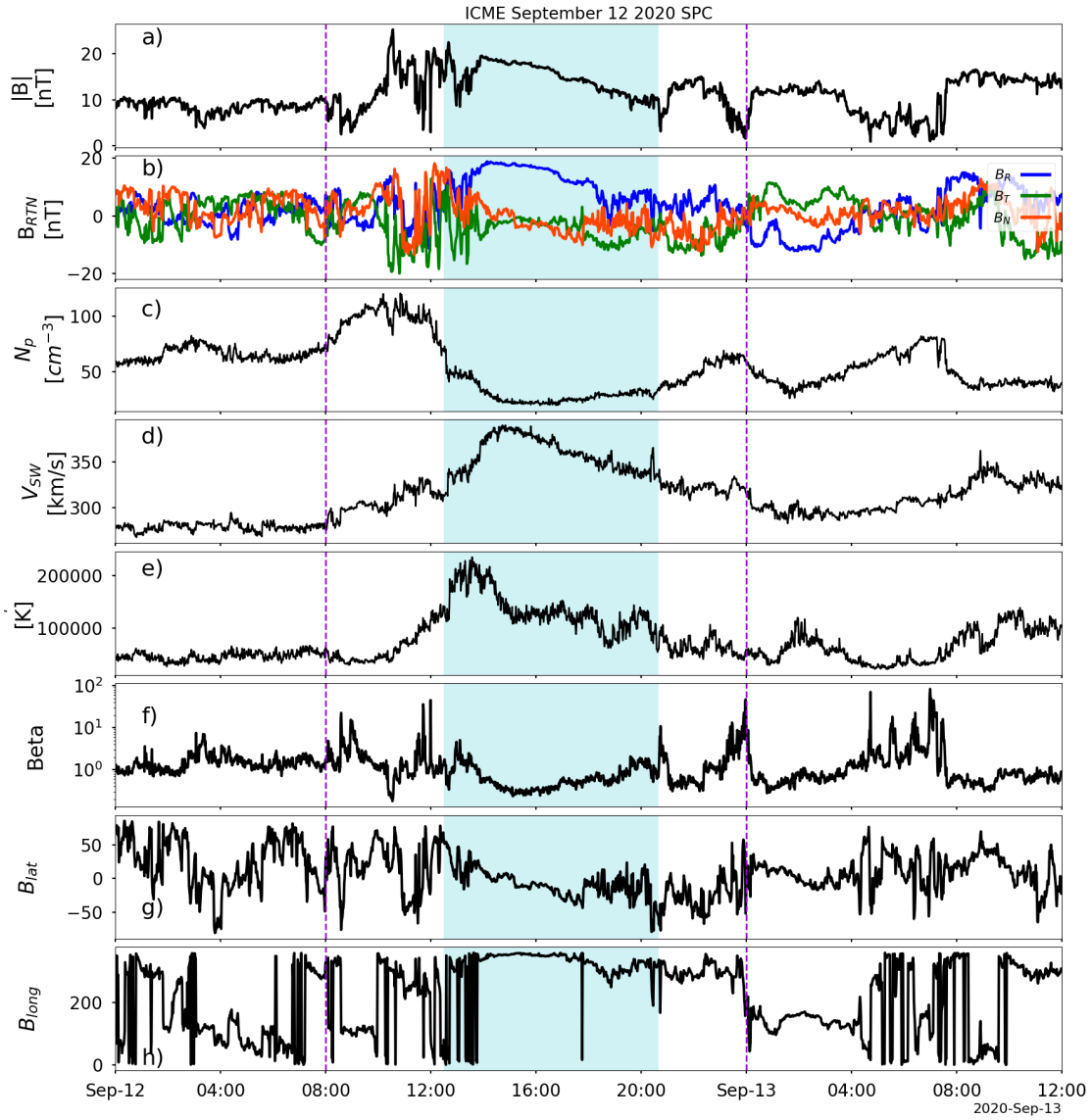

SOURCE: Author.

Figure A.4 - December 2, 2020 event observed by Parker Solar Probe spacecraft.

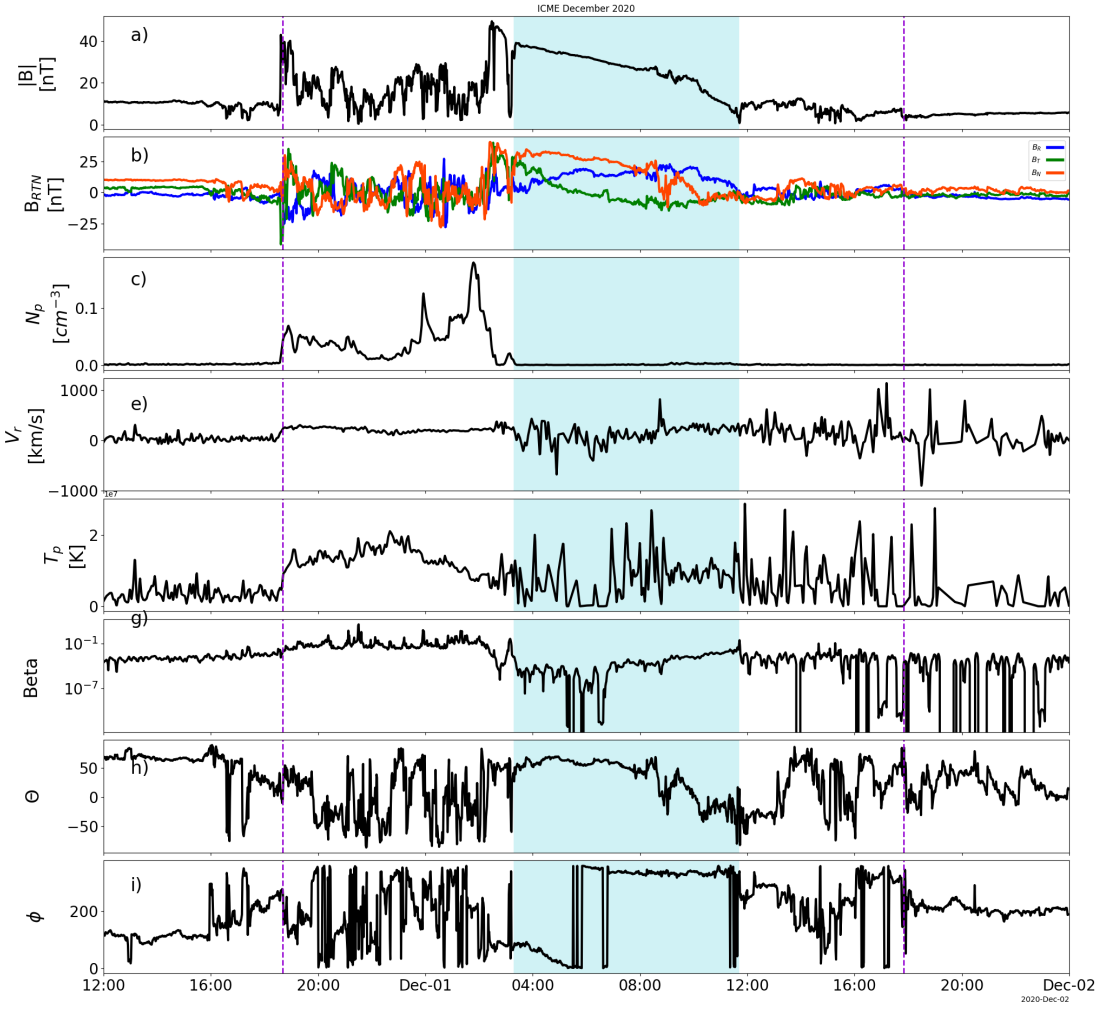

SOURCE: Author.

Figure A.5 - December 2, 2020 event observed by WIND spacecraft.

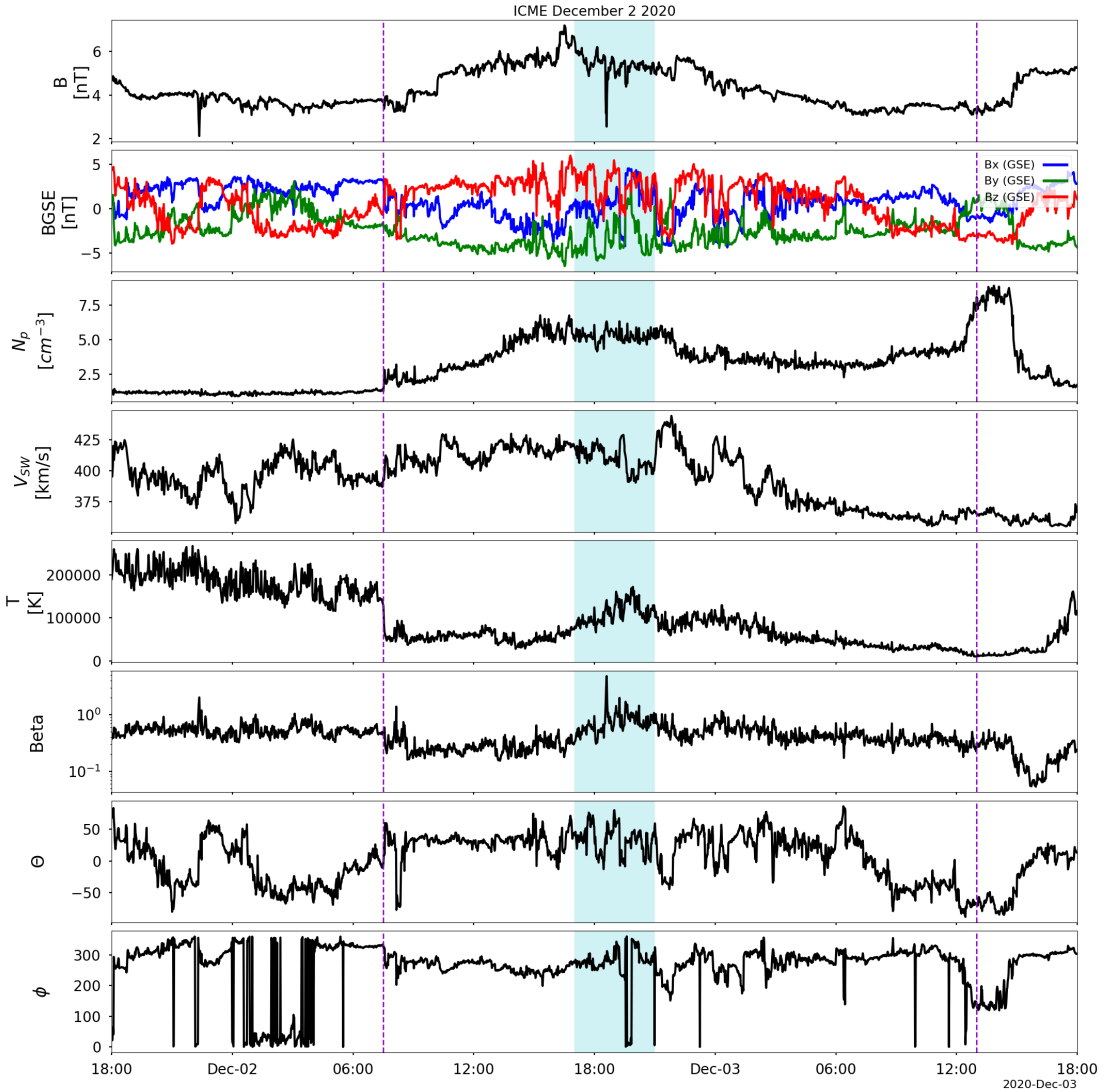

SOURCE: Author.

Figure A.6 - June 12, 2021 event observed by WIND spacecraft.

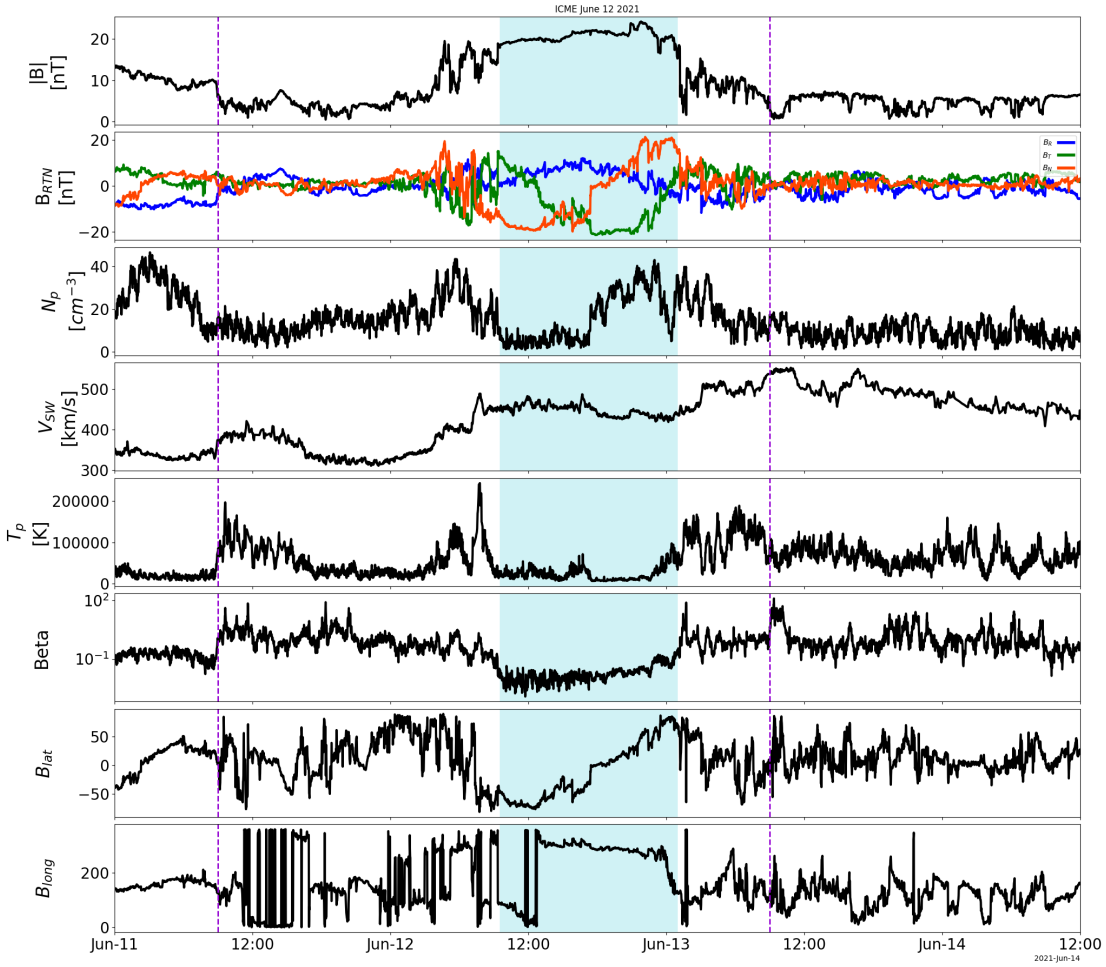

SOURCE: Author.